TECHNISCHE UNIVERSITÄT MÜNCHEN

School of Natural Sciences
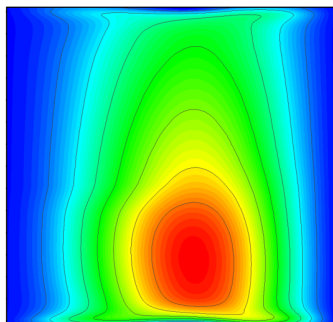
Forschungs-Neutronenquelle
Heinz Maier-Leibnitz (FRM II)

Coupled Thermal-Hydraulic and Mechanic Calculations for FRM II

Dissertation

Kaltrina Shehu

June 2023

Prof. Dr. Winfried Petry, TUM, Lehrstuhl E13

Dr. Christian Reiter, McMaster University - Engineering Physics, TUM CNSI

Technische Universität München
TUM School of Natural Sciences

Coupled Thermal-Hydraulic and Mechanic Calculations for FRM II

Kaltrina Shehu

Vollständiger Abdruck der von der TUM School of Natural Sciences der Technischen

Universität München zur Erlangung einer

Doktorin der Naturwissenschaften (Dr. rer. nat)

genehmigten Dissertation.

Vorsitz: Prof. Dr. Björn Garbrecht

Prüfer*innen der Dissertation:

1.   Prof. Dr. Winfried Petry
2.   Prof. Dr. Bastian Märkisch

Die Dissertation wurde am 25.05.2023 bei der Technischen Universität München eingereicht

und durch die TUM School of Natural Sciences am 12.06.2023 angenommen.

.

"When I meet God, I am going to ask him two questions:
Why relativity? And why turbulence? I really believe he
will have an answer for the first."

—Werner Heisenberg

Abstract

The Forschungs-Neutronenquelle Heinz Maier-Leibnitz (FRM II) actively pushes the international efforts to reduce the use of highly enriched uranium (HEU) in civil operations. A new fuel containing highly dense uranium-molybdenum (UMo) alloys is being developed together with international partners to replace the currently used HEU fuels. This fuel allows Forschungs-Neutronenquelle Heinz Maier-Leibnitz (FRM II) to convert to Low Enriched Uranium (LEU).

For the conversion to LEU fuel, the change of the core geometry is imminent. Therefore, the entire reassessment of the neutronic, thermal-hydraulic and thermal-mechanical behavior of the FRM II core is entailed. This work focuses on developing a fully coupled system that accounts for neutronics, hydraulics and mechanics, with hydraulics and mechanics exchanging data on step bases. To achieve this goal, Serpent 2, Ansys CFX and Ansys Mechanical are used for the neutronics, thermal-hydraulic and mechanical calculations, respectively. The thermal-hydraulic and thermal-mechanic aspects of a potential LEU core design that originates from an extensive scoping process were assessed using different coupling schemes.

The starting point is verifying and validating Computational Fluid Dynamics (CFD) code Ansys CFX and Computational Structural Mechanics (CSM) code Ansys Mechanical using experiments that are representative of the FRM II operating conditions, such as Gambill-Bundy and Cheverton-Kelley experiments. It could be shown that Ansys CFX and Ansys Mechanical were able to capture the physical aspects of the experiments well. The codes were additionally verified with similar codes within the Involute Working Group (IWG) framework.

Having verified and validated CFD and CSM codes, the next step consisted in verifying Serpent 2 and Ansys CFX using the FRM II licensing documents and the previously performed MCNP-Ansys CFX coupling as a validation and verification basis. The results obtained from the Serpent 2-Ansys CFX coupling for the current HEU core agree well with the FRM II licensing documents and the previously performed MCNP-Ansys CFX coupling. The Serpent 2-Ansys CFX coupling was performed for both the current HEU core and the potential LEU design, comparing several parameters between the two.

The deformations occurring on the plate as a result of thermal expansion and pressure loads were assessed via a sequential Thermal-Fluid-Structure Interaction (TFSI) coupling scheme. Additionally, the influence of the deformations on the coolant flow was accounted for in a direct TFSI coupling. These couplings were performed on the current FRM II core and the potential LEU core.

The potential LEU core design is deemed scientifically feasible based on these calculations. With the results presented in this thesis, all necessary tools to assess the core thermal-hydraulic and mechanical stability under nominal and incident scenarios are available.

Zusammenfassung

Die Forschungs-Neutronenquelle Heinz Maier-Leibnitz (FRM II) treibt die internationalen Bemühungen zur Reduzierung der Verwendung von hochangereichertem Uran (HEU) im zivilen Bereich aktiv voran. Gemeinsam mit internationalen Partnern wird ein neuer Brennstoff mit hochdichten Uran-Molybdän-Legierungen (UMo) entwickelt, der die derzeit verwendeten HEU-Brennstoffe ersetzen soll. Dieser Brennstoff ermöglicht die Umwandlung von FRM II in LEU.

Für die Umstellung auf LEU-Brennstoff steht die Änderung der Kerngeometrie unmittelbar bevor. Daher ist eine vollständige Neubewertung des neutronischen, thermohydraulischen und thermomechanischen Verhaltens des FRM II-Kerns erforderlich. Diese Arbeit konzentriert sich auf die Entwicklung eines vollständig gekoppelten Systems, das die Neutronik, die Hydraulik und die Mechanik berücksichtigt, wobei die Hydraulik und die Mechanik Daten auf Stufenbasis austauschen. Um dieses Ziel zu erreichen, werden Serpent 2, Ansys CFX und Ansys Mechanical für die neutronischen, thermohydraulischen bzw. mechanischen Berechnungen verwendet. Die thermohydraulischen und thermomechanischen Aspekte eines potenziellen LEU-Kerndesigns, das aus einem umfangreichen Scoping-Prozess hervorgegangen ist, wurden unter Verwendung verschiedener Kopplungsschemata bewertet.

Ausgangspunkt ist die Verifizierung und Validierung des CFD-Codes (Computational Fluid Dynamics) Ansys CFX und des CSM-Codes (Computational Structural Mechanics) Ansys Mechanical anhand von Experimenten, die für die Betriebsbedingungen des FRM II repräsentativ sind, wie z. B. Gambill-Bundy- und Cheverton-Kelley-Experimente. Es konnte gezeigt werden, dass Ansys CFX und Ansys Mechanical in der Lage waren, die physikalischen Aspekte der Experimente gut zu erfassen. Die Codes wurden zusätzlich mit ähnlichen Codes im Rahmen der Involute Working Group (IWG) verifiziert.

Nach der Verifizierung und Validierung der CFD- und CSM-Codes bestand der nächste Schritt in der Verifizierung von Serpent 2 und Ansys CFX unter Verwendung der FRM II Lizenzierungsdokumente und einer zuvor durchgeführten MCNP-Ansys CFX-Kopplung als Grundlage für die Validierung und Verifizierung. Die Ergebnisse der Serpent 2-Ansys CFX-Kopplung für den aktuellen HEU-Kern stimmen gut mit den FRM II-Lizenzierungsunterlagen und der zuvor durchgeführten MCNP-Ansys CFX-Kopplung überein. Die Serpent 2-Ansys CFX-Kopplung wurde sowohl für den aktuellen HEU-Kern als auch für das potenzielle LEU-Design durchgeführt, wobei mehrere Parameter zwischen beiden verglichen wurden.

Die auf der Platte auftretenden Verformungen infolge thermischer Ausdehnung und Druckbelastungen wurden über ein sequenzielles Kopplungsschema Thermal-Fluid-Structure Interaction (TFSI) bewertet. Zusätzlich wurde der Einfluss der Verformungen auf den Kühlmittelfluss in einer direkten TFSI-Kopplung berücksichtigt. Diese Kopplungen wurden für den aktuellen FRM II-Kern und den potenziellen LEU-Kern durchgeführt.

Auf der Grundlage dieser Berechnungen wird das Design des potenziellen LEU-Kerns als wissenschaftlich machbar angesehen. Diese Arten der Kopplung bieten alle notwendigen Instrumente zur Bewertung der thermohydraulischen und mechanischen Stabilität des Kerns im Nominalbetrieb und unter Störfallszenarien.

Contents

Contents

CHAPTER 1

Introduction

1.1 FRM II

Figure 1.1: *Scenic view of FRM II area, with the FRM (Atomei) on the right hand side, and FRM II on the left hand side.*

The neutron source Forschungs-Neutronenquelle Heinz Maier-Leibnitz (FRM II) is located in the Technische Universität München (TUM) campus Garching, Germany. Operating with a power of 20 MW, it is Germany's most powerful neutron source. FRM II is the descendant of Atomei (FRM), which started operation in 1957 and was decommissioned in 2000. With a first criticality on March 2nd, 2004, FRM II is Germany's youngest reactor, and since the end of April, 2023, it is Germany's last operational reactor with a considerable thermal power. As a modern research reactor, the concept and development of FRM II were based on the design of the High Flux Isotope Reactor (HFIR) at Oak Ridge National Laboratory (ORNL) in the United States and High Flux Reactor (RHF) at Institute Laue Langevin (ILL), Grenoble, France. The design was optimized to obtain the highest thermal flux outside the fuel element while retaining a low thermal power and accommodating many beam tubes, adding to a substantially different

design concept compared to a power reactor. FRM II typically operates four cycles a year, each having 60 days of neutron beam. With an undisturbed thermal neutron flux of $8 \cdot 10^{-14} \, \mathrm{n/s/cm^2}$ at $20 \, \mathrm{MW}$ thermal power, FRM II has the highest flux-to-power ratio worldwide. It is cooled with light water, moderated, and reflected with heavy water [1].
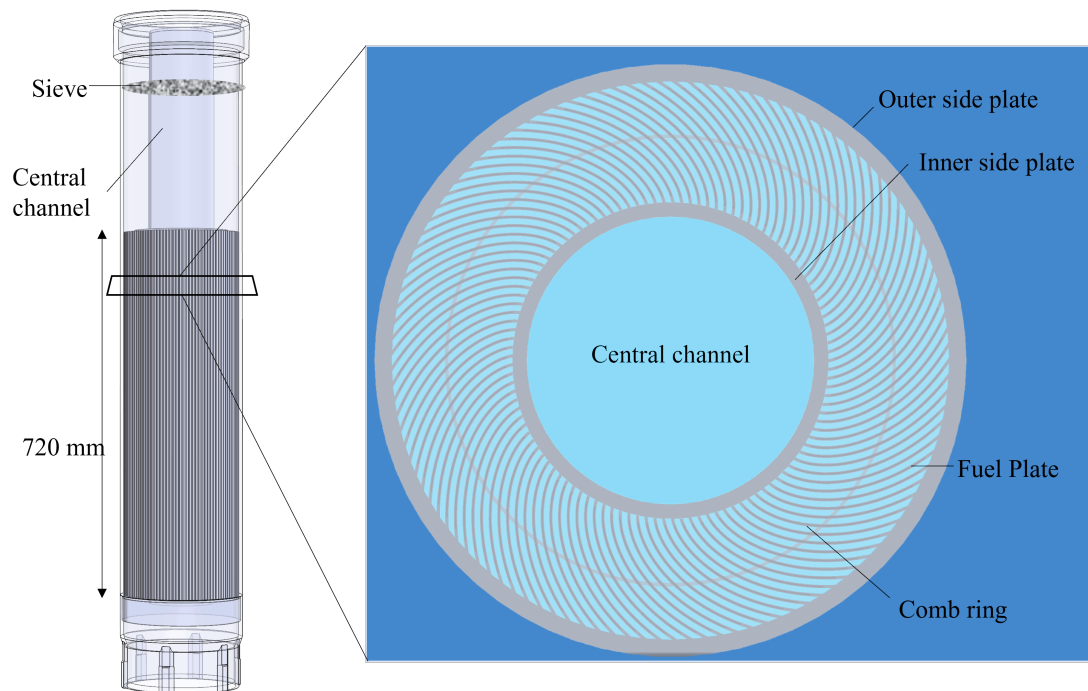
Figure 1.2: *A computer-aided design (CAD) model of the core is shown on the left-hand side, while a horizontal cut can be seen on the right-hand side. 113 involute-shaped plates are shown, together with the fuel element's inner and outer side plates, and the comb ring. The right figure's light and dark blue colors represent the light water and heavy water moderator, respectively.*
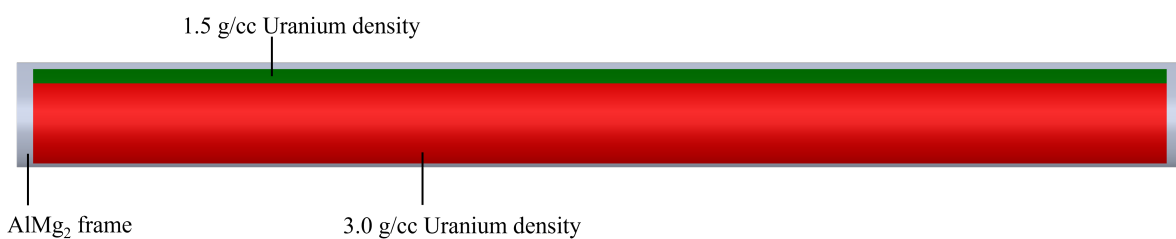
Figure 1.3: *The fuel plate with two different uranium densities and AlMg$_2$ frame. Red, green and gray colored areas refer to the 3.0 gUcm^{-3}, 1.5 gUcm^{-3} and AlMg$_2$, respectively.*

Fuel Element and Enrichment

FRM II, just like the other two predecessors HFIR and RHF, contains a compact core with one single fuel element. Each fuel element has 113 involute[1] shaped fuel plates, as depicted in Figure 1.2. The involute geometry ensures a compact core with a constant cooling channel

---

[1]An involute is defined as a spiral generated around a circle.
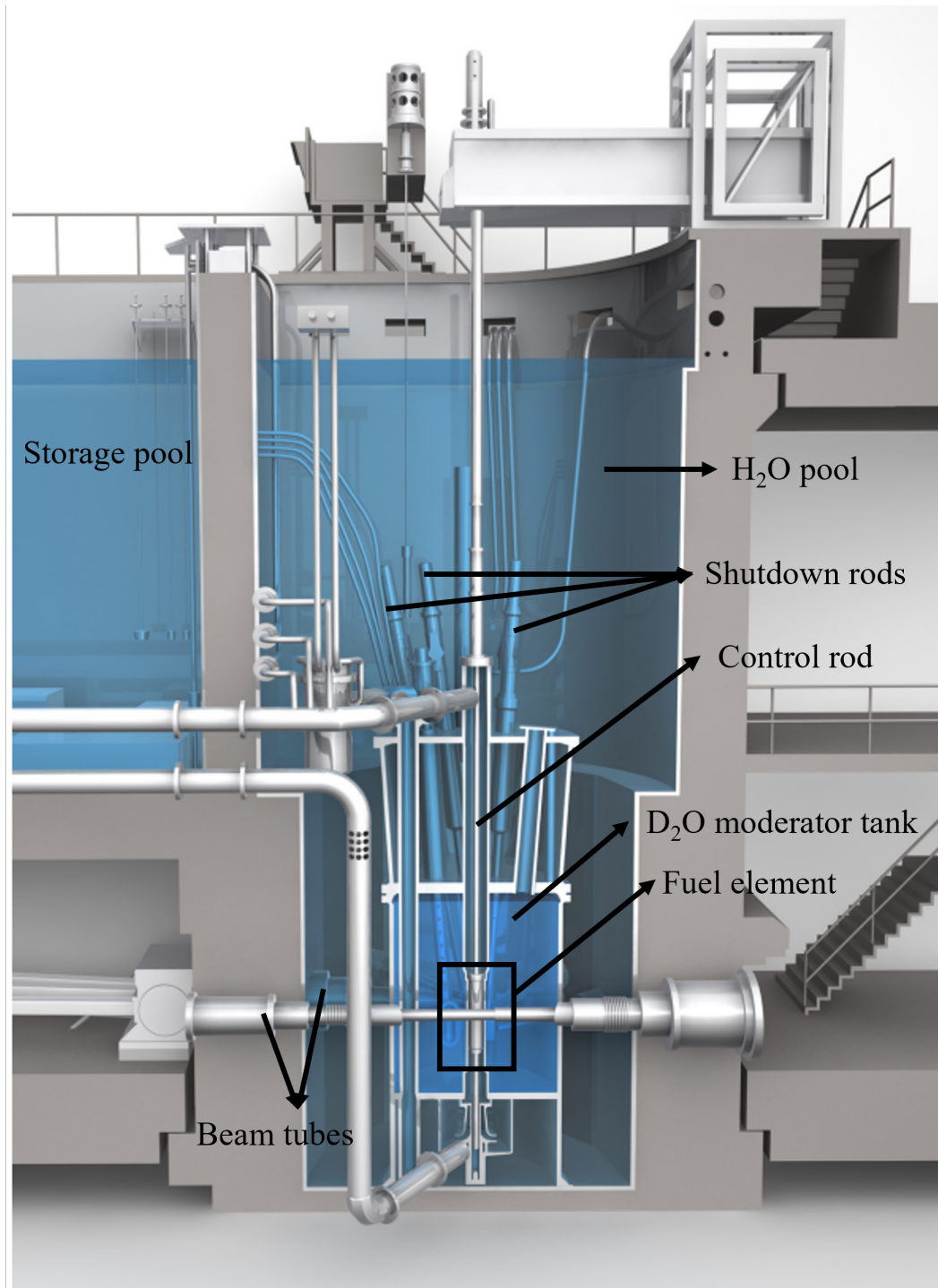
Figure 1.4: *A cross-section of the pool. The heavy water tank, light water moderator, shut-down rods, central channel, and fuel element are depicted [2, 3].*

thickness. FRM II uses 93% enriched U_3Si_2 dispersed in an aluminum matrix as fuel, and the fueled length in each plate is 70 cm long. An $AlMg_2$ frame surrounds the fueled area from all sides, resulting in a fuel plate length of 72 cm. The plates have a sandwich-like structure with the fuel in the middle and a layer of AlFeNi cladding on each side. With a fuel thickness of 0.6 mm and cladding thickness of 0.38 mm, the plate thickness amounts to 1.36 mm. Two different fuel densities are used for the plate. The fuel at the inner zone has a uranium density of $3.0\,\mathrm{g\,cm^{-3}}$. The uranium density close to the outer side plate is modified to $1.5\,\mathrm{g\,cm^{-3}}$ to reduce the heat deposited by the thermal neutrons being reflected from the heavy water reflector. Furthermore, a boron ring is placed at the bottom of the outer side plate to decrease the power peaking in this region.

The light water runs through 2.2 mm cooling channel which separates the plates. Roughly $274.5\,\mathrm{kg\,s^{-1}}$ water flows through the core with an average flow velocity of $15.9\,\mathrm{m\,s^{-1}}$. The fuel element is positioned in the central channel, also shown in Figure 1.2. A control rod made of hafnium at the top and a beryllium follower at the bottom is placed in the middle of the fuel element. The D_2O moderator encompasses the whole fuel element. Figure 1.4 shows a horizontal cross-section of the reactor pool. In addition to the central channel, the FRM II core contains multiple installations such as the cold source, hot source, 5 shut down rods[2], 11 beam tubes, the silicon doping system, material sample irradiation systems, and the high irradiation medical system. The whole assembly is immersed in the light water pool [1].

1.2   Conversion

As of today, FRM II is operating with U_3Si_2 fuel with 93% enrichment. Such enrichment is considered as Highly-Enriched Uranium (HEU). FRM II actively participates in international efforts to reduce uranium enrichment in civil cycles[4]. However, compared to other research reactors, the compact core and its already dense fuel make this reactor particularly cumbersome to convert. The given conversion criteria are:

- Fulfillment of the safety requirements. The safety margins calculated for the potential Low Enriched Uranium (LEU) core have to be at least as good as the ones for the current HEU core.

- Compatibility with the existing facility. In order to avoid prolonged shutdowns of the reactor, the LEU core needs to be downward compatible to the current facility. This means that the outer central channel radius is a constraint, so the extension of the core to the outer side is deemed infeasible.

- Preservation of the cycle length at 60 days to maintain the scientific activities and performance.

---

[2]Due to the cut, only three are shown in Figure 1.4.

- Marginal loss of neutron flux.

In order to lower the enrichment and fulfill the conversion criteria, modifications to the fuel element need to be applied. In addition, a new fuel has to utilize a higher chemical uranium density than the current one to compensate for the low enrichment. Only UMo fuel in monolithic form allows a conversion to LEU while fulfilling the conversion criteria [3]. The potential usage of this novel fuel for the conversion to LEU requires a new assessment of the core's neutronics, thermal-hydraulics, and mechanical aspects.

The thermal-hydraulic methods used for the licensing of FRM II in the past consisted of one-dimensional (1D) steady-state calculations [5]. While offering an overview of key quantities, 1D calculations are considered conservative. In order to provide a detailed representation of the thermal-hydraulic conditions in the core, effort is put into employing commercial Computational Fluid Dynamics (CFD) codes. So far, no high-flux research reactors have used CFD codes in their licensing process. Consequently, the verification and validation of CFD codes are of importance for conversion. Since all three involute reactors HFIR, RHF, and FRM II are pursuing the conversion to LEU, an alliance is formed to validate the CFD solvers and techniques for the high-performance research reactor safety analysis. Together with the support and expertise gained by Argonne National Laboratory (Argonne) through their several conversion programs, the three involute reactors have joined forces into the Involute Working Group (IWG) [6].

1.3   A Potential LEU Core

Identifying possible LEU core designs is a scientific process that relies on several design variables, objectives, and constraints. The details of the down-selecting process and the parametric study are not shown in this work. The interested reader can refer to the latest publication on this topic [3]. The LEU core used in this work originates from this publication. It is important to emphasize that this design is one of many that shows viability in accordance with the performed down-selection analysis. Therefore, it is referred to in this work as a potential LEU core.

A potential LEU core considered here uses monolithic UMo. This fuel type has been investigated thoroughly for the past twenty years [7, 8]. Additionally, the thermal-mechanical and physical properties have been thoroughly assessed [9].

This specific core design has 109 plates. The fuel itself is 0.45 mm thick and it is sandwiched between 0.3 mm AlFeNi cladding. The length of the active region is increased towards the top of the plate by 13 cm resulting in 83 cm fueled length. The frame remains unchanged compared to the current design, with 1 cm length on top and bottom of the fueled area, adding up to a plate length of 85 cm. The cooling channel thickness increases to 2.4 mm, yielding a larger flow area and higher moderation inside the fuel elements. Furthermore, to supply more fuel in the plate while maintaining compatibility with the current HEU core, the radius of the involute-generating

circle was decreased, leading to a larger involute plate arc length. At this stage of the project, the position of the combs is assumed to be unchanged. This means that the arc length of the involute plate starting from the inner side plate to the comb is unchanged. Subsequently, the combination of larger involute arc length and unchanged arc length distance between the combs and the inner side plate implies that the comb would no longer be located at the mid-radial distance between the side plates but closer to the inner side plate. Figure 1.5 is a schematic showing the geometrical differences between the current HEU core and the potential LEU core.
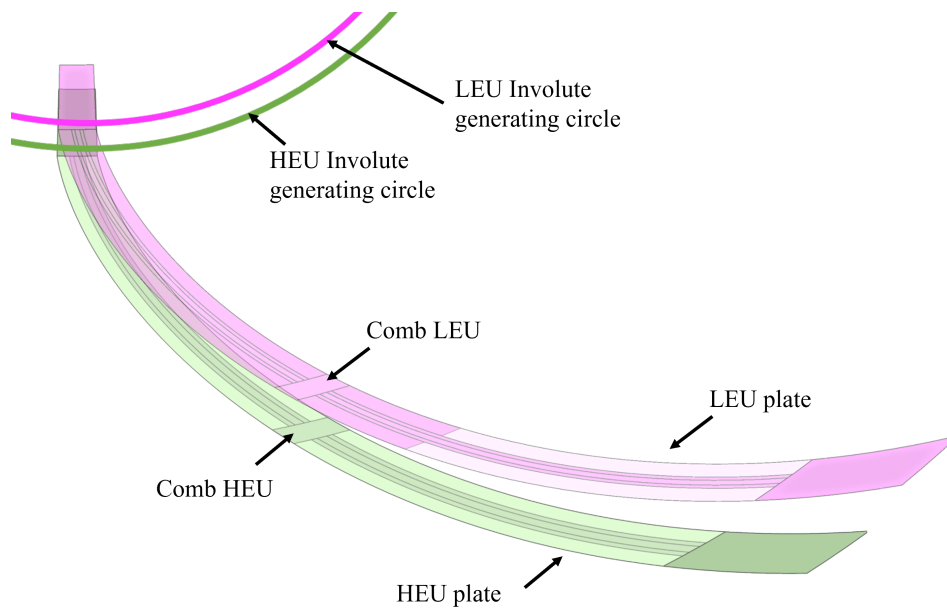
Figure 1.5: *Comparison between HEU (green) and LEU (pink) plates. The involute generating circles are shown for each plate. The combs can be identified at the mid half arc length for the HEU plate and slightly closer to the involute generating circle for the LEU plate.*

Since the potential LEU plate has a larger flow area, the pressure drop along the plate is expected to decrease in comparison to the current HEU plate. Additionally, due to the increased flow area, the flow resistance also decreases, thus, contributing to a lower pressure drop. Given that a certain pressure drop is required from the FRM II reactor control system, measures must be taken to increase the pressure. For this purpose, a flow restrictor located at the core outlet is introduced. A flow restrictor can be a Venturi nozzle[3] that confines the flow, leading to a decrease of the flow area at the bottom of the core, thus increasing the velocity, and adding an additional flow resistance. That leads to an irreversible pressure drop with the beneficial effect that a larger pressure at the bottom of the fuel plates increases the saturation temperature of the coolant, which in turn ameliorates the safety margins. In addition, the pressure drop through the restrictor in the reverse direction (bottom to top) has to be small in order to minimize its impact in transient accident scenarios, such as flow reversal due to failure of the pumps. According to calculations performed with a flow network script developed by Argonne to model the primary circuit, the flow restrictor should yield an additional pressure drop of 1.5 bar [3].

---

[3]A Venturi nozzle is a short narrow tube located within a wider tube.

The pump flow rate in the LEU core is assumed to remain unchanged. Due to the increased flow area, the flow resistance decreases in comparison to the current core. Adding the flow restrictor compensates for the difference in resistance between the two cores. The flow network script discussed in [3] calculates a mass flow rate of $277.6\,\mathrm{kg\,s^{-1}}$ for the potential LEU design. The small difference in mass flow rates between the HEU and LEU cores is due to the assumptions used in the flow network script and do not impact the safety or validity of the results.

It is crucial to point out that the flow restrictor presented here is a first assessment, and it is, therefore, subject to ongoing optimization. Figure 1.6b shows a design possibility of the flow restrictor in which the restrictor confines the flow at the core outlet and then reopens to the cooling channel. At this first assessment of the potential LEU core, the reopening of flow restrictor is not taken into account. Furthermore, in this work, the restrictor shown in Figure 1.6a is used. In the near future, the assessment of the LEU plate including the full restrictor is expected to take place.

Table 1.1 summarizes the main differences between the current HEU core and the potential LEU core from material and geometric points of view.
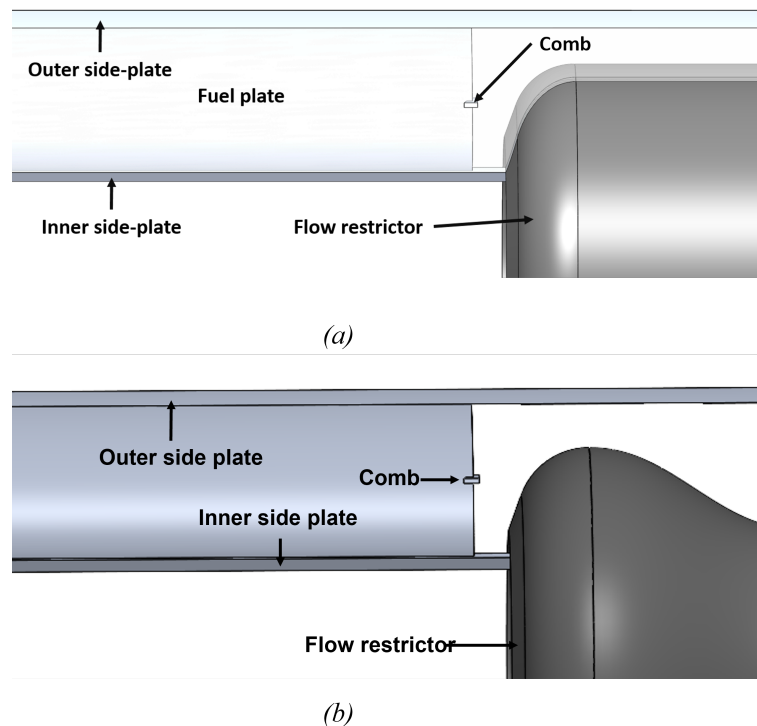
(a)

(b)

Figure 1.6: *The CAD model of the plate, including (a) the flow restrictor used in this work and (b) the potential flow restrictor. Note that only one plate is shown, while the restrictor is fully shown. Source (a) [3].*

	Parameter	Current HEU core	A potential LEU core
	Fuel	U$_3$Si$_2$-Al matrix	UMo monolithic
	Enrichment	93%	19.75%
Material	Cladding material		AlFeNi
	Frame material		AlMg2
	Number of plates	113	109
	Fuel length	72 cm	83 cm
	Plate length	70 cm	85 cm
	Fuel thickness	0.6 mm	0.45 mm
	Cladding thickness	0.38 mm	0.3 mm
Geometry	Cooling channel thickness	2.2 mm	2.4 mm
	Fuel width arc length	62.38 mm	71.07 mm
	Plate width arc length	69.39 mm	78.39 mm
	Flow restrictor	no	yes
	Mass flow	274.5 kg s^{-1}	277.3 kg s^{-1}
	Boron ring	bottom outer side plate	bottom outer side plate

Table 1.1: *Comparison between the current HEU core and a potential LEU core design considered in this work.*

1.4   This Work

The road of converting FRM II to Low-Enriched Uranium fuel (LEU) has many different aspects to be considered. The change of the core material to LEU entails an entire assessment of the new core's behavior based on neutronics, thermal-hydraulics, and mechanics. This work is primarily focused on the thermal-hydraulic and thermal-mechanic prospects. It is clear that all the calculations rely on the neutronics outcome; however, the neutronics part is not discussed in detail as substantial work has been performed in different frameworks and the work is still advancing [2, 10, 11].

The underlying goal of this thesis is to create a fully coupled system that takes into account neutronics, thermal-hydraulics, and mechanics, with hydraulics and mechanics systems exchanging information on a stepped basis. Even though a coupling between neutronics and thermal-hydraulics was performed in previous work [12], the starting point of this work is the verification and validation of the CFD and Computational Structural Mechanics (CSM) codes. Experiments that represent the thermal-hydraulics and mechanics of high-flux research reactors are taken as a validation basis [13]. The Gambill–Bundy experiments [13] and Cheverton–Kelley experiments [14] (also referred to as GB and CK experiments throughout this work) are two experiments that were done in the 1960s for the licensing of the HFIR reactor. The test sections used in these experiments represent the thermal-hydraulic and mechanical behavior of a high-flux research reactor such as HFIR, and by extension, also RHF and FRM II. These experimental setups are simulated in Ansys CFX (CFX) and Ansys Mechanical, respectively. The computational results

are compared to the actual experimental outcomes. This process is repeated with other codes such as Comsol and Star-CCM+ within the IWG framework [15, 16]. The results obtained with each code are compared to each other and to the experiment (see Chapter 11).

Being acquainted with the codes of choice, the next step consists of performing the coupling between the neutronics calculated by Serpent 2 and thermal-hydraulics by CFX, as shown in Chapter 12. For various reasons, since 2015, Serpent 2 has been used to account for the neutronics for FRM II as opposed to MCNP which was previously used in [12]. The coupling between Serpent 2 and CFX is done in-house. Using the power deposition provided by Serpent 2 and the conjugate heat transfer solver in CFX, this coupling provides insights into the pressure, velocity, and temperature field of the reactor plates and coolant. The accuracy and credibility of the Serpent 2–CFX coupling is attained via the previously completed verification and validation of the code (see Chapter 11), the comparability with the FRM II licensing documents, and comparability with previous work performed on the reactor plate using different codes (see Chapter 12). The agreement between different sources and the Serpent 2–CFX coupling for the current HEU plate provides additional credibility and confidence in using these methods for the prediction of the thermal-hydraulic and mechanic aspects of a potential LEU core for the conversion. The results obtained using the Serpent 2–CFX coupling for both core configurations are compared between each other.

Thus far, the entire range of FRM II fuel plate assessments has been focused solely on the neutronic and thermal-hydraulic behavior. However, in furtherance of a complete picture, the plate deformation under nominal conditions is beneficial in understanding the mechanical stability of the current core and the potential LEU one. This type of analysis is usually called a Fluid Structure Interaction (FSI) analysis; however, in this case, the name is updated to Thermal-Fluid-Structure Interaction (TFSI) since the coupling includes also the thermal aspect. The method and naming details are explained in detail in Chapter 7. The evaluation of the plate's deformation amplitude and profile is executed in two forms: the first form, called one-way coupling, is constructed to take the solution of the thermal-hydraulic solver CFX and map the results into the solid domain in Ansys Mechanical (see Chapter 13). In the second approach, also called two-way coupling, once the deformation is evaluated from the fluid solution, Ansys Mechanical sends the corresponding deflections back to CFX, where the deformation's influence on the velocity is taken into account. The process carries on depending on the model and convergence criteria (see Chapter 13). The TFSI simulations are performed for both the current HEU plate and a potential LEU plate in order to provide a comparison between the two. In addition, the newly settled TFSI coupling is used to assess a station blackout scenario in Chapter 14. A flowchart of the work performed in this thesis is shown in Figure 1.7.

The theoretical background related to fluid and structural mechanics is given in Part I and Part II, respectively. Part III explains the codes and the coupling approaches between them. Furthermore, the results are shown and discussed in Part IV. Lastly, Part V summarizes the results of this work.
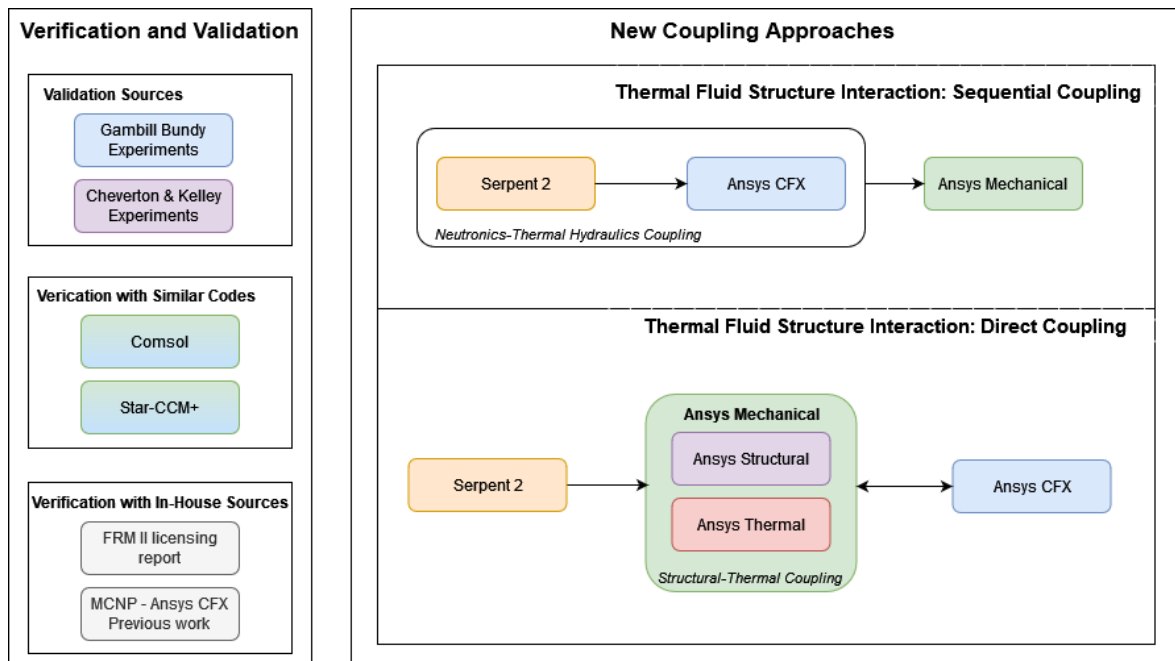
Figure 1.7: *Flowchart of this work. The left column contains the verification and validation sources used in this work. Comsol and Star-CCM+ in the Verification with Similar Codes category are colored green and blue since these codes have both fluid and solid solvers incorporated into one Graphical User Interface (GUI). The right column shows a flowchart of the two different coupling methods.*

Part I

Thermal Hydraulics

CHAPTER 2

Consideration of Basic Quantities

The thermal-hydraulic aspect of this thesis relies on the Navier-Stokes equations. In this chapter, the basis used to describe the equations is given first. A series of dimensionless quantities used to quantify and describe the thermal-hydraulic analysis are presented and described in detail in Section 2.1. Then, the heat transfer equation is given in Section 2.4, while heat transfer correlations are explained in Section 2.3. Furthermore, the boiling phenomenon with the focus on nucleate boiling is described in Section 2.4.

2.1 Dimensionless Numbers

The information given in this section is mainly based on [17–19].

Hydraulic diameter (d_h) is a term used when the channel under investigation is not exactly circular. There are several correlations to calculate the hydraulic diameter for different geometries [17]. Usually, d_h is defined as:

$$d_h = 4\frac{A}{p}$$

(2.1)

where A is the cross sectional area and p the perimeter.

Reynolds number (Re) is a dimensionless quantity defined by the ratio between a fluid's inertial and viscous forces. Re number serves as a measure for flow patterns such as turbulence, and it can be calculated as:

$$Re = \frac{vd_h}{\nu}$$

(2.2)

where v is the velocity of the fluid and ν is the kinematic viscosity[1]. Therefore, Reynolds number is temperature dependent. Low Re numbers are characteristic of laminar flows, indicating a domination of the viscous forces. On the contrary, high Re numbers occur in turbulent flows, where the inertial forces dominate. For pipe flows, a Re number at about 2300 presents the transition between laminar and turbulent flows.

Prandtl number (Pr) is defined as a ratio between the momentum diffusivity (or kinematic viscosity) and thermal diffusivity:

$$Pr = \frac{\nu}{a} \tag{2.3}$$

where a is the thermal diffusivity defined as:

$$a = \frac{k}{c_p \rho} \tag{2.4}$$

where k is the thermal conductivity, c_p the specific heat capacity at constant pressure and ρ the density.

In conjugate heat transfer cases, Pr number also represents the ratio between the momentum boundary layer thickness d_M and the thermal boundary layer d_T [17].

$$\frac{d_M}{d_T} \approx Pr \tag{2.5}$$

The definition of the boundary layers is illustrated in Figure 2.1. Supposing that there is a fluid flowing with velocity $\boldsymbol{v}$ by a heated wall with temperature T_{Solid}, the fluid velocity close to the wall is zero. In regions far from the wall, the velocity is $\boldsymbol{v}$. The momentum boundary layer thickness is the distance from the wall towards the center of the channel where the velocity has reached an asymptotic behavior or roughly 99% of the free stream velocity[2].
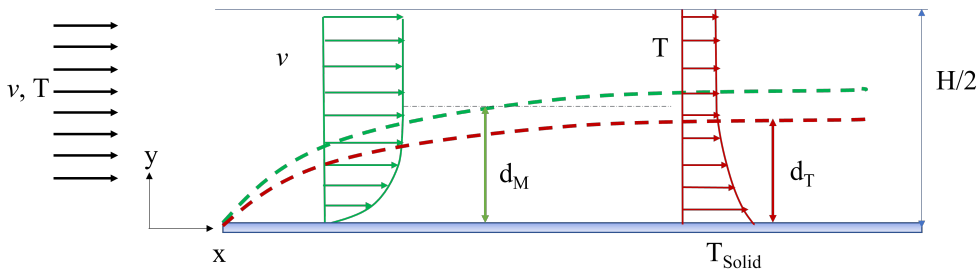
Figure 2.1: *The definition of the momentum boundary layer d_M and thermal boundary layer d_T. Refurbished from [19].*

---

[1]Kinematic viscosity is a measure of of the fluid flow resistance, and it is calculated as the absolute (or dynamic) viscosity divided by the density.

[2]The term free stream is used to describe a region that is far from a boundary.

In heat transfer processes, the fluid in close proximity to the heated wall has roughly the same temperature as the wall, while the fluid at the center of the channel has a lower temperature. Therefore, convective heat transfer takes place in the direction perpendicular to the flow. The thermal boundary layer is defined as the distance from the heated wall for which the fluid has reached 99 % of the free stream temperature [19].

As seen in Equation (2.5), for large Pr numbers, the momentum boundary layer is larger than the thermal one. The opposite occurs for low Pr numbers. In the heated regions of the FRM II plates, the Pr number is low; therefore, the thermal boundary layer is thicker than the momentum one.

Nusselt number (Nu) [18] is calculated as the ratio between the convective heat transfer and conductive heat transfer. Hence, it can also be considered a dimensionless heat transfer coefficient.

$$Nu = \frac{hd}{k} \tag{2.6}$$

where h is the heat transfer coefficient, its calculation heavily depends on the fluid properties, the fluid regime, and geometry.

2.2 Heat Transfer

The energy equation for a solid body is written as:

$$\frac{\partial T}{\partial t} = \nabla(a\nabla T) + S \tag{2.7}$$

where S is a source term, and a is the thermal diffusivity. The thermal diffusivity is defined in Equation (2.4) where k is the thermal conductivity, c_p the specific heat capacity and ρ the density.

The source term is a temperature source $[\mathrm{K\,s^{-1}}]$:

$$S = \frac{Q}{c_p\rho} \tag{2.8}$$

The energy per unit volume and time is denoted by Q. For a steady state application, the time derivative of the temperature is zero, therefore:

$$\nabla(a\nabla T) = -S \tag{2.9}$$

Equation (2.9) has to be solved for the volume elements by applying the divergence theorem:

$$\int \nabla(a\nabla T)dV = \oint a\boldsymbol{\nabla}T d\boldsymbol{A} = -\int SdV \tag{2.10}$$

2.3 Heat Transfer Correlations

Heat transfer is a complicated physical process. Therefore, heat transfer correlations that can evaluate the heat flux at the fluid-solid interface are widely used in thermal-hydraulic frameworks. These correlations take into account the geometry of the channel, the fluid properties, and the operating conditions [20]. Correlations can be expressed in terms of dimensionless quantities that characterize the flow and its thermal conditions. For instance, heat transfer is represented by the dimensionless heat transfer coefficient (Nu), which can be expressed by quantities such as Re and Pr, yielding an understanding whether the heat transfer is driven by conduction or convection. The classical one-dimensional thermal-hydraulic codes rely on correlations such as Sieder-Tate [21] or Hausen [22] to calculate the heat flux and heat transfer coefficients[3]. Therefore, it is common practice to compare the heat transfer results obtained with Computational Fluid Dynamics (CFD) codes to 1D calculations. Sieder-Tate and Hausen correlations are usually used for plate-type geometries [23], such as the Forschungs-Neutronenquelle Heinz Maier-Leibnitz (FRM II) plate. Therefore, they are briefly introduced in the next section.

2.3.1 Sieder-Tate Correlation

In 1936, Sieder and Tate [21] used a series of heat transfer parameters measured on several types of oil with very different temperature coefficients of viscosity in order to develop a correlation using dimensionless numbers. The main focus of Sieder and Tate was to establish a correlation that could evaluate the temperature-dependent viscosity and viscosity gradients on the flow direction and perpendicular to the flow and heated walls. Therefore, they decided to use as dimensionless quantity the ratio between the viscosity of the mainstream flow and the viscosity at the heated wall $\frac{\mu_b}{\mu_w}$. This ratio is given in terms of the dynamic viscosity[4] and it estimates the interaction between the viscosity gradient of the temperature distribution and the velocity field. Thus, Nu number can be calculated by the Sieder-Tate correlation as:

$$Nu_{ST} = 0.027(Re)_b^{0.8}(Pr)_b^{1/3}\left(\frac{\mu_b}{\mu_w}\right)^{0.14} \tag{2.11}$$

The subscript b means the value is calculated at the fluid mean temperature.

The Sieder-Tate correlation is valid for Pr between 0.7 and 16700 and for Re larger than 10000 [17].

---

[3]For CFD, the heat fluxes are calculated based on a mesh. See Chapter 3

[4]Dynamic (or absolute) viscosity is a measure of force required to make the fluid flow at a certain rate. It is important to note that the kinematic viscosity, on the other hand, gives information about the velocity the fluid is flowing when a force is applied on it.

2.3.2 Hausen Correlation

Helmuth Hausen extended the Sieder-Tate correlation to be used both for transitional and fully turbulent flows [22]. Nu number, according to Hausen's correlation, can be calculated as:

$$Nu_H = 0.116[(Re)_b^{2/3} - 125](Pr)_b^{1/3} \left[1 + \left(\frac{d_h}{L_h} \right)^{2/3} \right] \left(\frac{\mu_b}{\mu_w} \right)_x^{0.14} \tag{2.12}$$

where L_h is the heated length. All the properties except μ_w are evaluated at the fluid temperature.

2.4 Boiling Phenomena

FRM II is designed in a way that no boiling occurs under nominal conditions. However, the assessment of the safety margins is necessary. An important scenario for FRM II is the flow reversal scenario, where nucleate boiling is expected (see Chapter 14). To explain what nucleate boiling is and subsequently illustrate this scenario, the Nukiyama boiling curve in Figure 2.2 is used.
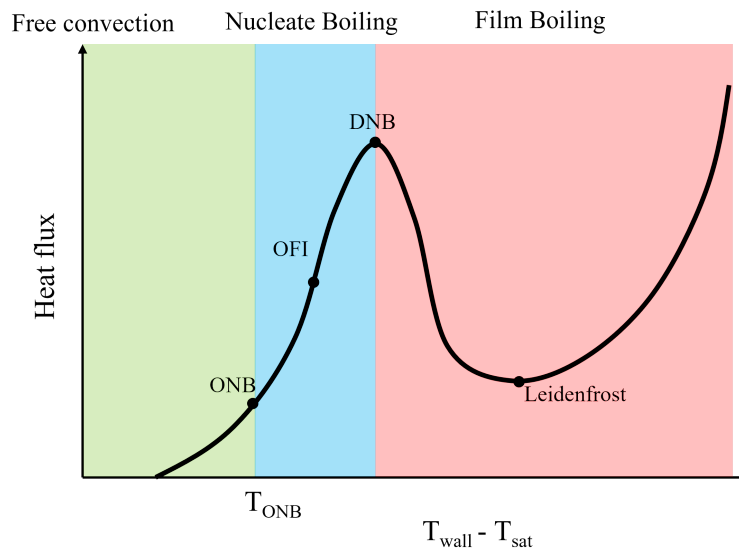
Figure 2.2: *Typical boiling curve showing the evolution of the heat flux at the heated wall depending on the wall superheat, also defined as the temperature difference between the wall temperature and the fluid saturation temperature. Refurbished from source [24].*

Nucleate boiling occurs when the heat flux at a solid surface is increased, and therefore, the temperature of the wall is increased by a couple of degrees above the water saturation temperature. In this case, small bubbles start forming at the wall. However, since the applied heat flux is not large enough, most of the water is still below the saturation temperature. Therefore, the steam bubbles cannot get too far from the wall without condensing. This point is the Onset of

Nucleate Boiling (ONB). This flow is called subcooled flow boiling. If the heat flux is increased further, the water temperature also increases. The bubbles start detaching from the walls and merge with the fluid flow. This process continues until the heat flux is large enough that bubbles have increased in size and the detachment rate is also large. This point is called Departure from Nucleate Boiling (DNB). The largest value of heat flux that can be achieved is called Critical Heat Flux (CHF). There comes the point where a large amount of vapor bubbles is covering the wall. The heat transfer from the heated wall to vapor is much less efficient than to liquid, causing the heat flux to decrease. This point is called the Leidenfrost point. From this point on, the heated wall is covered exclusively by vapor and radiation is the main heat transfer mechanism. This causes the heat flux to increase fast. This region is referred to as film boiling [25].

In the case of FRM II, nucleate boiling is related to pump failures. In the event of a pump failure, the coolant is subject to decay heat from the fission reaction. The water gets warmer and natural convection takes place. In Figure 2.2 this is denoted from the starting point of the curve up to ONB. The coolant temperature is still below the saturation temperature, and the flow is still in a single phase; therefore, no bubbles form. Nucleate boiling occurs when the temperature of the wall is between $5\,°C$ to $10\,°C$ larger than the water saturation temperature. In ONB, the coolant pressure decreases and bubbles form at the cladding surface (two-phase flow). The pressure decreases further while the void fraction increases with the coolant velocity decreasing until the Onset of Flow Instability is reached (OFI). This process continues until DNB transpires. The presence of numerous vapor bubbles at the wall causes an increase in frictional drag and a decrease of pressure drop.

This work does not include the flow reversal CFD calculations for the FRM II plate. However, since 2021 efforts have been made to build representative experimental setups that focus on capturing the nucleate boiling in a simple rectangular channel. The data acquisition is expected to facilitate the CFD modeling of such scenarios for FRM II in the very near future. The interested reader can refer to the master thesis performed as a first step of nucleate boiling assessment [26].

CHAPTER 3

Fluid Mechanics

3.1 Navier-Stokes Equations

Fluid mechanics is based on the assumption that the density of a fluid is large enough to approximate it as a continuum. This means that even an infinitesimal amount of fluid is composed of a plentiful amount of particles, each with a velocity and mean kinetic energy. Consequently, one can determine the pressure, temperature, density, turbulence parameters and other quantities related to the fluid. The governing equations of fluid dynamics are primarily based on three conservation laws: the conservation of mass, momentum and energy. These three laws define a set of equations called the Navier-Stokes equations [27], and they can be expressed based on the Reynolds Transport Theorem [28], which is a three-dimensional generalization of Leibnitz rule:

$$\frac{d}{dt} \int_{V(t)} \boldsymbol{f} dV = \int_{V(t)} \frac{d\boldsymbol{f}}{dt} dV + \int_{S(t)} f \boldsymbol{v} \cdot \boldsymbol{n} dS \tag{3.1}$$

$\boldsymbol{f}$ is a general quantity, V(t) is the element volume at time t, S(t) is the surface at time t and $\boldsymbol{n}$ is the vector normal to the surface. Equation (3.1) connects two different ways to describe the motion of a fluid: the Lagrangian and Eulerian approaches. In the Lagrangian approach, all fluid particles are followed and the change around each particle is described in terms of its path. In the Eulerian approach, all particles are characterized at fixed positions at different times.

Mass Conservation

The conservation law of mass or continuity equation is based on the logic that the mass in a single-phase fluid system cannot disappear nor be created out of nothing. Therefore, the mass change in an infinitesimal volume element equals the sum of mass fluxes through the surfaces. The mass fluxes through the X-direction of one element are shown in Figure 3.1.
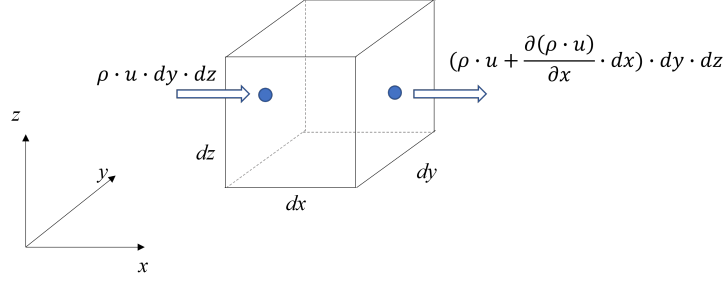
Figure 3.1: *The mass fluxes in X-direction through an infinitesimal element volume. Since only the X-direction is taken into account, the u component of velocity is used. Refurbished from [29].*

For all three directions, the continuity equation for one element is written as:

$$\int_{V(t)} \frac{d\boldsymbol{\rho}}{dt} dV + \int_{S(t)} \rho \boldsymbol{v} \cdot \boldsymbol{n} dS = 0 \tag{3.2}$$

where ρ refers to the density and $\boldsymbol{v}$ to the velocity vector. Using Gauss' theorem, Equation (3.2) can be written as:

$$\frac{\partial \rho}{\partial t} + \nabla (\rho \cdot \boldsymbol{v}) = 0 \tag{3.3}$$

Momentum Conservation

The equation regarding the conservation of momentum is an application of Newton's second law. Therefore, the time-dependent momentum change in an element $\rho \boldsymbol{v}$ is calculated as the difference between incoming and outgoing momentum currents plus the sum of the forces acting on the volume element. Two types of forces act on the control volume: body and surface forces. The body forces can be gravity or buoyancy. Surface forces can be separated into two parts: the pressure and the viscous stress tensor $\boldsymbol{\tau}$ that includes the normal stress and shear stress, i.e.:

$$\boldsymbol{\sigma} = -p\delta_{ij} + \boldsymbol{\tau} \tag{3.4}$$

where δ_{ij} is the Kronecker delta and $\boldsymbol{\sigma}$ is the stress tensor. The pressure is expressed in terms of the normal stress components:

$$p = -\operatorname{tr}(\sigma) \tag{3.5}$$

The minus sign indicates that the pressure is acting on the volume.

For Newtonian fluids, the normal and shear stresses can be expressed in terms of the velocity gradient such that:

Figure 3.2: *Momentum in X-direction through an infinitesimal volume element. Since only the X-direction is taken into account, the u component of velocity is used. Refurbished from [29].*

$$\tau_{ii} = \lambda \boldsymbol{\nabla} \cdot \boldsymbol{v} + 2\mu \frac{\partial v_i}{\partial x_i} \tag{3.6}$$

and

$$\tau_{ij} = \tau_{ji} = \mu \left(\frac{\partial v_i}{\partial x_j} + \frac{\partial v_j}{\partial x_i} \right) \tag{3.7}$$

In Equation (3.6), λ is the bulk viscosity[1]. The momentum conservation law for one element is written as:

$$\rho \cdot \left(\frac{\partial \boldsymbol{v}}{\partial t} + (\boldsymbol{v} \cdot \boldsymbol{\nabla}) \, \boldsymbol{v} \right) = -\nabla p + \mu \Delta \boldsymbol{v} + \rho \boldsymbol{g} \tag{3.8}$$

Energy Conservation

The energy conservation equation is another way of expressing the first law of thermodynamics. The time-dependent change of energy in a volume can be calculated as the sum of incoming and outgoing energy flux in an element, the flow of energy due to heat transfer, the work done by all the forces such as compressive forces, normal- and shear stress and energy contribution from external sources. The total energy of an infinitesimal volume element is a sum of the internal energy $\rho e dV$ and kinetic energy $\rho |\boldsymbol{v}|^2 dV$:

$$\rho E dV = \rho e dV + \rho |\boldsymbol{v}|^2 dV \tag{3.9}$$

where e is the internal energy per unit mass.

The time change of energy in a volume equals the sum of the change in internal energy and the energy flux through the element walls. Analogously to Equation (3.1), the time change of energy is defined as:

$$\frac{d}{dt} \int (\rho E) dV = \int \frac{\partial (\rho E)}{\partial t} dV + \int \rho E \boldsymbol{v} \cdot \boldsymbol{n} dS \tag{3.10}$$

---

[1]The bulk viscosity, or also called volume viscosity, introduces damping that is associated to volumetric staining of the liquid, such as compression.
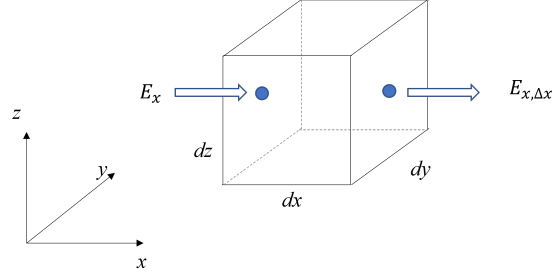
$$E_x = \rho \cdot \left[e + \frac{|\boldsymbol{v}|^2}{2} \right] \cdot u \cdot dy \cdot dz$$

$$E_{x,\Delta x} = \left(\rho \cdot \left[e + \frac{|\boldsymbol{v}|^2}{2} \right] \cdot u + \frac{\partial \left(\rho \cdot \left[e + \frac{|\boldsymbol{v}|^2}{2} \right] \cdot u \right)}{\partial x} \cdot dx \right) \cdot dy \cdot dz$$

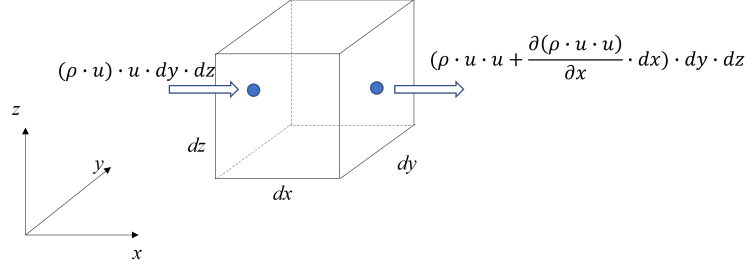**Figure 3.3:** *Energy through an infinitesimal volume element. Since only the X-direction is taken into account, the u component of velocity is used. Refurbished from [29].*

To account for the heating within the element, the Fourier law can be used:

$$d\dot{Q} = \rho q dV - k\boldsymbol{\nabla} T dS \tag{3.11}$$

where q is the heat strength and k is the thermal conductivity.

The time rate of the work done by the compressive forces can be written as:

$$dW = \rho \boldsymbol{g} \cdot \boldsymbol{v} + \boldsymbol{v} \cdot (\boldsymbol{\sigma} \cdot \boldsymbol{n}) dS \tag{3.12}$$

Applying the divergence theorem, the energy equation can be assembled to:

$$\frac{\partial(\rho E)}{\partial t} + \boldsymbol{\nabla} \cdot (\rho E \boldsymbol{v}) = \boldsymbol{\nabla} \cdot (k\boldsymbol{\nabla} T) + \rho q - \boldsymbol{\nabla} \cdot (p\boldsymbol{v}) + \rho \boldsymbol{g} \cdot \boldsymbol{v} + \boldsymbol{\nabla} \cdot (\boldsymbol{\tau} \cdot \boldsymbol{v}) \tag{3.13}$$

Equation (3.3), (3.8) and (3.13) add up to the compressible Navier-Stokes equations. They can be expressed in a conservation form as:

$$\frac{\partial \boldsymbol{U}}{\partial t} + \nabla \cdot \boldsymbol{F} = \boldsymbol{Q} \tag{3.14}$$

where:

$$\boldsymbol{U} = \begin{pmatrix} \rho \\ \rho \boldsymbol{v} \\ \rho E \end{pmatrix} \tag{3.15}$$

$$\boldsymbol{F} = \begin{pmatrix} \rho\boldsymbol{v} \\ \rho\left(\boldsymbol{v}\cdot\boldsymbol{\nabla}\right)\boldsymbol{v} \\ \left(\rho E + p\right)\boldsymbol{v} - k\nabla T - \boldsymbol{\tau}\cdot\boldsymbol{v} \end{pmatrix} \tag{3.16}$$

$$\boldsymbol{Q} = \begin{pmatrix} 0 \\ \rho\boldsymbol{g} \\ \rho\left(q + \boldsymbol{g}\cdot\boldsymbol{v}\right) \end{pmatrix} \tag{3.17}$$

Equation (3.14) is a system of 5 equations and 5 variables: ρ, $\rho\boldsymbol{v}$ and ρE. However, since there are 7 unknown flow field variables: ρ, u, v, w, E, p and T, this system is under-defined. Therefore, two more thermodynamic relations are necessary, such as the pressure dependence on density and temperature and the internal energy in terms of pressure and temperature. In addition, the viscosity μ and thermal conductivity k have to be determined in dependence on the system's state so that this equation system is closed. Such formulations are derived for an ideal and a real gas in literature [27]. Given the complicated nature of Navier-Stokes equations[2], to describe a real-life turbulent flow, the British physicist Osborne Reynolds suggested the so-called Reynolds-averaging approach, which is described in the following section.

3.2   Reynolds Averages Navier-Stokes (RANS) Equations

Osborne Reynolds introduced the concept of decomposing quantities into averaged and fluctuating components that can help solve a set of equations that covers the turbulence models [31]. This way, the turbulence fluctuations can be eliminated. A variable can be divided into two parts: the averaged and varying components, e.g., velocity:

$$\boldsymbol{v_i} = \overline{\boldsymbol{v_i}} + \boldsymbol{v'_i} \tag{3.18}$$

The averaged part can be expressed as:

$$\overline{v_i} = \frac{1}{\delta t}\int_{t}^{t+\delta t} v_i \, \mathrm{d}t \tag{3.19}$$

The time interval δt is chosen in a way that it is small compared to the time scale of solving the equations but larger in account of the turbulent fluctuations[3].

---

[2]As of the early 2000s, the existence of smooth and reasonable solutions of the Navier-Stokes equations in three-dimensional (3D) constitute a millennium problem [30]. In fact, the smoothness of these equations is the last unsolved problem of classical mechanics.

[3]This is Favre-averaging when weighted by density for the compressible flows.

Substituting the averaged quantities into the conservation equation in Section 3.1 one gets Equation (3.20) for the mass conservation, Equation (3.21) for momentum conservation and Equation (3.22) for energy conservation:

$$\frac{\partial \overline{\rho}}{\partial t} + \nabla \cdot (\overline{\rho \boldsymbol{v}}) = 0 \tag{3.20}$$

$$\frac{\partial \overline{\rho \boldsymbol{v}}}{\partial t} + (\overline{\boldsymbol{v}} \cdot \nabla) \cdot \overline{\boldsymbol{v}} = -\nabla \overline{p} + \mu \nabla^2 \overline{\boldsymbol{v}} + \overline{\rho} \boldsymbol{g} + \nabla \cdot \tau_t \tag{3.21}$$

$$\frac{\partial \left(\overline{\rho E} \right)}{\partial t} + \nabla \cdot \left(\overline{\rho \boldsymbol{v} E} \right) = \nabla \cdot (\kappa \Delta T) + \overline{\rho} q - \nabla \cdot (\overline{p \boldsymbol{v}}) + \overline{\rho} g \overline{\boldsymbol{v}} + \nabla \cdot \left(\overline{\boldsymbol{\tau}} \cdot \overline{\boldsymbol{v}} \right) \tag{3.22}$$

One can see that no changes were made to the continuity Equation (3.20) compared to the continuity equation without averaged quantities in Equation (3.3). However, turbulent flux terms are added to the momentum Equation (3.21) and the scalar transport Equation (3.22). The Reynolds stress tensor is the last term in Equation (3.21). It mathematically rises due to the nonlinear convective term when averaging. Physically, it describes the momentum transfer due to turbulent fluctuations. The Reynolds stress tensor has 9 components:

$$\tau_t = \overline{\rho v_i' v_j'} = \begin{bmatrix} \overline{\rho(v_1')^2} & \overline{\rho v_1' v_1'} & \overline{\rho v_1' v_3'} \\ \overline{\rho v_2' v_1'} & \overline{\rho(v_2')^2} & \overline{\rho v_2' v_3'} \\ \overline{\rho v_3' v_1'} & \overline{\rho v_3' v_2'} & \overline{\rho(v_3')^2} \end{bmatrix} \tag{3.23}$$

However, since velocities v_i' and v_j' can be interchanged, the Reynolds stress tensor has only 6 independent components. In order to solve for the components of Equation (3.23), a closure approach is needed. In 1877, Boussinesq [32] proposed a hypothesis that relates the Reynolds stress components to the average velocity:

$$\overline{\rho v_i' v_j'} = 2\mu_t \left(\frac{\partial \overline{u}_i}{\partial x_j} + \frac{\partial \overline{u}_j}{\partial x_i} \right) - \frac{2}{3} \left(\rho K + \mu_t \frac{\partial \overline{u}_k}{\partial x_k} \right) \delta_{ij} \tag{3.24}$$

where μ_t is the turbulent (or eddy) viscosity and K is the turbulent kinetic energy. The turbulent viscosity is not a physical descriptor of the fluid, it is dependent on the local flow conditions. More details on the turbulent viscosity are given in Section 4.3.

In the case when supplementary variables that are introduced by the turbulence models have to be calculated, the transport equation is:

$$\frac{\partial \overline{\rho \phi}}{\partial t} + \nabla \cdot (\overline{\rho \boldsymbol{v}} \phi) = \nabla \cdot \left(a \nabla \phi - \overline{\rho \boldsymbol{v}' \phi} \right) + S_\phi \tag{3.25}$$

where S_ϕ is the source term for the supplementary variable. Supplemental variables, such as the turbulence kinetic energy or dissipation rate for which Equation (3.25) is solved are introduced in Section 4.3.

CHAPTER 4

Computational Fluid Dynamics (CFD)

Computational Fluid Dynamics (CFD) is a field within fluid mechanics that deals with solving fluid flow-related problems through numerical analysis. The Navier-Stokes equations presented in Section 3.1 are Partial Differential Equation (PDE) and can only be solved analytically for very simple problems. For complicated tasks, the PDEs can be expressed as a set of linear equations, which then can be solved iteratively using computational resources.

4.1 Discretization

The physical space where the flow needs to be calculated can be broken down into a number of smaller geometrical components, the entire assembly of which is called a grid or mesh. This process is referred to in the literature as mesh generation [27]. The mesh elements are usually 2- (triangle, quadrilateral) or 3-dimensional (tetrahedron, hexahedron) shapes. The mesh requirements are application-dependent. However, in all cases, the mesh must be constructed in a way that no unexpected variation in cell volumes occurs. A mesh consists of several elements and nodes. An element is defined as an assembly of nodes that connect the geometrical points on each mesh element. Figure 4.1 illustrates the elements and nodes.
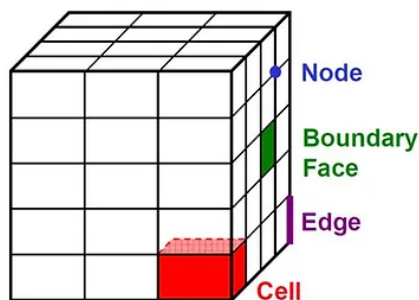

Figure 4.1: *Graphics showing a mesh element or cell, a node, boundary face and edge. Source: [33].*

There are several discretization methods, such as Finite Element Method (FEM), Finite Volume Method (FVM) or Finite Difference Method (FDM). The finite volume method is the most commonly used for CFD. There are two types of FVMs:

- Cell-centered: the variables are calculated at the center of every cell volume.

- Vertex-centered: the variables are calculated at the middle line that connects two nodes.

Figure 4.2 illustrates the difference between cell-centered and vertex-centered FVM discretization. The latter is a hybrid FEM-FVM discretization approach. More details can be found in Section 4.4.
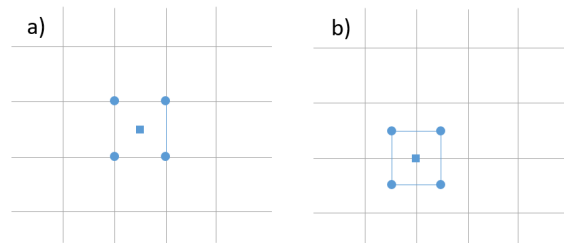
Figure 4.2: *The difference between (a) cell-centered and (b) vertex-centered finite volume method. Refurbished from [27].*

4.2   Turbulence Wall Modeling

Turbulence is a three-dimensional phenomenon that consists of many scales and happens when the fluid's inertia forces become comparable to the viscous forces; thus, Reynolds number (Re) is high [27]. A Direct Numerical Simulation (DNS) could provide further insights (see Section 4.3). However, DNS simulations require higher computing power and cannot be performed for complex geometries. To overcome this issue, CFD research is focused on deriving turbulence models, which can account for the turbulence phenomenon statistically and, thus, save computational resources. One of the most important concepts regarding turbulence in CFD is modeling the flow in the wall vicinity.

In CFD, it is common practice that the near-wall region is considered as three layers; one almost laminar viscous sublayer where viscosity is a crucial factor for momentum and heat transfer, and logarithmic layer where turbulence is the primary mechanism for heat and momentum transfer. The zone where the sublayer and logarithmic layer mix is considered a buffer layer. To evaluate the flow velocity dependence on the wall distance, it is helpful to define dimensionless parameters that can be used universally such as the dimensionless velocity, temperature and wall distance.

The dimensionless wall distance y^+ can be written in terms of the density ρ, friction velocity u_τ[1], viscosity μ and distance from the wall y as:

---

[1]The friction or shear velocity is shear stress expressed in units of velocity. In other words, $u_\tau = \sqrt{\tau/\rho}$

$$y^+ = \frac{\rho y u_\tau}{\mu} \tag{4.1}$$

The evolution of the non-dimensional velocity u^+ in terms of y^+ is linear in the viscous sublayer region:

$$u^+ = y^+ \tag{4.2}$$

In the logarithmic layer, the dimensionless velocity can be determined as the ratio between the local velocity tangent to the wall u_t and the friction velocity u_τ:

$$u^+ = \frac{u_t}{u_\tau} = \frac{1}{\kappa} ln(y^+) + C \tag{4.3}$$

where κ is the von Karman constant with a value of 0.41 [34]. C is a constant that depends on the wall roughness. The friction velocity u_τ is calculated as:

$$u_\tau = \left(\frac{\tau_w}{\rho}\right)^{1/2} \tag{4.4}$$

The velocity at the blending region can be calculated by blending the viscous sublayer and logarithmic layer [35].

Figure 4.3 shows the evolution of the dimensionless velocity u^+ in terms of the dimensionless wall distance y^+. This plot is also known in the literature as the *universal law of the wall* [19].
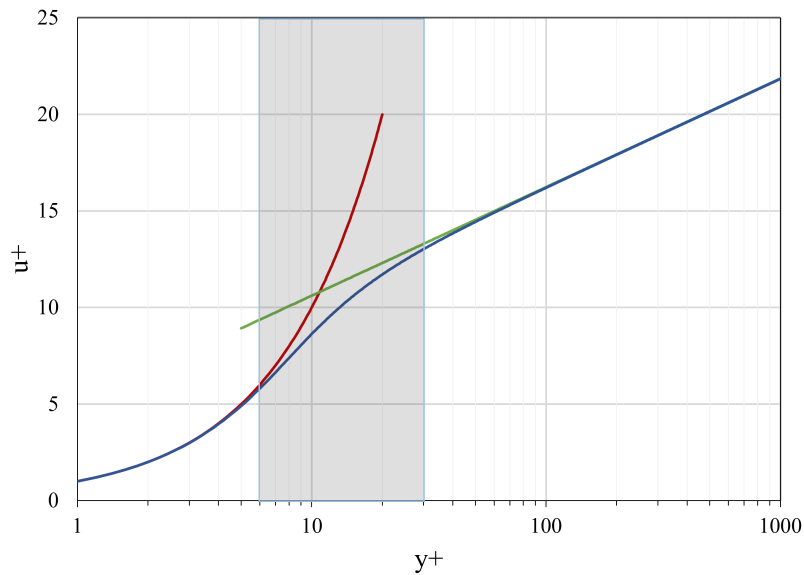

Figure 4.3: *Universal law of the wall. The red line shows the linear behavior in the viscous sublayer, the green curve shows the logarithmic law and the blue curve shows the universal law that includes all regions. The gray-colored area shows the buffer layer. Refurbished from [19].*

The dimensionless temperature in the viscous sublayer is linearly related to the dimensionless wall distance y^+ via the Prandtl number (Pr) number:

$$T^+ = \text{Pr} \cdot y^+ \tag{4.5}$$

In the logarithmic region T^+ can be written as:

$$T^+ \approx \frac{Pr_t}{\kappa} \ln y^+ + A(Pr) \tag{4.6}$$

where:

$$A(Pr) = \left(3.85 Pr^{(}1/3) - 1.3\right)^2 + \frac{Pr_t}{\kappa} \ln Pr \tag{4.7}$$

Pr_t is the turbulent Pr number and it is calculated as the ratio between momentum turbulent diffusivity and thermal turbulent diffusivity. The physical meaning of Pr_t is the quantification of how quickly momentum is transferred compared to how quickly heat is transferred within the turbulent flow [25, 36]. Pr_t is usually equal to 0.9 in Ansys CFX [35].

4.2.1 Wall Functions

To fully resolve the viscous sublayer in CFD, very fine mesh cells are needed close to the wall, which can easily increase the need for computational effort. In order to skip the necessity of very fine meshes close to the wall, the wall function approach can be used. Wall functions are empirical correlations that bridge the viscous sublayer region. These equations connect the wall shear stress to the dependent variables without resolving the boundary layer. In Ansys CFX (CFX), the near wall modeling is based on an extension of the method developed by Launder and Spalding [37]. The dimensionless velocity of the viscous sublayer and logarithmic region intersect at a y^+ value of 11.25 in the buffer region. In general, it is recommended the y^+ should be smaller than 5 (turbulence model dependent) in the case that the viscous sublayer is to be resolved and larger than 30 when the wall functions are used [35][38].

One drawback of the wall function approach is the sensitivity of the results to the location of the nearest point to the wall. Refining the mesh at the wall does not necessarily provide a unique solution and increase accuracy. Therefore, to tackle the inconsistencies of the wall function formulation, the scalable wall functions were introduced in CFX.

Scalable Wall Functions

Equation (4.3) becomes singular when the near wall velocity u_t is zero. Therefore, a different velocity scale u^* is defined for the logarithmic region such that it does not result in zero if u_t is zero:

$$u^* = C_\mu^{1/4}\sqrt{k} \tag{4.8}$$

where C_μ is a constant with value 0.09.

Analogously, an alternative dimensionless wall distance variable is defined as:

$$y^* = \frac{\rho u^* y}{\mu} \tag{4.9}$$

It is important to note that y^* is the same concept as y^+. The different notation of star and plus is related to whether the dimensionless wall distance is calculated by using the wall shear stress (Equation (4.1)) or the turbulent kinetic energy (Equation (4.9)).

Scalable wall functions are able to limit the y^* to a lower value, that is the intersection between linear and logarithmic regions [35]. This means that the mesh points lay surely outside the viscous sublayer. Using scalable wall functions essentially means that arbitrary fine meshes can be used without deciding whether the wall functions are feasible. Therefore, the velocity law is modified, and u^* cannot take zero values.

For the scalable wall functions the dimensionless temperature can be calculated as:

$$T^+ = 2.12\ln(y^*) + \beta \tag{4.10}$$

where:

$$\beta = \left(3.85 Pr^{1/3} - 1.3\right)^2 + 2.12\ln(Pr) \tag{4.11}$$

However, the scalable wall function formulation is cumbersome for low Re numbers, since the viscous sublayer is completely ignored in the mass and momentum balance equation.

Automatic Wall Functions

Automatic wall functions rely on a continuous function acting on the entire range of y^+ and switching automatically between the wall function and low Re number formulation [35]. This approach provides an advantage to the scalable wall functions described in Section 4.2.1. CFD codes first evaluate the y^+ value then select the appropriate formulation or apply blending functions to bridge the buffer layer. The dimensionless velocity is calculated in the same approach as shown in Equations (4.1) and (4.3). The thermal boundary layer when using automatic wall functions is expressed as:

$$T^+ = Pry^* \exp(-\Gamma) + [2.12 \ln(y^*) + \beta] \exp(1 - \Gamma) \tag{4.12}$$

where β is calculated by Equation (4.11) and Γ is defined as:

$$\Gamma = \frac{0.01(Pry^*)^4}{1 + 5Pr^3 y^*} \tag{4.13}$$

Roughness

In reality, surfaces have roughness, which means that there is an increase of turbulence production near a wall and therefore the shear stress and wall heat transfer coefficients can experience significant enhancement. Taking into account the wall roughness, the logarithmic velocity profile will shift closer to the wall as shown in Figure 4.4. The notion of sand grain roughness is employed to account for the surface roughness effect. The sand grain roughness averages the roughness with different shapes and sizes by implying that the wall consists of closely packed spheres with an average roughness height h_s [19], as illustrated in Figure 4.5.
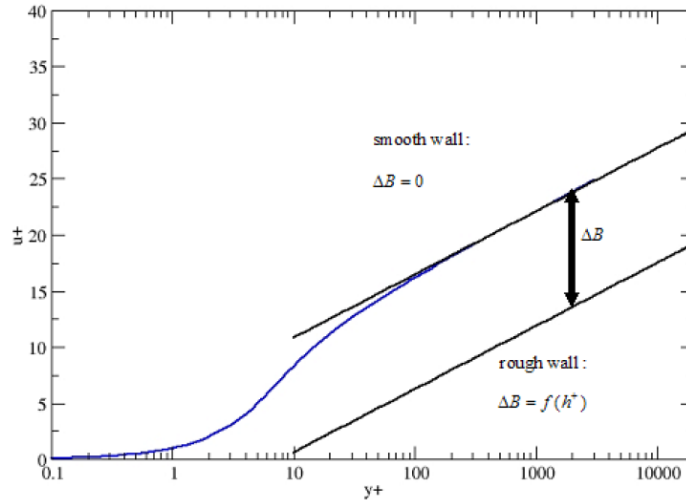
Figure 4.4: *Due to roughness, the wall shear stress is enhanced compared to a hydraulically smooth wall. Therefore, the velocity profile is shifted downward (closer to the wall) by ΔB [35][35].*

The dimensionless velocity can be expressed taking into account the roughness as:

$$u^+ = \frac{1}{\kappa} \ln y^+ + C - \Delta B \tag{4.14}$$

where C is a constant equal to 5 [19]. ΔB represents the downward shift of the profile and it is a function of the dimensionless roughness height h^+:

$$\Delta B = \frac{1}{\kappa} \ln(1 + 0.3h_s^+) \tag{4.15}$$

where:

$$h^+ = \frac{h u_\tau}{\nu} \tag{4.16}$$
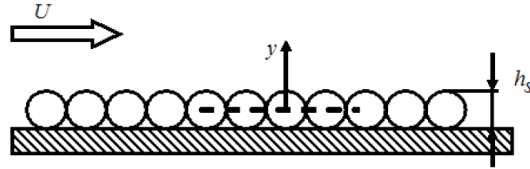
Figure 4.5: *Sand grain roughness concept. The average height of the technical roughness can be approximated to a surface covered with closely-packed spheres with a diameter h_s. Source: [19][35].*

The thermal boundary layer in the logarithmic region is expressed by:

$$T_{log}^+ = 2.12 \ln(Pry^*) + (3.85 Pr^{1/3} - 1.3)^2 - \frac{1}{\kappa} \ln(1 + 0.3 BPr h_s^+) \tag{4.17}$$

where B is the energy calibration coefficient with a value of 0.2. B was calibrated using the data obtained by a heat transfer experiment performed on a flat plate [35]. It is important to mention that this experiment used air as the fluid medium; however, Lechner and Menter showed in 2004 that 0.2 is a reasonable value for water as well [39].

It is important to note that for values $h_s^+ > 70$, the application of blending function in the SST turbulence model becomes rather unphysical due to the disappearing of the viscous sublayer [35].

4.3 Turbulence Models

Prior to getting into details concerning turbulence models, a few key concepts and parameters are introduced. Turbulence is one of the most complicated processes of fluid mechanics. Over the last two centuries, scientists like Landau [40], Prandtl [41] and Kolmogorov [42] have contributed to developing an understanding of turbulence and its properties. The turbulent length scale is defined in literature as a measure of the size of the largest eddies[2] present in the flow [29]. It was suggested by Richardson [44] that the large eddies break down into smaller ones. The energy is transferred from a large eddy to a smaller one without dissipation until the small eddies take the energy out of the system via viscous forces (low Re numbers). This is called the energy cascade process [29]. The turbulent dissipation ϵ defines the amount of turbulent kinetic energy that is transformed into thermal energy. The turbulent dissipation rate ω defines the amount of turbulent kinetic energy that is transformed into thermal energy per unit of turbulent kinetic energy.

---

[2]The eddies have a very loose definition. In his book "Turbulent Flows" [43], Pope writes, "An 'eddy' eludes precise definition, but it is conceived to be a turbulent motion, localized within a region of size l, that is at least moderately coherent over this region".

The development of turbulence modeling is a fast-changing field. There are several approaches to model turbulence such as Direct Numerical Simulation (DNS) [45], Large Eddy Simulation (LES) [46], Detached Eddy Simulation (DES) [47] and Reynolds-Averaged Navier-Stokes (RANS). DNS simulations involve very fine meshes to resolve all scales of turbulence without using turbulence models. It is mostly used for research concerning turbulence. The computational effort of DNS is very high even for simple geometries and flows with low Re numbers. LES deals with modeling only the large eddies while filtering out the smaller ones. DES uses the RANS modeling in the regions where the turbulence length scale is smaller than the mesh size and LES for the regions where the turbulence length scale is larger than the mesh size. As explained in Chapter 3.2, RANS turbulence modeling relies on the time averaging of the flow properties such as velocity and the modeling of the Reynolds stress terms that arise from the averaging process. RANS can be further sub-categorized into the Boussinesq hypothesis and Reynold Stress (RS) models. Boussinesq's hypothesis relates the Reynolds stress to the turbulent viscosity (see Chapter 3.2), while RS models solves transport equations for the Reynolds stress components [19].

K-ϵ, K-ω and Shear Stress Transport (SST) are two-equation turbulence models widely used due to their numerical robustness and the satisfactory level of numerical effort [48]. The name originates from the fact that they use two separate transport equations, one for the velocity (kinetic energy K), and the other for the turbulence length scale. Both are based on the gradient diffusion hypothesis and they relate the Reynolds stresses to the average velocity gradients and turbulent viscosity as expressed in Equation (3.24). The turbulent kinetic energy K is calculated from the solution of its transport equation, and the same is done for the dissipation rate. Then, the turbulence velocity and length scales are estimated from the turbulent kinetic energy and dissipation rate. All the turbulence models aim at modeling the Reynolds stress defined in Equation (3.24), where the turbulence viscosity μ_t plays an important role. The turbulence viscosity is a modeling approach used to account for turbulence. In other words, in a laminar flow, the diffusion in the flow occurs by molecular motion, while in a turbulent flow, the eddies also play a role to diffusion. Therefore, in turbulence modeling, the diffusion is enhanced by including the turbulent viscosity in addition to the molecular viscosity. The quantity of turbulence intensity I can be defined based on viscosity μ and turbulent viscosity μ_t such that:

$$I = 0.001 \frac{\mu_t}{\mu} \tag{4.18}$$

Furthermore, the turbulent kinetic energy K can be determined in terms of Reynolds stress:

$$K = \frac{1}{2} \sum_i \overline{v_i' \cdot v_i'} \tag{4.19}$$

4.3.1   K-ϵ

K-ϵ is a rather standard turbulence model used widely in industry. This model deals with modeling the turbulent kinetic energy K and the turbulent dissipation rate ϵ [35]. One of the assumptions made is that the turbulent viscosity μ_t is related to the turbulent kinetic energy as:

$$\mu_t = C_\mu \rho \frac{K^2}{\epsilon} \tag{4.20}$$

where C_μ is a constant with value of 0.09. The turbulent kinetic energy K can be calculated using Equation (4.19), while the turbulent dissipation rate ϵ that determines the turbulence length scale is calculated as:

$$\epsilon = \nu \cdot \overline{\frac{\partial v_i'}{\partial x_k} \cdot \frac{\partial v_i'}{\partial x_k}} \tag{4.21}$$

For both K and ϵ, transport Equation (4.3) is used.

The major disadvantage of K-ϵ is the inability to model the low-Reynolds number flows close to the heated walls. For heated walls, a very fine mesh with a y$^+$ value (see Equation (4.1)) smaller than 0.2 would be necessary to adequately describe the heat transfer processes in the near wall regions.

4.3.2   K-ω

Similarly to K-ϵ, K-ω is also a two-equation model dealing with the turbulent kinetic energy K and the turbulent frequency ω [49]. This model reflects the fact that the turbulent viscosity is proportional to the kinetic energy and inversely proportional to the turbulent frequency:

$$\mu_t = \rho \frac{K}{\omega} \tag{4.22}$$

where ω represents the time scale of the turbulence.

For K-ω, two transport equations are solved, one for the turbulent kinetic energy K and the other for the turbulent frequency ω. The main advantage of K-ω over K-ϵ is that it deals better with the near wall region for low Re number calculations. To be able to resolve the viscous sublayer, a y$^+$ value smaller than 2 would be required. A substantial disadvantage of K-ω is the large sensitivity to the initial conditions of the free stream.

4.3.3   Shear Stress Transport (SST) Model

The baseline K-ω model (BSL) was developed to deal with K-ω's inability to properly predict the free stream by combining Wilcox's K-ω model and K-ϵ. However big these efforts were, BSL

still failed to deal with the flow separation from smooth surfaces. Furthermore, BSL did not account for the turbulent shear stress, and thus it led to an overprediction of the eddy viscosity. Therefore, the SST model was developed with the aim of overcoming these issues [50]. SST uses the potential of K-ω to model the inner part of the boundary layer and K-ϵ for the free stream. An important feature of the SST model is the introduction of a factor that limits the behavior of eddy viscosity, making it possible to calculate flows with strong pressure gradients and boundary layer separation [27]. The switching between K-ϵ and K-ω formulations is done through blending functions, which control the switching on and off of the two models [35]. The formulation of the blending functions is based on the distance to the nearest surface. For more details on the blending functions, the interested reader can refer to literature [27] and the Ansys CFX theory guide [35].

In general, SST calculates lower wall temperatures compared to K-ϵ, which leads to higher heat transfer coefficients.

4.3.4 Reynolds Stress Models

Reynolds stress models (also called second-moment closure models), unlike the previously discussed turbulence models, do not use the eddy viscosity hypothesis but rather calculate all the components of the Reynolds stress tensor [51].

Since the Reynolds stress tensor is symmetric, there are six equations to solve in total. These equations have the form of:

$$\overline{v_i}\frac{\partial \overline{v_i v_j}}{\partial x} + \overline{v_j}\frac{\partial \overline{v_i v_j}}{\partial y} = D_{ij} + P_{ij} - \epsilon_{ij} + \Phi_{ij} \tag{4.23}$$

The terms on the left-hand side of Equation (4.23) are the convection terms. Furthermore, D_{ij} accounts for the diffusion, Φ_{ij} is the pressure-strain correlation, P_{ij} is the production term and ϵ_{ij} is the dissipation term.

The pressure-strain correlation is an important term for RS models since it drives turbulence toward an isotropic state by redistributing the Reynolds stresses. Several RS models are available, and LRR-IP and LRR-QI models use linear pressure-strain correlation. The SSG model, on the other hand, uses a quadratic relation [35].

4.4 Ansys CFX Solver

The theory presented here is based on Ansys CFX Solver Theory Guide [35]. CFX uses a hybrid finite element-finite volume approach together with a discretizing grid. This means the vertex-based finite volume method is used to construct the mesh. This denotes an element with multiple nodes depending on the shape of the element and solving order. The relevant quantities
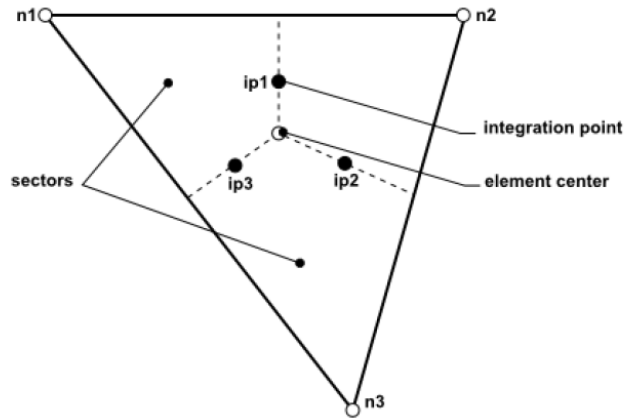
Figure 4.6: *Mesh element in Ansys CFX. Source [35].*

during solution are stored in nodes, while the conservation of quantities such as momentum, mass, and energy is done in each volume. Around each node, a control volume is constructed, whose corners are defined by the median of the line connecting two nodes, also called integration points. Equation (3.14) is integrated over the control volume and the Gauss divergence theorem is applied, provided that the control volumes do not exhibit deformation in time steps. Volume integrals are discretized in each volume sector and then summed to the control volume. Figure 4.6 shows schematics of nodes, volume sector and control volume in a 2D element. The volume integrals are calculated at the element sectors, then summed up at the control volume where the sector belongs. Surface integrals are evaluated at integration points and then assigned to the adjacent control volume.

4.4.1 Calculations of Special Terms

Shape Functions

The solution variables are stored at mesh nodes; however, evaluating solution fields and gradients requires approximating solutions at the integration point. This constitutes to a finite element method and it is done in CFX by shape functions that essentially describe a variable's development within one element by means of linear approximations:

$$X = \sum_{i=1}^{N_{node}} N_i X_i \tag{4.24}$$

where N_i are the shape functions at each node, and X_i is the variable value at each node i.

This work uses hexahedral and tetrahedral elements for CFD discretization. A hexahedral linear element has 8 nodes and therefore 8 shape functions, while a tetrahedral element has 4 nodes and 4 shape functions. Figure 4.7 shows both element types and the corresponding nodes.
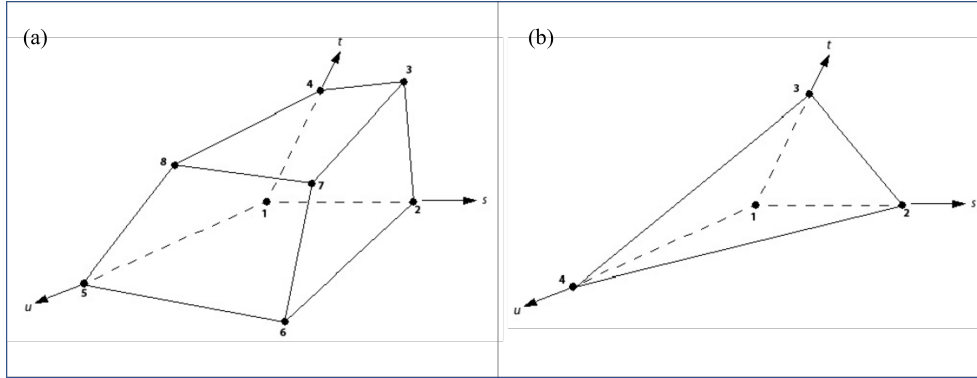
Figure 4.7: *Hexahedral (a) and tetrahedral (b) element types in CFX. Source [35].*

Control Volume Gradients

In the event that the gradients need to be calculated at nodes, a form of Gauss' divergence theorem is employed by CFX to calculate the control volume gradients such that:

$$\nabla X = \frac{1}{V} \sum_{ip} (X \Delta \boldsymbol{n})_{ip} \tag{4.25}$$

$\Delta \boldsymbol{n}$ is the outward normal vector at the integration point *ip*. It is important to note that in order to be able to use this formula, the variable X has to be calculated at the integration points by means of shape functions.

Diffusion Terms

The diffusion of heat in a domain is also calculated by using shape functions:

$$\left. \frac{\partial X}{\partial x} \right|_{ip} = \sum_n \left. \frac{\partial N_n}{\partial x} \right|_{ip} X_n \tag{4.26}$$

Mesh Deformation

In the Fluid-Structure Interaction (FSI) calculations, the CFD mesh is subject to deformation. Therefore, Equation (3.14) is modified to account for the change of control volumes in time steps. The modifications include the application of Leibniz rule and differentiation under the integral sign:

$$\frac{d}{dt} \int_{V(t)} X dV = \int_V \frac{\partial X}{\partial t} dV + \int_S X \boldsymbol{W_j} dn_j \tag{4.27}$$

where W_j is the velocity of the control volume boundary.

The Coupled Equation System

CFX uses a coupled system of equations to solve for the field variables. The application of the finite element method in the domain gives rise to a system of linear equations written in such form:

$$\sum_{nb_i} a_i^{nb} X_i^{nb} = b_i \tag{4.28}$$

where the subscript *nb* stands for neighbors of the node i. *b*, *a* and *X* are scalars for scalar equations. They are matrices and vectors for the coupled 3D mass-momentum equations.

4.4.2 Ansys CFX Solution Strategy

CFX uses the coupled equation system shown in Equation (4.28), which is also called a coupled solver since it solves the hydrodynamic equations for all the velocity components and pressure as a single system. This approach is robust and efficient as opposed to segregated solvers[3]. The drawback of coupled solvers is a large amount of memory needed to store all the coefficients of the linear set of equations. Furthermore, Ansys CFX uses a so-called acceleration parameter as a time step notion in the steady state solver. This helps approximate the solutions within a physically based manner, and the convergence is reached within a reasonable number of iterations.

Figure 4.8 shows the general solution process. The solver performs two numerically intensive processes in each iteration. First, the linearization of nonlinear equations takes place and are gathered into the solution matrix. Then, the linear equations are solved using a Multigrid (MG) accelerated Incomplete Lower Upper (ILU) factorization technique.

The ILU technique is an iteration process that starts the solving by stating an approximate solution. For example, if the system of equations resulting from discretization has the form:

$$[A][X] = [b] \tag{4.29}$$

where [A], [X] and [b] are the coefficient matrix, solution vector and the right-hand side of the equation.

The iterative process starts with an approximate solution $[X_n]$ that will be improved by a correction [X']:

$$[X_{n+1}] = [X_n] + [X'] \tag{4.30}$$

---

[3]Segregated solvers solve first the momentum equations using a guess value for the pressure to obtain a correction equation for the pressure.
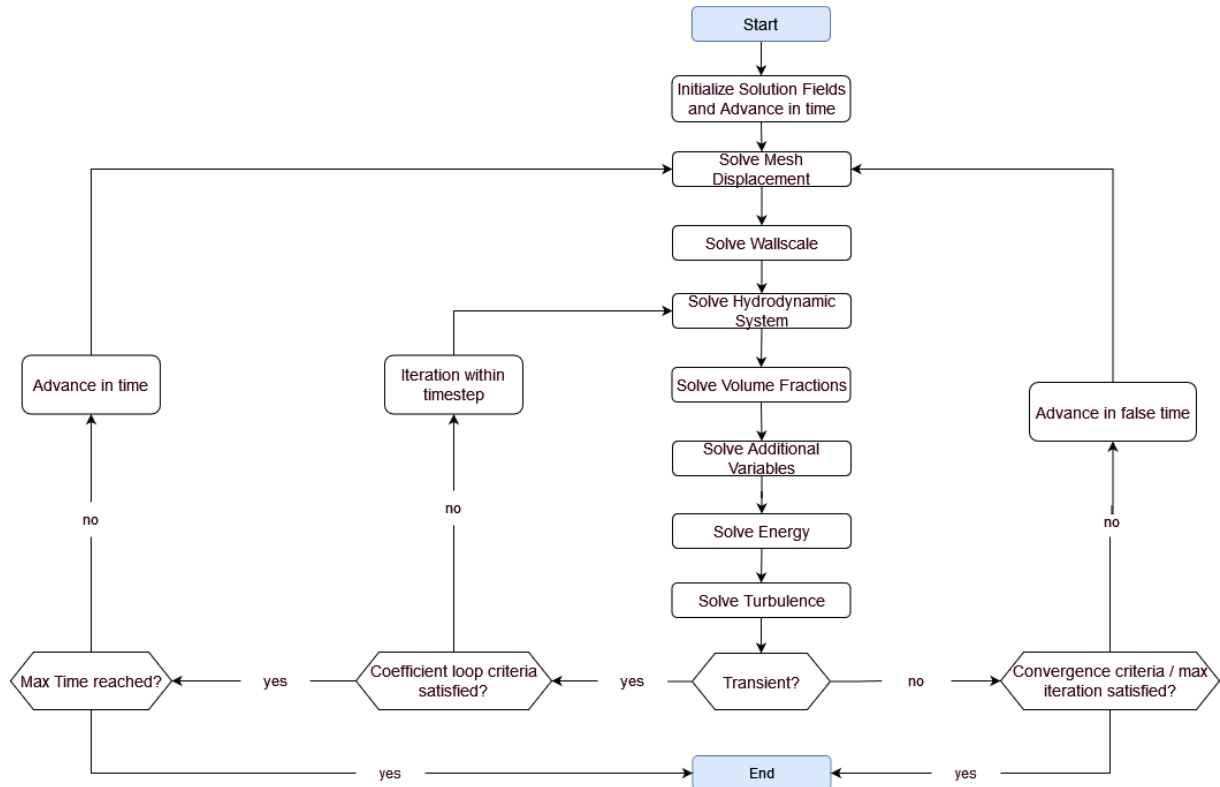
Figure 4.8: *Flowchart of the CFX solver. Source: [35].*

where [X'] is the solution obtained from:

$$[A][X'] = [r_n] \tag{4.31}$$

Moreover, $[r_n]$ is the residual defined as:

$$[r_n] = b - [A][X_n] \tag{4.32}$$

Iterative solvers can only reduce discretization errors with a wavelength comparable in order of magnitude to the mesh size. Therefore, for a fine mesh, the short wavelength errors disappear relatively fast, however, the longer wavelength ones do not. This problem is overcome by the usage of the Multigrid method [52] since coarser meshes are built where the longer wavelength errors appear as short wavelength errors with respect to the mesh size. To avert the need for re-meshing the geometry with a set of different mesh sizes, CFX uses the Algebraic Multigrid. The Algebraic Multigrid sums up the fine mesh equations to build a discrete equation system for a coarse mesh. The mesh is coarsened in a virtual manner without user intervention. This essentially means that the early iterations are performed on a fine mesh that coarsens out continuously. The results are finally transferred to the original mesh to obtain a more accurate solution with fewer discretization errors. Algebraic Multigrid's main advantage is the reduced computational expense since the nonlinear equations are only discretized once for the finest mesh. The particular

implementation of the Algebraic Multigrid used by CFX is called Additive Correction. The reason behind this is the suitability of this approach to the CFX solver implementation. More specifically, taking into account that the discrete equations represent the conservation of quantities in a control volume, the coarse mesh equations can be built by joining the small control volumes to form larger ones. Therefore, the coarse mesh equations also establish conservation over large control volumes, reducing the errors components. A small schematic of Algebraic Multigrid is shown in Figure 4.9.
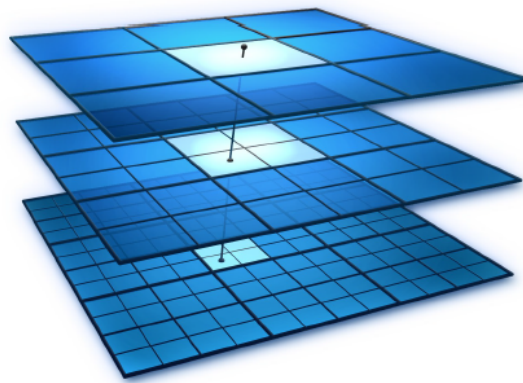

Figure 4.9: *Schematics of the Algebraic Multigrid method going from fine meshes to coarser ones. The process starts with the most lower plane (fine mesh). As the solver progresses, the mesh is coarsened out in a virtual manner. Finally, the final results are mapped into the fine mesh. Source [12].*

Part II

Mechanics

CHAPTER 5

Structural and Thermal Mechanics

This part consists of two chapters, the first including a theoretical background of structural and thermal mechanics as well as their implementation into Ansys. The second provides more details on the finite element method. It is crucial to note that in the Mechanics part, the vector notation is done by using curly brackets:

- $\{V\}$ represents a column vector.

- The subscript T means that the matrix or vector is transposed.

- $\{V\}^T$ represents the transpose of a column vector, which is a row vector.

- $[M]$ is a matrix.

The information given in the next two chapters is mainly based on [17, 53–55] and the Ansys Mechanical Theory Reference [56], and oftentimes appended with the locally mentioned references.

5.1 The Structural System

Hooke's law is one of the basic principles upon which the theory of elasticity is developed. It suggests that the force needed to deform a spring by a distance is proportional to that distance and a constant. For continuous media, Hooke's law can be written as:

$$[K]\{u\} = \{F\} \tag{5.1}$$

where $[K]$ is the stiffness matrix, $\{u\}$ is the vector of displacement and $\{F\}$ is the applied force.

A structure's response to a load can be linear or nonlinear. A linear behavior would imply that the displacement is directly proportional to the applied load, meaning that the stiffness matrix

remains constant with the applied load. On the other hand, when the response is nonlinear, the displacement and the applied load are non-linearly related. Therefore, the stiffness matrix is not constant in terms of load steps.

One of the primary relations, arguably the most important in structural mechanics, is the relationship between stress and strain, which is another way of expressing Hooke's Law. In this section, only a linear behavior is considered, whereas the nonlinear one is described later in Section 5.3. For a linear behavior, it holds:

$$\{\sigma\} = [D]\left\{\epsilon^{el}\right\} \tag{5.2}$$

where $\{\sigma\}$ is the stress vector whose component are also shown in Figure 5.1, $[D]$ is the elasticity matrix and $\left\{\epsilon^{el}\right\}$ is the elastic strain vector.

The total strain vector is defined as the sum of the elastic strain and the thermal strain vectors:

$$\{\epsilon\} = \left\{\epsilon^{el}\right\} + \left\{\epsilon^{th}\right\} = \begin{bmatrix} \epsilon_x & \epsilon_y & \epsilon_z & \epsilon_{xy} & \epsilon_{yz} & \epsilon_{xz} \end{bmatrix}^T \tag{5.3}$$

The shear strain components $\epsilon_{xy}, \epsilon_{yz}, \epsilon_{xz}$ are twice the tensor shear strains.

In order to include the thermal strain, Equation 5.2 can be written as:

$$\{\epsilon\} = \left\{\epsilon^{th}\right\} + [D]^{-1}\sigma \tag{5.4}$$

The thermal strain for a 3D case is defined as:

$$\left\{\epsilon^{th}\right\} = \Delta T [\alpha_x^{se} \quad \alpha_y^{se} \quad \alpha_z^{se} \quad 0 \quad 0 \quad 0]^T \tag{5.5}$$
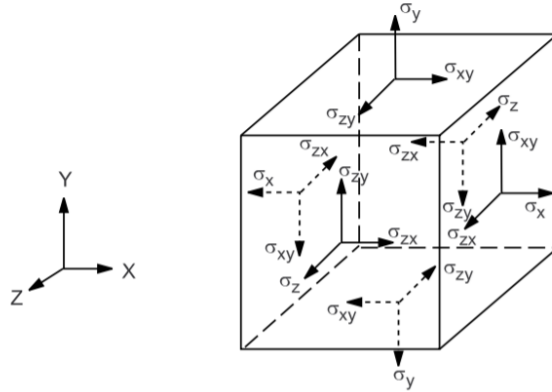

Figure 5.1: *The definition of the stress vector. The shear stresses are denoted by double subscripts, while normal stresses are by single subscripts. Source [56].*

where α_x^{se} are the Secant coefficients of thermal expansion in all three directions. ΔT is defined as the difference between the current temperature at the point in question and a reference temperature.

The inverse of the elasticity matrix $[D]^{-1}$ can be defined as:

$$[D]^{-1} = \begin{bmatrix} 1/E_x & -\nu_{xy}/E_x & -\nu_{xz}/E_x & 0 & 0 & 0 \\ -\nu_{yx}/E_y & 1/E_y & -\nu_{yz}/E_y & 0 & 0 & 0 \\ -\nu_{zx}/E_z & -\nu_{zy}/E_z & 1/E_z & 0 & 0 & 0 \\ 0 & 0 & 0 & 1/G_{xy} & 0 & 0 \\ 0 & 0 & 0 & 0 & 1/G_{yz} & 0 \\ 0 & 0 & 0 & 0 & 0 & 1/G_{xz} \end{bmatrix} \tag{5.6}$$

where E_x is the x component of Young's modulus, ν_{xy} and ν_{yx} are the major and minor Poisson's ratios, respectively. G_{xy} is the xy component of the shear modulus.

In an orthotropic material, the symmetry of the $[D]^{-1}$ matrix relies on the fact that only three out of six Poisson's ratios are independent. The remaining can be calculated as:

$$\frac{\nu_{yx}}{E_y} = \frac{\nu_{xy}}{E_x}; \quad \frac{\nu_{zx}}{E_z} = \frac{\nu_{xz}}{E_x}; \quad \frac{\nu_{yz}}{E_y} = \frac{\nu_{zy}}{E_z} \tag{5.7}$$

Taking into account all the above relations, Equation 5.2 can be expressed in six explicit relations:

$$\sigma_x = \frac{E_x}{h} \left(1 - (\nu_{yz})^2 \frac{E_z}{E_y} \right) (\epsilon_x - \alpha_x \Delta T) + \frac{E_y}{h} \left(\nu_{xy} + \nu_{xz}\nu_{yz} \frac{E_z}{E_y} \right) (\epsilon_y - \alpha_y \Delta T) +$$
$$\frac{E_z}{h} \left(\nu_{xz} + \nu_{yz}\nu_{xy} \right) (\epsilon_z - \alpha_z \Delta T) \tag{5.8}$$

$$\sigma_y = \frac{E_y}{h} \left(\nu_{xy} + \nu_{xz}\nu_{yz} \frac{E_z}{E_y} \right) (\epsilon_x - \alpha_x \Delta T) + \frac{E_y}{h} \left(1 - (\nu_{xz})^2 \frac{E_z}{E_x} \right) (\epsilon_y - \alpha_y \Delta T) +$$
$$\frac{E_z}{h} \left(\nu_{yz} + \nu_{xz}\nu_{xy} \frac{E_y}{E_x} \right) (\epsilon_z - \alpha_z \Delta T) \tag{5.9}$$

$$\sigma_z = \frac{E_z}{h} \left(\nu_{xz} + \nu_{yz}\nu_{xy} \right) (\epsilon_x - \alpha_x \Delta T) + \frac{E_z}{h} \left(\nu_{yz} + \nu_{xz}\nu_{xy} \frac{E_y}{E_x} \right) (\epsilon_y - \alpha_y \Delta T) +$$
$$\frac{E_z}{h} \left(1 - (\nu_{xy})^2 \frac{E_y}{E_x} \right) (\epsilon_z - \alpha_z \Delta T) \tag{5.10}$$

$$\sigma_{xy} = G_{xy}\epsilon_{xy} \tag{5.11}$$

$$\sigma_{yz} = G_{yz}\epsilon_{yz} \tag{5.12}$$

$$\sigma_{xz} = G_{xz}\epsilon_{xz} \tag{5.13}$$

h is defined for simplicity reasons as:

$$h = 1 - (\nu_{xy})^2 \frac{E_y}{E_x} - (\nu_{yz})^2 \frac{E_z}{E_y} - (\nu_{xz})^2 \frac{E_z}{E_x} - 2\nu_{xy}\nu_{yz}\nu_{xz}\frac{E_z}{E_x} \tag{5.14}$$

$\epsilon_{x,y,z}$ and $\sigma_{x,y,z}$ describe the direct strain and stress terms, and $\epsilon_{xy,yz,xz}$ and $\sigma_{xy,yz,xz}$ the shear strain and stress terms, respectively.

From Equation (5.7), one can deduct that if $E_x > E_y$ then $\nu_{xy} > \nu_{yx}$. In this case, ν_{xy} is the major Poisson's ratio and ν_{yx} is the minor. However, for isotropic materials, all the components of Young's modulus are equal; therefore, Poisson's ratio's components are also equal.

If the material under study is isotropic, the shear modulus components are not input parameters. They are instead calculated as:

$$G_{xy} = G_{yz} = G_{xz} = \frac{E}{2(1+\nu)} \tag{5.15}$$

5.1.1 Von Mises Theory

The total stress $\{\sigma\}$ can be expressed as a sum of hydrostatic and deviatoric stresses. The same holds for strain. The hydrostatic stress, also known as volumetric stress, causes changes only in the volume without triggering a change in shape, and it can be calculated as the average of the normal components of a stress tensor, also shown in Figure 5.1.

$$\sigma_{Hyd} = \frac{\sigma_{xx} + \sigma_{yy} + \sigma_{zz}}{3} \tag{5.16}$$

The deviatoric stress is in charge of shearing and distortion, and it is calculated as a difference between the total stress and the hydrostatic stress:

$$\{\sigma_d\} = \{\sigma\} - \{\sigma_{Hyd}\} \tag{5.17}$$

The limits of elasticity are usually based on uniaxial stress tests. The von Mises theory [57], also known as the maximum distortion energy theory, suggests that the structure fails when the maximum distortion energy equals the distortion energy when yielding in a uniaxial test. The distortion energy W_d refers to the strain energy corresponding to the effect of deviatoric stresses in the stress tensor. W_d per unit volume can be calculated as:

$$W_d = \frac{1+\nu}{6E}\left[(\sigma_1 - \sigma_2)^2 + (\sigma_2 - \sigma_3)^2 + (\sigma_3 - \sigma_1)^2\right] \tag{5.18}$$

where σ_1, σ_2 and σ_3 are the three principal stress components[1].

The maximum principal stress equals the material's yield strength during a stress test. The rest of the principal stresses are zero. Therefore, the distortion energy when yielding in a uniaxial (y) stress test can be calculated as:

$$W_{d,y} = \frac{1 + \nu}{3E} \sigma_y^2 \tag{5.19}$$

By equalizing the Equations (5.18) and (5.19), von Mises failure criteria in terms of principal stresses and stress tensor components are obtained:

$$
\begin{aligned}
\sigma_e &= \sqrt{\frac{1}{2} \left(\sigma_1 - \sigma_2\right)^2 + \left(\sigma_2 - \sigma_3\right)^2 + \left(\sigma_3 - \sigma_1\right)^2} \\
&= \sqrt{\frac{1}{2} \left(\sigma_{xx} - \sigma_{yy}\right)^2 + \left(\sigma_{yy} - \sigma_{zz}\right)^2 + \left(\sigma_{zz} - \sigma_{xx}\right)^2 + 6 \left(\sigma_{xy}^2 + \sigma_{yz}^2 + \sigma_{zx}^2\right)}
\end{aligned} \tag{5.20}
$$

σ_e is called the equivalent von Mises stress. It states that the structure has deformed if the von Mises stress is reached.

5.1.2 Boundary Conditions

Generally, the most common boundary condition is a zero-displacement condition, which refers to a structure or element being fully fixed in all three directions. The fixed end of a cantilever beam is an example of this.

5.2 Heat Flow

The energy equation for solids in a differential control volume has the form [17]:

$$\rho c_p \left(\frac{\partial T}{\partial t} + \{v\}^T \nabla T\right) + \nabla \{q\} = \ddot{q} \tag{5.21}$$

where $\{v\}$ is the velocity vector for mass transport, $\{q\}$ is the heat flux vector and $\ddot{q}$ is the heat generation rate per unit volume.

In order to introduce a relation between the heat flux vector $\{q\}$ and the temperature gradients, the Fourier law (from Section 2.2) is applied:

$$\{q\} = -[D] \{L\} T \tag{5.22}$$

---

[1]The principal stress is defined as such that upon a basis change, the shear stress component is always zero. Mathematically speaking, principal stresses are the eigenvalues of the stress tensor

where [D] is the thermal conductivity matrix:

$$[D] = \begin{bmatrix} K_{XX} & 0 & 0 \\ 0 & K_{YY} & 0 \\ 0 & 0 & K_{ZZ} \end{bmatrix} \tag{5.23}$$

Moreover, $\{L\}$ is a vector operator defined as:

$$\{L\} = \begin{pmatrix} \frac{\partial}{\partial x} \\ \frac{\partial}{\partial y} \\ \frac{\partial}{\partial z} \end{pmatrix} \tag{5.24}$$

Combining Equation (5.22) and Equation (5.21) leads to:

$$\rho c_p \left(\frac{\partial T}{\partial t} + v_X \frac{\partial T}{\partial t} v_Y \frac{\partial T}{\partial t} v_Z \frac{\partial T}{\partial t} \right) = \ddot{q} + \frac{\partial}{\partial x} \left(K_X \frac{\partial}{\partial x} \right) + \frac{\partial}{\partial y} \left(K_Y \frac{\partial}{\partial y} \right) + \frac{\partial}{\partial z} \left(K_Z \frac{\partial}{\partial z} \right) \tag{5.25}$$

5.2.1   Boundary Conditions

The boundary conditions that can be applied to Equation (5.25) are:

- A specified temperature on a surface: $T = T^*$

- A specified flux on a surface: $\{q\}^T \{n\} = -q^*$, where $\{n\}$ is the normal unit vector and q^* is the specified heat flux.

- A specified convection applied to a surface, or better known as the Newton's law of cooling: $\{q\}^T \{n\} = h(T_s - T_b)$, where h is the heat transfer coefficient and T_s and T_b refer to the temperature of the surface of the model and the adjacent fluid temperature, respectively.

Combining Equation (5.21) and Equation (5.22):

$$\{n\}^T [D] \{L\} T = h(T_b - T_s) \tag{5.26}$$

5.3   Linear and Nonlinear Analysis

As mentioned in Chapter 5.1, a structure's response to a particular load can be linear or nonlinear. Similarly, there are linear and nonlinear types of structural analysis. Nonlinearity can be expressed as geometrical nonlinearity, material nonlinearity, or change of contact status during the analysis[2].

---

[2]For instance, if the initial contact is lost or changed during the load application.

Large deformations, rotations and stress stiffening are referred to as geometrical nonlinearities. The term large deformation is used in cases where the most significant deformations the structure undergoes are comparable to its smallest dimensions. The material nonlinearity is explained in detail in subsection 5.3.2.

5.3.1   Geometric Nonlinearities

Geometric nonlinearities imply a nonlinear structure behavior due to the changing geometry during deformation since the stiffness matrix $[K]$ is a function of the deformation $\{u\}$. Ansys Mechanical includes four types of geometrical nonlinearities [56]:

1. *Large deflection* is used when the largest deformations the structure undergo are comparable to its smallest dimensions. In this case, the strains are finite.

2. *Rotation* assumes that the structure does not exhibit a shape change other than rigid body dynamics. The rotations are significant, but the strains are still calculated with linear expressions.

3. *Stress stiffening* estimates that strain and rotations are minor, and a first-order approximation of the rotations is used for nonlinear effects.

4. *Spin Softening* accounts for the combinations of the transverse vibrational motion and the centrifugal force. Both strains and rotations are minor in this case.

Not all elements available in Ansys Mechanical support all the geometric nonlinearities. Only the large deformations are used in the mechanical analysis of Forschungs-Neutronenquelle Heinz Maier-Leibnitz (FRM II). In principle, the maximum predicted deformation for the FRM II plate is not expected to exceed 6% of the plate thickness. However, the large deformation implementation was used for research purposes. Therefore, this approach is explained further in detail here.

Large Deformation Theory

The motion of a body from one position to another under an applied load is assessed by examining the position vector of the deformed x and undeformed X conditions, also shown in Figure 5.2:

$$\{u\} = \{x\} - \{X\} \tag{5.27}$$

The change in deformation is then defined in terms of displacement as:

$$[F] = \frac{\partial \{x\}}{\partial \{X\}} = [I] + \frac{\partial \{u\}}{\partial \{X\}} \tag{5.28}$$
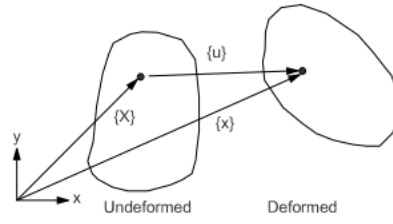
51

Figure 5.2: *Position vector of a deformed and undeformed body. Source [56].*

where $[I]$ is the identity matrix.

The volume change, rotation and shape change of the body are included in the change in deformation. Therefore, the volume change at one point can be calculated as:

$$\frac{dV}{dV_0} = \det[F] \tag{5.29}$$

where V_0 is the original volume, V the current volume and det the determinant of the matrix.

The deformation gradient can be expressed by rotation and shape change:

$$[F] = [R][U] \tag{5.30}$$

where $[R]$ is the rotation matrix and $[U]$ the shape change matrix.

When $[U]$ is known, the logarithmic strain measure can be defined as:

$$[\epsilon] = ln[U] \tag{5.31}$$

Since here $[\epsilon]$ is a matrix, not a vector as usual, a spectral decomposition of $[U]$ is needed:

$$[\epsilon] = \sum_{i=1}^{3} ln \ \lambda_i \ e_i \ e_i{}^T \tag{5.32}$$

where λ_i are the eigenvalues of $[U]$ and e_i the eigenvectors of $[U]$.

Implementation in Ansys Mechanical

The computation of Equation (5.31) can be done by following an incremental approximation such that:

$$[\Delta \epsilon_n] = \ln[\Delta U_n] \tag{5.33}$$

where n refers to the current time step. By expressing the incremental logarithmic strain in terms of the strain-displacement matrix and the incremental displacement, this method leads to the calculation of the position of the midpoint of the deformed geometry:

$$\left\{X_{1/2}\right\} = \frac{1}{2}\left(\{X_n\} + \{X_{n-1}\}\right) \tag{5.34}$$

where n-1 refers to the previous time step. This method is used to approximate the logarithmic strain when the strain steps are less than 10% and is employed in 2D and 3D element formulations. Furthermore, the element matrices and load vectors are derived based on the updated Lagrange formulation, which implies that all the variables refer to the last calculated state, not the original one.

5.3.2 Material Nonlinearities

The material nonlinearity is referred to the strain-strain relationship in Equation (5.2). The nonlinearity and the different ways of unloading make modeling nonlinear materials complicated. One thing that must be considered is the limit of this linear stress-strain dependence. For this purpose, one can examine the stress-strain plot of a ductile material shown in Figure 5.3. A linear behavior holds for small stresses and strains (linear analysis). This means that when a small load is applied in a way that no energy is lost in the process, the structure can return to its original state upon unloading. This is called the elastic region and is limited by the yield strength, which suggests that the deformations are irreversible above this limit. The yield strength defines the beginning of the plastic regime. The ultimate or tensile strength is the maximum stress value the material can withstand before rupturing. When the rupture stress is reached, a fracture of the structure is expected. The area under the curve in the plastic regime is equal to the energy the structure absorbs during the elongation of the compression process [58].

All the types of material nonlinearity except nonlinear elasticity and hyperelasticity have a path-dependent stress-strain relationship, which essentially means that the stress depends on the history of the strain [56].

- *Rate independent plasticity* refers to a small but irreversible strain in a material.

- *Rate dependent plasticity*, also referred to as viscoplasticity, implies the development of the plastic strains over a certain amount of time.

- *Creep* is very similar to both rate-dependent and independent plasticity, with the larger time frame.

- *Gasket Material* can be modeled using very specific relationships

- *Nonlinear elasticity* implies that a nonlinear stress-strain relation can be input; however, all straining is reversible.

- *Hyperelasticity* is referred to the strain energy density potential in foam-like materials. Also, here the straining is reversible.

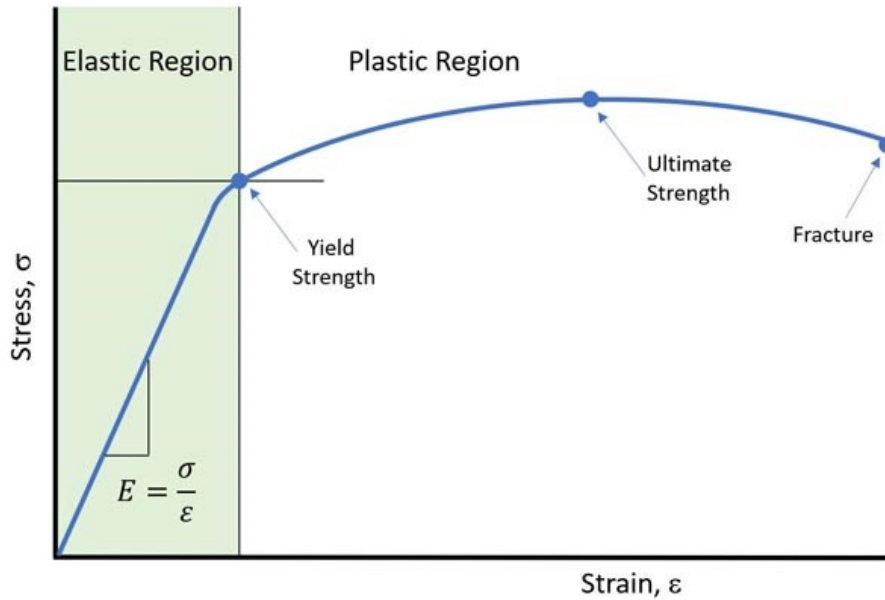- *Swelling* refers to enlarging materials due to neutron flux.

Figure 5.3: *Stress-strain relation for a ductile material. Source [58].*

Rate-independent plasticity

Rate-independent plasticity occurs in a material once a certain level of stress is reached, and it is called rate-independent because plasticity occurs instantaneously and not as a function of time steps [56].

A few concepts are necessary to grasp when talking about rate-independent plasticity. First, the von Mises failure criteria, explained in subsection 5.1.1, is employed in the rate-independent plasticity approach. That means the structure will obey the linear stress-strain relationship when an equivalent stress value is smaller than the yield stress. When the yield stress value is surpassed, the plastic strain in the structure will develop at once. Equation (5.20) can be expressed more easily as:

$$f(\{\sigma\}) = \sigma_y \tag{5.35}$$

where $f(\{\sigma\})$ is a function taking into account all the stress components.

The yielding direction of the structure is assumed to be always normal to the surface. This is called the flow rule. If the yielding is progressing, the hardening rule describes the evolution of the yielding surface upon further yielding. There are two types of hardening. The first one is isotropic hardening which entails that the yielding surface continues to be centered around

its initial axis; however, its size has increased as the strain increases. The second type, called kinematic hardening, relies on the rationale that the yielding surface keeps a constant size, but it does translate in the stress space as the plastic strain is proceeding. By including the hardening features into Equation (5.35):

$$f(\{\sigma\}, \kappa, \{\alpha\}) = 0 \tag{5.36}$$

where κ is the sum of all the plastic work performed in the system upon loading, and $\{\alpha\}$ is the translation of the yield surface.

$$\kappa = \int \{\sigma\}^T [M] d \{\epsilon\}^{pl} \tag{5.37}$$

[M] refers to the mass matrix.

$$\{\alpha\} = \int C d\epsilon^{pl} \tag{5.38}$$

where C is a material parameter.

Ansys Mechanical offers several types of hardening rules for materials. The most used ones are the bilinear and multilinear isotropic hardening. In the few cases where nonlinear analysis was performed throughout this work, bilinear isotropic hardening was used. In this model, the von Mises stress is calculated as:

$$\sigma_e = \left[\frac{3}{2} \{\sigma_d\}^T [M] \{\sigma_d\} \right]^{\frac{1}{2}} \tag{5.39}$$

When the equivalent stress is equal to the current yield stress σ_k, the material goes through yielding, and the von Mises yielding criteria from Equation (5.20) is expressed as:

$$\left[\frac{3}{2} \{\sigma_d\}^T [M] \{\sigma_d\} \right]^{\frac{1}{2}} - \sigma_k = 0 \tag{5.40}$$

where σ_k is the current yield stress, and it can be determined from the equivalent plastic strain and the stress-strain curve, shown in Figure 5.4.

Implementation in Ansys Mechanical

The implementation of material nonlinearities in Ansys Mechanical is done by a backward Euler scheme[3] to ensure a consistency condition that the equivalent stress is equal to the material yield stress. Therefore, first, yield stress for a material is determined in terms of temperature. Then,

---

[3]A backward Euler scheme is a numerical method used for the time integration of differential equations. It approximates the solution at the next time step using information from the current time step.
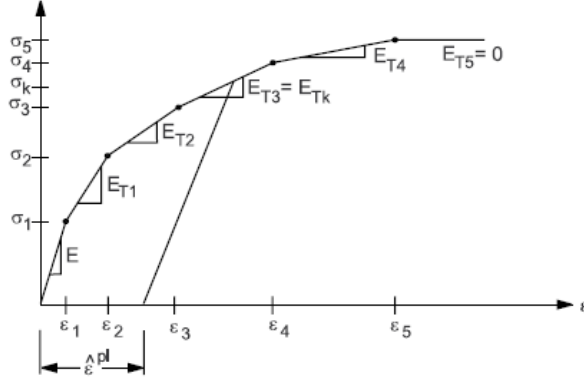
Figure 5.4: *The uniaxial behavior of the stress-strain curve is also used to determine the yield stress at the current step σ_k. Source: [56].*

the trial strain, which is defined as the difference between the total strain and the plastic strain from the previous time step, is defined, and the trial stress is calculated based on it. Furthermore, the failure condition is applied after the equivalent stress σ_e is calculated at this stress level using Equation (5.39). No plastic strain increment is needed if $\sigma_e < \sigma_y$. If $\sigma_e < \sigma_y$, the plastic multiplier λ is calculated by using a Newton-Raphson procedure [59]. The incremental plastic strain is calculated as:

$$d\{\epsilon\}^{pl} = \lambda \frac{\partial\{Q\}}{\partial\{\sigma\}} \tag{5.41}$$

The plastic strain is then updated by adding the incremental plastic strain to the plastic strain calculated at the current step.

$$\{\epsilon\}_n^{pl} = \{\epsilon\}_{n-1}^{pl} + \Delta\{\epsilon\}^{pl} \tag{5.42}$$

The elastic strain is then calculated as:

$$\{\epsilon\}^{el} = \{\epsilon\}^{tr} - \Delta\{\epsilon\}^{pl} \tag{5.43}$$

The stress vector is then:

$$\{\sigma\} = [D]\{\epsilon\}^{el} \tag{5.44}$$

The incremental plastic work, which is the sum of the plastic work performed over the whole loading, and the center of the yielding surface are calculated using Equations (5.37), (5.38) and the values are updated taking into account the previous step. Values such as equivalent plastic strain, strain increment, equivalent stress, and stress ratio are also output.

CHAPTER 6

Finite Element Formulation

The structural analysis of many systems is based on the Finite Element Method (FEM). FEM, as mentioned briefly in Chapter 4.1, is a discretization method. The Finite Element Analysis was introduced in 1956 by Turner and his team [60]. FEM divides the domain into numerous elements, thus transforming the problem into a finite number of unknown variables expressed in terms of assumed approximating functions within the element. The nodal approximation (predecessor of finite elements) is a mathematical approach that takes care of modeling a physical system with a certain number of variables or functions $u_{ex}(x)$. The function can be a representation of any variable, such as temperature, velocity. These variables can be approximated by functions $u(x)$ in a way that the difference $u(x) - u_{ex}(x)$ is small enough for a specific problem. However, constructing $u(x)$ functions becomes challenging when the number of nodes is large. That is when finite elements come to play. If there is a domain V with a complex shape, there is a function $u(x)$ that satisfies the boundary conditions of V. It implies that a number of subdomains V^e is established that represents the total domain V. Then, an approximating function is built for each element, and it depends on the nodal variables of the nodes in the current element and its boundary. Furthermore, the approximating functions are continuous over the element and the different elements. In the finite element method, the $u(x)$ functions are called nodal points and $u_{ex}(x)$ nodal variables. A clearer definition is shown in Figure 6.1 in 1D (a) and 2D (b). The nodes are denoted with numbers 1, 2, 3 and 4; the nodal coordinates are x_1, x_2, x_3 and x_4. The domain is V, and the elements are defined as V^1, V^2 and V^3. The approximating functions $u^1(x)$, $u^2(x)$ and $u^3(x)$ are linear in this case [55].

A typical FEM analysis consists of six steps. The first step is to define the problem, including its boundary conditions and loads. Then, the discretization of the geometry into elements takes place. Furthermore, the element stiffness matrix is defined. For this, the shape functions used to describe the variation of a variable within an element are taken into account. Next, a global stiffness matrix is defined in which the connection between the elements is taken into account. The global stiffness matrix can be used together with the loads and boundary conditions to solve
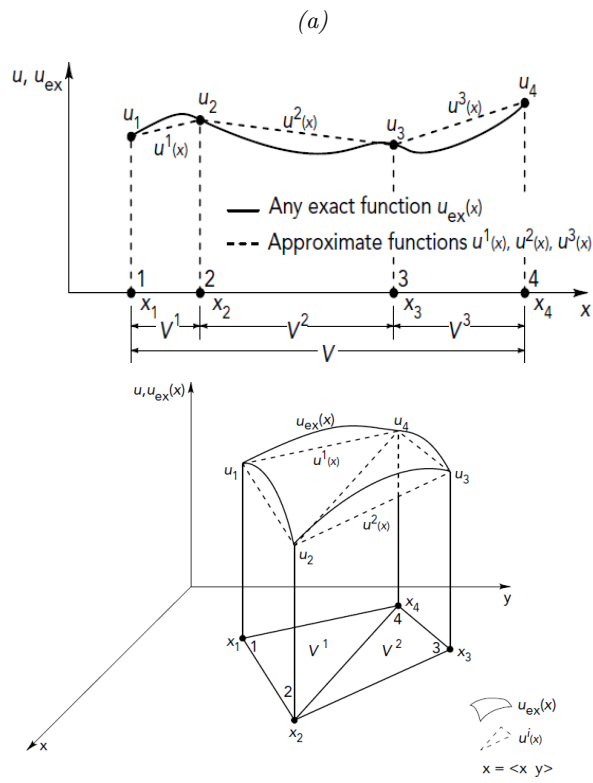
Figure 6.1: *Definition of nodes, nodal coordinates, domain and elements in 1D (a) and 2D (b). Source: [55].*

for displacement in the structure. Finally, as a last step, the results can be post-processed or used for further validation.
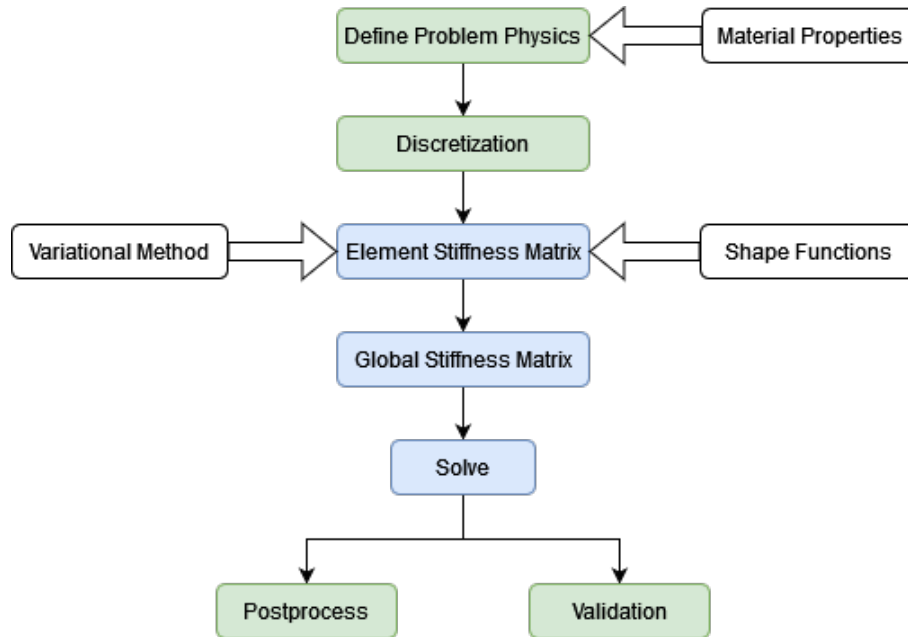
Figure 6.2: *The steps of finite element analysis. The green tabs are an indication of user operations, while the blue tabs represent the work done by the software.*

6.1   Stiffness Matrix and Thermal Conductivity Matrix

Equation (5.1) is the fundamental equation to be solved. Therefore, the stiffness matrix [K] solution must be found first. [K] is a square matrix the dimensions of which correspond to the number of nodes. For a structure with numerous elements, [K] stores all of them at each node of each element. The situation is analogous to thermal analysis, where the thermal conductivity matrix has to be calculated.

Three basic paths exist to derive the stiffness matrices and construct an approximate solution. First, there is the direct approach which derives the stiffness matrix directly from an equilibrium equation for the behavior of a given element. A differential equation usually governs the behavior of an element, and solving these equations encloses the strong form. Due to the complexity of these differential equations for different elements, the direct method is mainly used for simple elements or explaining how FEA works.

The second and third approaches constitute the weak form since they depict a problem in integral form utilizing approximate solutions that are easier to solve. The second approach consists of weighted residuals such as the Galerkin, Ritz, or the least squares formulation [61]. The Galerkin method, for instance, approximates the function satisfying the differential equation as the sum of several functions with unknown coefficients. This approximation is then substituted in the differential equation and an error equation or the residual is obtained. The unknown coefficient that minimizes the residuals can then be calculated.

The third approach is the minimum potential energy approach. It is based on variational calculus

and the calculation of the extremities of the potential energy. This approach states that the displacement that is able to fulfill the equilibrium condition must be the one for which the total potential energy reaches a minimum. The potential energy is the sum between the strain energy and the energy originating from external loads[1]. This approach is called virtual strain energy and is a special case of the virtual work principle [62]. The concept of virtual work does not have a significant physical background; instead, it is a purely mathematical approach, the goal of which is to find approximate displacement functions and provide a set of linear equations that can be solved.

6.1.1   The principle of virtual work

For a solid 3D body, the conservation of momentum is expressed by Cauchy's momentum equation in a continuum, which is in the core Newton's second law and it can be written as:

$$\rho \{\ddot{u}\} - \nabla \{\sigma\} + \{b\} = 0 \tag{6.1}$$

where $\{\ddot{u}\}$, $\{\sigma\}$ and $\{b\}$ refer to the acceleration, stress tensor and the total body forces, respectively.

Loads and constraints are applied to the equilibrium equation:

$$\{u\} = \{\overline{u}\} \quad \textbf{Constaint} \tag{6.2}$$

$$\{\sigma\} \{n\} = \{\overline{t}\} \quad \textbf{Load} \tag{6.3}$$

The $\{\overline{u}\}$ is a prescribed displacement and $\{\overline{t}\}$ the prescribed surface traction. $\{n\}$ refers to the normal to the surface.

For a virtual displacement $\{\delta u\}$:

$$\int_V \{\delta u\} \left(\rho \{\ddot{u}\} - \nabla \{\sigma\} + \{b\} \, dV\right) = 0 \tag{6.4}$$

By inserting the load and constraint equations, the virtual work equation takes the form:

$$\int_V \{\delta u\} \rho \{\ddot{u}\} \, dV + \int_V \{\delta\epsilon\} \{\sigma\} \, dV = \int_V \{\delta u\} \{b\} \, dV + \int_{S_t} \{\delta u\} \{\overline{t}\} \, dS_t \tag{6.5}$$

S_t is the surface where the external loads such as traction, is specified.

---

[1]In other words, the external work is stored in a material as strain energy.

6.1.2 Virtual Displacement Principle in Ansys Mechanical

Most of Ansys FEM formulations are based on the principle of virtual displacement [56], which states that a minimal (virtual) change in internal work or strain energy must correspond to an identical change in external work:

$$\delta U_i = \delta V_e \tag{6.6}$$

where U_i is the internal work, V_e is the external work and δ is the virtual operator.

Assuming a linear material and geometry, the virtual strain energy (internal energy) can be calculated as:

$$\delta U_1 = \int_{vol} \left(\{\delta\epsilon\}^T [D] \{\epsilon\} - \{\delta\epsilon\}^T [D] \left\{\epsilon^{th}\right\} \right) \, \mathrm{d}(vol) \tag{6.7}$$

Furthermore:

$$\{\epsilon\} = [B] \{u\} \tag{6.8}$$

expresses the connection between strain and displacement by means of the strain-displacement matrix $[B]$.

Incorporating the strain-displacement relation in Equation (6.7) and pointing out that the displacement vector $\{u\}$ does not change over the volume:

$$\delta U_1 = \{\delta u\}^T \int_{vol} [B]^T [D][B] \, \mathrm{d}(vol) \{u\} - \{\delta u\}^T \int_{vol} [B]^T [D] \left\{\epsilon^{th}\right\} \, \mathrm{d}(vol) \tag{6.9}$$

The external work done on a body is constituted by the work done due to the body force δV_1, work done due to the traction force δV_2 and work done due to the force applied to the body δV_3.

V_1 is defined as:

$$\delta V_1 = - \{\delta u\}^T \rho \int_{vol} [N]^T [N] \frac{\delta^2}{\delta t^2} \{u\} \, \mathrm{d}(vol) \tag{6.10}$$

where [N] is the shape function matrix.

V_2 is defined as:

$$\delta V_2 = \int_{area_p} \{\delta w_n\}^T \{P\} \, \mathrm{d}(area_p) \tag{6.11}$$

where $\{P\}$ is the pressure vector acting on $area_p$, and $\{w_n\}$ is a vector describing the motion normal to the surface.

V_3 is defined as:

$$\delta V_3 = \{\delta u\}^T \left\{ F_e^{nd} \right\} \tag{6.12}$$

Summing up the contributions to the external work and applying Equation (6.6) the virtual work principle is expressed as:

$$\{\delta u\}^T \int_{vol} [B]^T [D][B] \{u\} \, \mathrm{d}(vol) - \{\delta u\}^T \int_{vol} [B]^T [D] \left\{ \epsilon^{th} \right\} \, \mathrm{d}(vol) +$$
$$= -\{\delta u\}^T \rho \int_{vol} [N_n]^T [N_n] \frac{\delta^2}{\delta t^2} \{u\} \, \mathrm{d}(vol) + \tag{6.13}$$
$$\{\delta u\}^T \int_{area_p} [N_n]^T \{P\} \, \mathrm{d}(area_p) + \{\delta u\}^T \left\{ F_e^{nd} \right\}$$

Since $\{\delta u\}^T$ is an arbitrary displacement vector in all the terms, Equation (6.13) can be reduced to:

$$[K_e] \{u\} - \left\{ F_e^{th} \right\} = [M_e] \{\ddot{u}\} + \{F_e^{pr}\} + \left\{ F_e^{nd} \right\} \tag{6.14}$$

where:

$$[K_e] = \int_{vol} [B]^T [D][B] \, \mathrm{d}(vol) = \text{element stiffness matrix} \tag{6.15}$$

$$\left\{ F_e^{th} \right\} = \int_{vol} [B]^T [D] \left\{ \epsilon^{th} \right\} \, \mathrm{d}(vol) = \text{element thermal load vector} \tag{6.16}$$

$$[M_e] = \rho \int_{vol} [N_n]^T [N_n] \, \mathrm{d}(vol) = \text{element mass matrix} \tag{6.17}$$

$$\{\ddot{u}\} = \frac{\delta^2}{\delta t^2} \{u\} = \text{acceleration vector (accounts for gravity effects)} \tag{6.18}$$

$$\{F_e^{pr}\} = \int_{area_p} [N_n]^T \{P\} \, \mathrm{d}(area_p) = \text{element pressure vector} \tag{6.19}$$

Equation (6.14) represents the equilibrium state for one element. In order to express the whole domain or structure, it has to be integrated over the domain volume. Equation (6.14) can be redistributed and express Hooke's law in a set of linear equations. It is important to note that even though a thermal load vector is present in Equation (6.14), the system does not contain thermal degrees of freedom, only structural. A coupled solver is needed if there is a need to solve for temperature in addition to displacement, and this is explained further in the thesis.

Once Equation 6.14 is obtained, the software can solve for the displacement field. Then, other field variables such as strain and stress can be calculated using the obtained displacements.

6.1.3 Virtual Temperature Principle in Ansys Mechanical

The virtual temperature principle is used when dealing with thermal mechanics and is analogous to the virtual displacement principle. Applying a virtual temperature $(\delta T(x, y, z, t))$ to Equation (5.21):

$$
\begin{aligned}
\int_{vol} \left(\rho c_p \delta T \left(\frac{\partial T}{\partial t} \right) + \{L\}^T (\delta T) ([D] \{L\} T) \right) d(vol) = \\
\int_{S_2} q d(S_2) + \int_{S_3} \delta \text{ T h } (\text{T}_b - T_s) d(S_3) + \int_{vol} \delta \text{ T } \ddot{q} \, d(vol)
\end{aligned}
\tag{6.20}
$$

where *vol* represents the volume element. In the case of thermal analysis, the $[D]$ matrix represents thermal conductivity.

Since the temperature can be varied in space and time, the variables can be separated as:

$$
T = \{N\}^T \{T_e\}
\tag{6.21}
$$

$\{N\}$ represents the shape functions depending on position, while $\{T_e\}$ is the nodal temperature vector of an element and it is time dependent. Therefore the time derivatives are written as:

$$
\dot{T} = \frac{\partial T}{\partial t} = \{N\}^T \left\{ \dot{T}_e \right\}
\tag{6.22}
$$

The virtual temperature takes the form:

$$
\delta T = \{\delta T_e\}^T \{N\}
\tag{6.23}
$$

Additionally, the term $\{L\} T$ can be expressed as:

$$
\{L\} T = [B] \{T_e\}
\tag{6.24}
$$

where

$$
[B] = \{L\} \{N\} T
\tag{6.25}
$$

Combining the variational approach of Equation 6.20 with Equation (6.21) and taking into account that the density is assumed to stay constant within one element (while the specific heat capacity and internal heat generation can vary):

$$\rho \int_{vol} c_p \{N\} \{N\}^T \left\{\dot{T}_e\right\} \, \mathrm{d}(vol) + \rho \int_{vol} c_p \{N\} \{v\}^T [B] \{T_e\} \, \mathrm{d}(vol)$$

$$+ \int_{vol} [B]^T [D][B] \{T_e\} \, \mathrm{d}(vol) = \int_{S_2} \{N\} \, q^* d(S_2) \qquad (6.26)$$

$$+ \int_{S_3} T_B h \{N\} \, d(S_3) - \int_{S_3} h \{N\} \{N\}^T \{T_e\} \, d(S_3) + \int_{vol} \ddot{q} \{N\} \, \mathrm{d}(vol)$$

This equation can be rewritten in a simplified form:

$$[C_e^t] \left\{\dot{T}_e\right\} + \left([K_e^{tm}] + [K_e^{tb}] + [K_e^{tc}]\right) \{T_e\} = \left\{Q_e^f\right\} + \{Q_e^c\} + \{Q_e^g\} \qquad (6.27)$$

where:

$$[C_e^t] = \rho \int_{vol} c_p \{N\} \{N\}^T \, \mathrm{d}(vol) = \text{element specific heat matrix} \qquad (6.28)$$

$$[K_e^{tm}] = \rho \int_{vol} c_p \{N\} \{v\}^T [B] \, \mathrm{d}(vol) = \text{element mass transport conductivity matrix} \qquad (6.29)$$

$$[K_e^{tb}] = \int_{vol} [B]^T [D][B] \, \mathrm{d}(vol) = \text{element diffusion conductivity matrix} \qquad (6.30)$$

$$[K_e^{tc}] = \int_{S_3} h \{N\} \{N\}^T \, d(S_3) = \text{element convection surface matrix} \qquad (6.31)$$

$$\left\{Q_e^f\right\} = \int_{S_2} \{N\} \, q d(S_2) = \text{element mass flux vector} \qquad (6.32)$$

$$\{Q_e^g\} = \int_{vol} \ddot{q} \{N\} \, \mathrm{d}(vol) = \text{element heat generation load} \qquad (6.33)$$

Once Equation (6.27) is settled, it can be solved to find the temperature field.

6.2   Shape Functions

In order to be able to apply the virtual principles as mentioned in Chapter 6.1.1, functions that describe how variables change within one element are needed. These assumed functions are called shape functions and are used to interpolate the solutions from the nodes. The shape functions are usually polynomials whose derivative is a constant. In general, the expression for calculating the displacement approximation in an element can be written in an isoparametric form as:

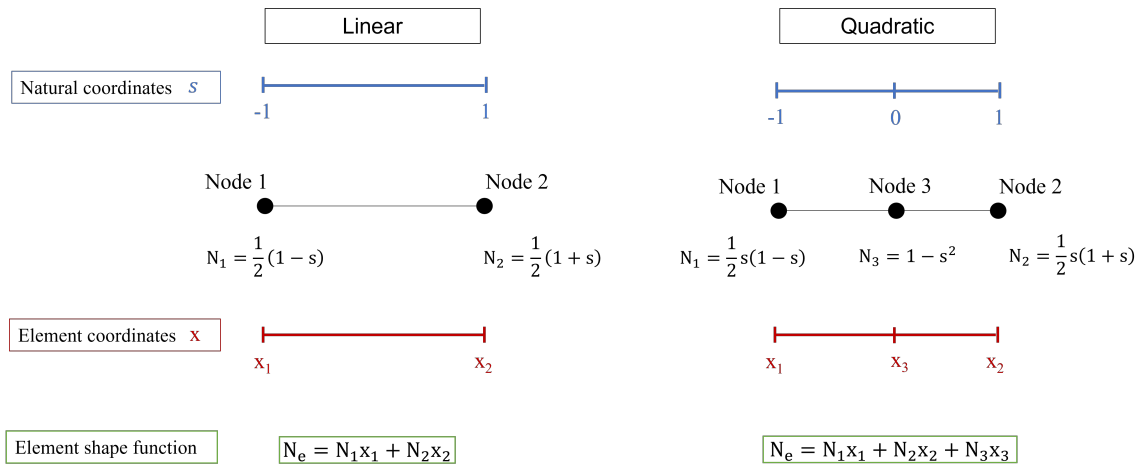$$u^e = \sum_a^n N_a(\xi) \tilde{u}_a \qquad (6.34)$$

Figure 6.3: *The difference between linear and quadratic shape functions with the corresponding nodes are shown. The shape function of the element is shown at the bottom of the figure for linear and quadratic shape functions, respectively.*

where ξ refers to the parent coordinate, which is expressed as a normalization of the global coordinates from -1 to 1. $\tilde{u}_a$ are the parameters to be determined and n is the total number of functions for one element.

There are different orders of shape functions; two of the most used ones are linear and quadratic. As the term denotes, linear shape functions use a first-order polynomial to describe the connection between the nodes in an element. A polynomial of the second order is used in the quadratic shape functions. Quadratic shape functions are, therefore more complex and require greater computational effort. In some cases, using quadratic elements is helpful due to the complex response of the structure under investigation. In this work, the linear shape functions with enhanced strain functions (see Chapter 6.3) are used. The difference between linear and quadratic shape functions is illustrated in Figure 6.3.

6.2.1 Element types in Ansys Mechanical and their shape functions

6.2.1.1 SOLID285

SOLID285 is a 4-node tetrahedral solid element shown in Figure 6.4, where I, J and K here are the nodal points [56].

The shape functions for the displacement, pressure and temperature are given with the following equations:
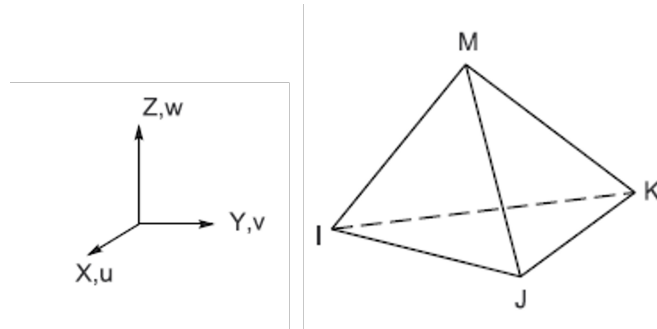
Figure 6.4: *SOLID285 element from Ansys Mechanical Theory Reference. I, J and K are the nodal points. Source [56].*
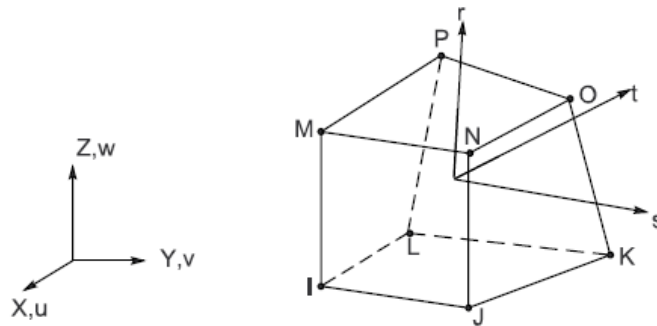

Figure 6.5: *SOLID185 element from Ansys Mechanical Theory Reference. Source [56].*

$$u = u_I L_1 + u_J L_2 + u_K L_3 + u_M L_4 \quad \text{Translation in u-direction} \tag{6.35}$$

$$v = v_I L_1 + v_J L_2 + v_K L_3 + v_M L_4 \quad \text{Translation in v-direction} \tag{6.36}$$

$$w = w_I L_1 + w_J L_2 + w_K L_3 + w_M L_4 \quad \text{Translation in u-direction} \tag{6.37}$$

$$P = P_I L_1 + P_J L_2 + P_K L_3 + P_M L_4 \quad \text{Pressure} \tag{6.38}$$

$$T = T_I L_1 + T_J L_2 + T_K L_3 + T_M L_4 \quad \text{Temperature} \tag{6.39}$$

where L denotes the location of the integration points for a tetrahedron. The integration points are further explained in Section 6.3.

6.2.1.2 SOLID185

SOLID185 is a simple 8-node hexahedron, shown in Figure 6.5, where the nodal points are written as I, J, L, K, M, N, O and P. A hexahedron's natural coordinates are denoted with r, s and t.

The shape function for the displacement in the u-direction for a SOLID185 element is written as:

$$u = \frac{1}{8} \left(u_I \left(1 - s \right) \left(1 - t \right) \left(1 - r \right) + u_J \left(1 + s \right) \left(1 - t \right) \left(1 - r \right) \right.$$
$$+ u_K \left(1 + s \right) \left(1 + t \right) \left(1 - r \right) + u_L \left(1 - s \right) \left(1 + t \right) \left(1 - r \right)$$
$$+ u_M \left(1 - s \right) \left(1 - t \right) \left(1 + r \right) + u_N \left(1 + s \right) \left(1 - t \right) \left(1 + r \right)$$
$$\left. + u_O \left(1 + s \right) \left(1 + t \right) \left(1 + r \right) + u_P \left(1 - s \right) \left(1 + t \right) \left(1 + r \right) \right) \tag{6.40}$$

The rest of the shape functions are analogously given to Equation (6.40).

6.3 Numerical Integration

Numerical integration methods are employed to construct the element matrices through integration over a reference element. A reference element has a very basic shape in a reference space with coordinates r,s and t, and it can be transformed into the "real" element by using a geometrical transformation τ. The numerical integration used by Ansys Mechanical is the Gauss Quadrature integration method [63]. The term quadrature implies that an integral is evaluated numerically and not analytically.

Gauss Quadrature method consists of three steps. First, the integral given in global coordinates (x, y, z) is transformed into the normalized or natural coordinates (r, s, t), which take values from -1 to 1. Then, the transformed functions are evaluated at specific locations within an element, and the locations are also referred to as Gauss points. Finally, weighting factors are applied to each Gauss point and the contributions are summed up. In Table 6.1, the weighting factors and the function arguments are given for 2 and 3-point integration for quadrilateral cells:

No. of points in one direction	Point locations	Weighting factors
2	$r_1 = 1$	$w_1 = 0.57735$
	$r_2 = 1$	$w_2 = -0.577335$
3	$r_1 = 0.55556$	$w_1 = -0.77460$
	$r_2 = 0.88889$	$w_2 = 0$
	$r_3 = 0.55556$	$w_3 = 0.77460$

Table 6.1: *Gauss points and weighting factors for each point of a quadrilateral cell. Source [56].*

Figure 6.6 shows a quadrilateral cell's 2x2 and 3x3 Gauss integration points.

The Gauss points and weighting factors for a tetrahedron are given in Table 6.2.

The numerical integration affects the accuracy and cost of the simulation and it has to be chosen carefully in a way that computes the element volume accurately. There are two categories of numerical integration: full and reduced. The full integration implies that the rules for displacement are in the same order as the element. In other words, the number of nodes located in an element edge is the same as the number of Gauss points. This means that the element order is able to
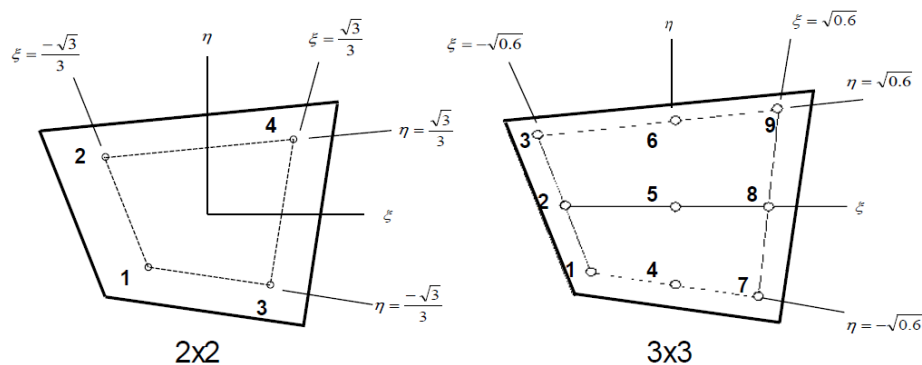
Figure 6.6: *Location of Gauss Integration points for a quadrilateral cell. Source [56].*

Points	Point locations	Weighting factors
4 (corner points)	$w_1 = 0.58541$ $w_2 = w_3 = w_4 = 0.13819$	0.25

Table 6.2: *Gauss points and weighting factors for a tetrahedron cell. Source [56].*

provide the exact integral of the components of the strain energy. Fully integrated lower-order elements (linear) can exhibit shear locking in bending problems by creating artificial shear strains which do not physically exist. This issue becomes particularly large in structures with a large length-to-thickness ratio. Therefore, usually an enhanced strain formulation [64] [65] is applied, adding additional shape functions to treat volumetric locking.

In the reduced integration, on the other hand, the number of Gauss points is one order lower than the number of nodes located in the element edge. The elements during reduced integration can avoid locking and are also preferred for better computational utilization times, which is beneficial.

For lower-order elements, the full integration with enhanced strain formulation is the default in Workbench[2], while for higher-order elements, the default is the reduced integration [56]. In Ansys Mechanical, element stress and strains are calculated at Gauss points, while displacement is calculated at nodes. Furthermore, the stresses and strains at nodes can be calculated by extrapolating the Gauss point values, which depends on the element type and integration scheme.

6.4   Solvers

There are two generally available solvers in Ansys Mechanical, a direct and an iterative solver. The direct solvers use a direct elimination process based on Gauss elimination, which essentially decomposes the matrix [K] into lower and upper triangular matrices [K]=[L] [U]. Furthermore,

---

[2]Workbench is part of the Ansys Suite of products. It is used for setting up couplings or as a work frame for different types of simulations. All the Ansys software are included in Workbench.

substitutions concerning [L] and [U] matrices are made, and the displacement vector $\{u\}$ is calculated. The main type of direct solver is the Direct Sparse Solver, which is also the solver used in the calculations throughout this work.

On the other hand, the iterative solvers start with an initial guess $\{u_1\}$ for the solution. Then, the solver iterates until a convergence criterion is reached. The calculation of $\{u_{n+1}\}$ involves [K], $\{F\}$ and $\{u\}$ from the previous iterations. The direct solver is explained here based on Ansys documentation [56].

The equation system with the lower and upper triangular matrices is solved:

$$[L][U]\{u\} = \{F\} \tag{6.41}$$

Assuming that $\{w\}$ is a vector containing [U] and $\{u\}$, the matrix equation system in Equation (6.41) is then:

$$\{w\} = [U]\{u\} \implies [L]\{w\} = \{F\} \tag{6.42}$$

$\{u\}$ can be obtained back-substituting into the triangular matrix. When [K] is symmetric, its decomposition into lower and upper matrices is done as shown in Equation (6.41). If [K] is non-symmetric:

$$[K] = [L][D][L]^T \tag{6.43}$$

where [D] is a diagonal matrix whose terms can be negative in some cases of non-linear analysis. Therefore the above equations are written as:

$$[L][D][L]^T\{u\} = \{F\} \tag{6.44}$$

$$\{w\} = [D][L]^T\{u\} \tag{6.45}$$

$$[L]\{w\} = \{F\} \tag{6.46}$$

and then back substituting:

$$[D][L]^T\{u\} = \{F\} \tag{6.47}$$

The [K] matrix is sparsely populated with non-zero values in non-diagonal positions; therefore, the direct sparse solver deals exclusively with the non-zero values in [K]. Furthermore, it can happen that during the decomposition of [K] into upper and lower triangular matrices, non-zero coefficients show up in the [L] or [L'] at the positions where zero coefficients were before in [K].

Therefore, the direct solver takes care of this by reordering the equation numbers in [K] by a permutation of rows and columns of [K] with the rows in $\{F\}$ in an appropriate manner. This means that the fill of [L] matrices are kept to a minimum, which adds up to the performance of the Direct Sparse Solver. To achieve this, different reordering algorithms are available [66].

CHAPTER 7

Fluid-Structure Interaction

Fluid Structure Interaction (FSI) is a type of analysis where the interaction between two or more different physics phenomena is analyzed. In the context of this work, Fluid-Structure Interaction (FSI) means assessing the mechanical and thermal hydraulic behavior of the fuel plates as well as the influence one of the fields has on the other. As an example, the water running through the reactor core can induce vibrations and deformations of the plate, which in turn can change the velocity and pressure of the water, and thus, also the temperature and heat fluxes of the fuel plate. Furthermore, the thermal expansion of the fuel plate under thermal loads impacts the width of the cooling channel, leading to a modification of the velocity and pressure fields. Since the thermal aspect is included into the calculations, the term is updated from FSI to Thermal-Fluid-Structure Interaction (TFSI). In this case, TFSI does not present a severe change of analysis type, it only means that the thermal response of the system being analyzed is taken into account in addition to the structural and hydraulic responses.

There are two main branches of FSI: one-way and two-way coupling. one-way coupling is a sequential analysis, meaning that a converged solution is first achieved for one solver, and the results are transferred as boundary conditions to the second field, which then is iterated towards a converged result. The two-way coupling on the other hand is referred to as a bidirectional or direct coupling, and it includes several sub-methods listed from strongest to weakest coupling [67]:

- Fully coupled. In this type of coupling, the fluid and solid fields are included in one monolithic fluid-structure matrix, which is difficult to solve. Such modeling is up to this point not possible for the Ansys Mechanical - Ansys CFX coupling.

- Two-way iteratively implicit coupling relies on the fluid and structural equations being solved separately. The data such as temperature, pressure etc is then transferred between the solvers. The solvers continue iterating within each time step to find an implicit solution.

- Two-way explicit coupling concept is similar to the iteratively implicit coupling with the

exception that the fluid and structural solvers exchange information on a single time step.

All types of coupling are shown in Figure 7.1 in terms of different physics phenomena. In this thesis, the one-way coupling and the two-way iterative implicit coupling are used. In this sense, the implicit/explicit concept is not related to the solver per se, but to the formulation used in the matrices. For instance, implicit coupling refers to the fact that the solution between fluid and solid is done within one time step, while explicit means that the solid and fluid fields are solved separately and there are n coupling iterations within time steps.

The coupling workflow between the one-way and two-way coupling differs greatly. In the one-way coupling, the thermal and hydraulics fields are considered within the fluid solver and it means that the fluid solver Ansys CFX is used as a conjugate heat transfer solver. Therefore, it solves for thermal-hydraulics and heat diffusion in solids. In the two-way coupling the thermal-structural coupling is used, which implies that the thermal diffusion in solids as well as deformation are accounted for in the structural solver Ansys Mechanical. The thermal-hydraulic behavior of the fluid is calculated with Ansys CFX. Furthermore, Ansys CFX and Mechanical exchange information on a step basis. The thermal-structural coupling is described in further detail in Section 7.1.
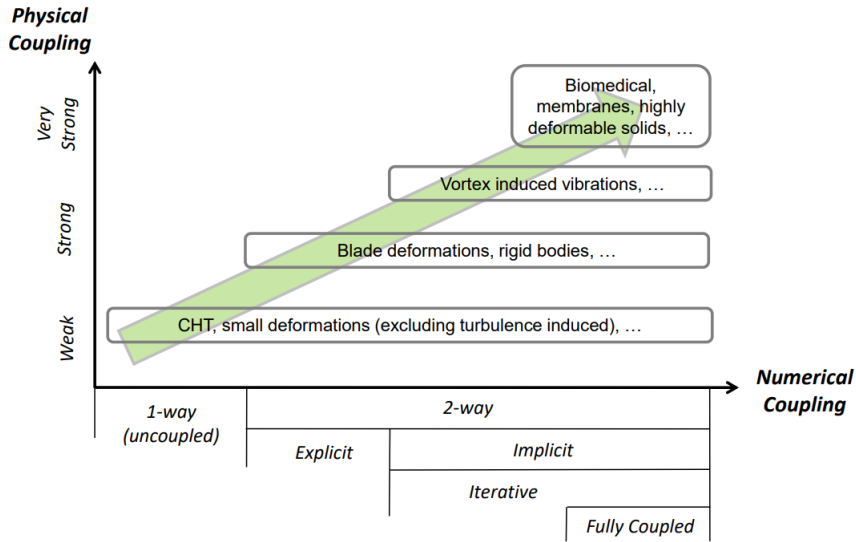
Figure 7.1: *Examples of physics phenomena in terms of their physics complexity (y axis) and numerical coupling (x axis). Conjugated Heat Transfer (CHT) does not present big challenges. Therefore, a basic coupling approach such as one-way coupling can be used. For more complex physical phenomena such as biomedical membranes (which are very prone to deformation and vibrations) would require a very strong coupling such as the fully coupled approach. The graph is provided by Ansys. Source: [67].*

7.1 Thermal-Structural Coupling

Analogously to FSI, the thermal-structural coupling can be done in a sequential manner or a direct one. A sequential manner means that the thermal field is solved first, and the results are imported into the structural solver as boundary conditions. This method can be used for example to calculate the thermal expansion of railways due to the sun. Another approach for the sequential coupling is to invert the order of solving the physics, such that the displacement field is solved first, then the results are used as boundary condition for the thermal field. For example, if the heat generated in the disc brakes of a car should be assessed, this type of coupling would be used.

The direct approach implies that both fields are solved simultaneously exchanging information with one-another. The direct thermal-structural coupling aims of capturing the thermally-induced deformation within the scope of one element. This means that the finite element types used in this analysis have both displacement and temperature degrees of freedom. A general example of the direct thermal-structural coupling would be the physics of a high temperature turbine where the thermal expansion impacts the deflection and vice-versa. Figure 7.2 shows the different thermal-structural coupling types together with examples.

To show the solution of a thermal-structural system, the equations representing the respective fields are shown from Chapter 6.1.2 and Chapter 6.1.3. The structural solution has the form:

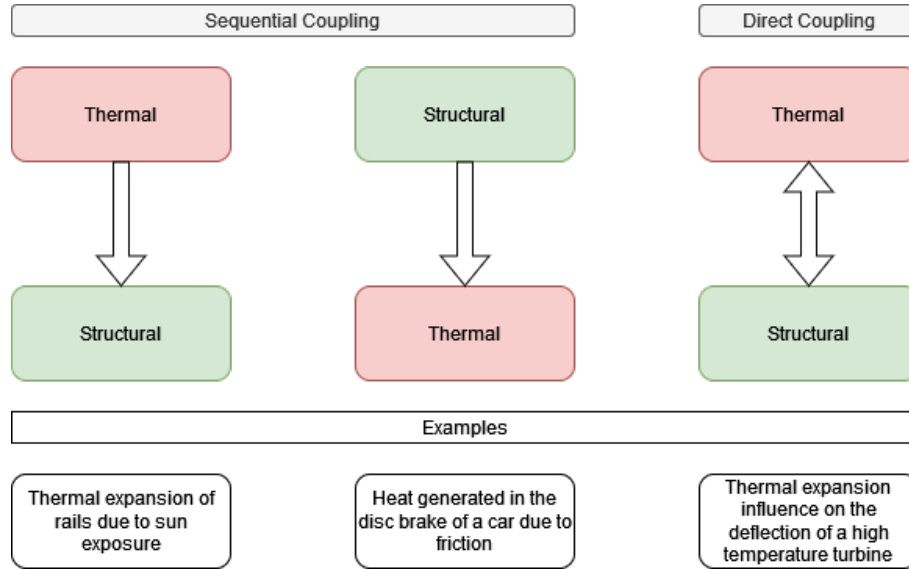$$[M]\{\ddot{u}\} + [C]\{\dot{u}\} + [K]\{u\} = \{F\} \tag{7.1}$$

Figure 7.2: *Different types of thermal-structural coupling including examples. Refurbished from [68].*

where $\{\ddot{u}\}$ and $\{\dot{u}\}$ are the acceleration and velocity, respectively in the case a moving structure is used, [M] is the mass matrix, [C] is the structural damping matrix, [K] is the stiffness matrix, $\{u\}$ is the displacement vector and $\{F\}$ is the applied load [56].

The thermal solution has the form:

$$[C^t]\left\{\dot{T}\right\} + [K^t]\{T\} = \{Q\} \tag{7.2}$$

where $[C^t]$ is the specific heat matrix, $\left\{\dot{T}\right\}$ is the temperature gradient vector, $\{T\}$ is the temperature vector, $[K^t]$ is the thermal conductivity matrix and $\{Q\}$ is the thermal load vector. The definitions of these matrices are given in Chapter 6.1.3.

Ansys provides 2 types of thermal-structural coupling: weak and strong. The weak coupling implies that the thermal matrices are simply added to the structural ones. The matrix equation has the form:

$$\begin{bmatrix} [M] & [0] \\ [0] & [0] \end{bmatrix} \begin{Bmatrix} \ddot{u} \\ \ddot{T} \end{Bmatrix} + \begin{bmatrix} [C] & [0] \\ [0] & [C^t] \end{bmatrix} \begin{Bmatrix} \dot{u} \\ \dot{T} \end{Bmatrix} + \begin{bmatrix} [K] & [0] \\ [0] & [K^t] \end{bmatrix} \begin{Bmatrix} u \\ T \end{Bmatrix} = \begin{matrix} \{F\} + \left\{F^{th}\right\} \\ \{Q\} + \left\{Q^{ted}\right\} \end{matrix} \tag{7.3}$$

All the matrices on the left-hand side of Equation (7.3) contain coefficients that are based on material properties such as Young's modulus, Poisson's ratio, thermal conductivity, specific heat capacity etc. On the right-hand side, there is the sum of the nodal forces and pressure vector $\{F\}$, the sum of the heat generation load and convection surface heat flow vectors $\{Q\}$, the thermal load vector $\left\{F^{th}\right\}$, the heat generation rate vector for thermoelastic damping $\left\{Q^{ted}\right\}$. All the vectors on the right hand side of the equation are loads and are, therefore, user defined. The temperature and displacement vectors are the unknowns for which these equations are solved.

For the strong coupling the matrix equation is written as:

$$\begin{bmatrix} [M] & [0] \\ [0] & [0] \end{bmatrix} \begin{Bmatrix} \ddot{u} \\ \ddot{T} \end{Bmatrix} + \begin{bmatrix} [C] & [0] \\ [C^{tu}] & [C^{t}] \end{bmatrix} \begin{Bmatrix} \dot{u} \\ \dot{T} \end{Bmatrix} + \begin{bmatrix} [K] & [K^{ut}] \\ [0] & [K^{t}] \end{bmatrix} \begin{Bmatrix} u \\ T \end{Bmatrix} = \begin{Bmatrix} F \\ Q \end{Bmatrix} \tag{7.4}$$

where $[K^{ut}]$ is the thermoelastic stiffness matrix, and $[C^{tu}]$ is the thermoelastic damping matrix [56].

CHAPTER 8

Impulse Excitation Technique (IET)

To calculate the as fabricated Forschungs-Neutronenquelle Heinz Maier-Leibnitz (FRM II) fuel plate behavior under different loads, the mechanical material properties of the fuel are required. To the knowledge of the author, there are no elastic modulus data available on the current FRM II fuel U_3Si_2 dispersed in an aluminum matrix as fabricated by *Framatome CERCA*. As a first assessment, a rough hand calculation can be done in order to have an estimation of E-modulus and the fundamental vibration frequency of the plate, accordingly.

The U_3Si_2 fuel dispersed in an aluminum matrix can be assumed as a fiber in a matrix. By using the rule of mixtures for an isotropic mixture of materials such as a fiber and a matrix, the Voigt model [69] estimates the E-modulus for axial loading by using:

$$E_{mix} = fE_f + (1 - f)E_m \tag{8.1}$$

where f is the volume fraction of the fiber calculated as:

$$f = \frac{V_f}{V_f + V_m} \tag{8.2}$$

V_f and V_m are the volumes of the fiber and matrix, respectively.

Using Equation (8.1) for the FRM II plate and applying the properties of U_3Si_2 [70] and aluminum A6061-0 [71], the expected Young's modulus is on the range from 69 GPa to 79 GPa. Applying this range of E-modulus and the appropriate plate dimensions in the equations provided in [72], the longitudinal frequency of the plate ranges from 3057 Hz to 3272 Hz.

For a more precise assessment, E-modulus of FRM II plates containing the fuel, cladding and frame were measured at the fuel fabricator *Framatome CERCA* by using the Impulse Excitation Technique (IET). Impulse Excitation Technique (IET) is a non-destructive method, and it follows a simple approach. A mechanical impulse is generated in the sample by means of a light touch with

a small hammer. The generated elastic waves dampen depending on the material properties and composition of the sample. The resulting elastic waves are picked up by a sensitive microphone or a piezoelectric detector and then transformed into spectral data by using the Fast Fourier Transform (FFT) technique. After the natural frequencies of the sample are established, they are used as input values into engineering correlations and the Young's modulus can thus be obtained.
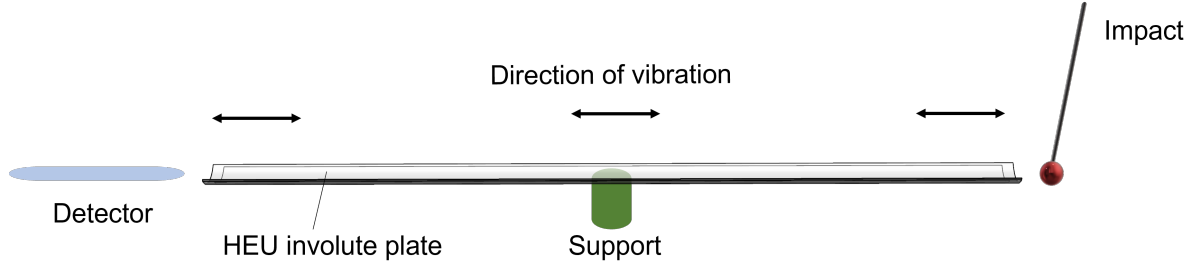

Figure 8.1: *The schematics of the experimental setup is shown.*

For plate samples with a large length-to-thickness ratio, the bending and torsional fundamental frequencies are small and thus, complicated to capture when noise is present in the experimental room. Therefore, in the performed measurements, the longitudinal vibrations were measured due to their large amplitude and ease of accessibility. The longitudinal fundamental frequency can be related to E-modulus by the following formula [72]:

$$E = \frac{f_{long}^2}{k^2} \cdot \frac{m \cdot l}{A} \cdot 4 \cdot C \tag{8.3}$$

where f_{long} is the longitudinal frequency, k is the harmonic order, m is the mass, l is the length of the specimen, A is the cross section area and C is a factor used to account for the small cross section to length ratio of the sample. C is defined as:

$$C = 1 + \frac{k^2 \pi^2 \nu^2 I}{A l^2} \tag{8.4}$$

where ν is the Poisson ratio and I is the moment of inertia, which for a rectangular cross section, is defined as:

$$I = \frac{b h^3}{12} \tag{8.5}$$

where b is the width and h the height of the rectangular cross section. The Poisson ratio ν can be calculated by using the E- and shear- moduli such as:

$$\nu = \frac{E}{2G} - 1 \tag{8.6}$$

where G refers to the shear modulus, and it can be calculated by measuring the torsional frequency of the sample under investigation. Since the fundamental torsional and bending frequencies of the FRM II plate are expected to be very low[1] and thus challenging to measure, the Poisson ratio was taken as a stable value of 0.3 in the above formulas. The Poisson ratio of aluminum is 0.33. Since the plate contains a small amount of U_3Si_2 in addition to aluminum, its Poisson ratio is expected to be somewhat smaller than 0.3. Additionally, it was proven that the variation of Poisson ratio in Equation (8.3) yields a change of roughly $10^{-6}\%$ in Young's modulus, which is negligible.

A schematic of the experimental setup used to measure the E-modulus is shown in Figure 8.1.

In addition to the FRM II fuel plates, a plate made of pure AlFeNi with the same dimensions as the ones in the reactor was measured, with the rationale being that the FRM II plates are made mostly of AlFeNi, and therefore the Young's modulus of the fuel plate and AlFeNi plates are believed to be rather similar. The results concerning the fuel plate and AlFeNi plate are shown in the Material Properties Section in Chapter 10.3.

---

[1]Roughly 15 Hz

Part III

Explanation of Codes and Coupling Approaches

CHAPTER 9

Neutronics - Hydraulics Coupling

The coupling between Serpent 2 and Ansys CFX (CFX) is a joint effort between the author and Dr. Christian Reiter who provided the Serpent 2 results [2, 10]. Since Serpent 2 modeling is not the main focus of this thesis, only very few and absolutely necessary details are provided. More details regarding the Serpent 2 calculations can be found on previous work [2, 3, 10, 11] of TUM CNSI [73]. On the other hand, details regarding the CFX modeling are given in the next sections.

9.1 Thermal Hydraulics

The neutronics-thermal hydraulics work frame consists of two key points:

1. Serpent 2-CFX coupling is validated for the Forschungs-Neutronenquelle Heinz Maier-Leibnitz (FRM II) Highly-Enriched Uranium (HEU) case by using the previously performed MCNP-CFX coupling as a validation source [12] and the licensing report of FRM II prepared by *Siemens* in 1996 [5].

2. An adequate mesh and model representing the physics of the system are established.

3. The results obtained with Serpent 2-CFX coupling are verified by using the coupling of a 2D thermal-hydraulic code PLTEMP with Serpent 2, previously developed as part of a master thesis [74]. An additional independent verification is performed by Argonne National Laboratory (Argonne) with the coupling of MNCP and their in-house code CD3CL2 [3].

Once the steps mentioned above are completed, the approach is used to predict the thermal-hydraulic and neutronic behavior of a potential LEU design for FRM II.
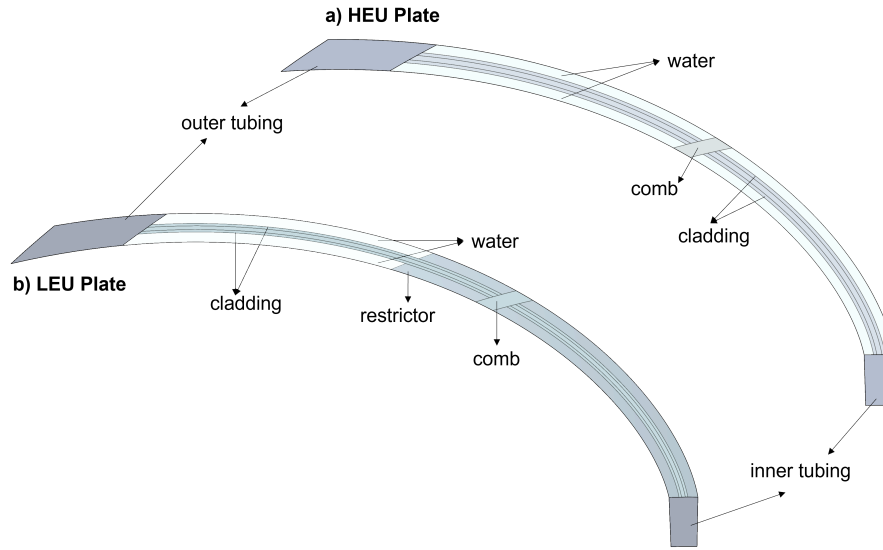
Figure 9.1: *Schematics of the CAD model of a single HEU (a) and LEU (b) plate with a split cooling channel.*

9.1.1 Geometry

The computer-aided design (CAD) models needed for the thermal-hydraulic analysis was built in *SolidWorks* [75]. Furthermore, an exact drawing of the involute is possible by using the parametric equation tools in *SolidWorks*. Due to the rotational symmetry of the core, only one fuel plate together with the directly adjacent structural materials, such as side plates and combs, are taken into account. Additionally, the cooling channel is split in half on both the concave and convex sides of the plate to fulfill the symmetry condition. This approach decreases the computational efforts. A top view of the HEU and Low Enriched Uranium (LEU) plates is shown in Figure 9.1.

The plate models are split into three parts: inlet, main, and outlet sections, also shown in Figure 9.2. For HEU plate: the inlet section is referred to as a 4 cm long zone, starting from the actual inlet until the top of the heated area. The main section comprises the 70 cm long-fueled plates. The outlet section begins at the bottom of the fueled area and is 7.6 cm. The HEU outlet was slightly extended compared to previous work [12] so that the turbulence induced by the lower comb can develop before the outlet boundary condition (see Chapter 12). This extension of the HEU outlet does not show a difference in results compared to previous work, but it does ease the convergence behavior of the simulation.

For the potential LEU plate, the inlet section is kept constant at 4 cm long, while the main part is extended to 83 cm. The outlet section for the LEU plate was even further extended to 15 cm due to the presence of the flow restrictor. As mentioned in the Introduction Chapter 1.3, the current flow restrictor used in the calculations performed in this work is a preliminary design. More details on the flow restrictor and its related boundary conditions are shown in Section 9.1.2.
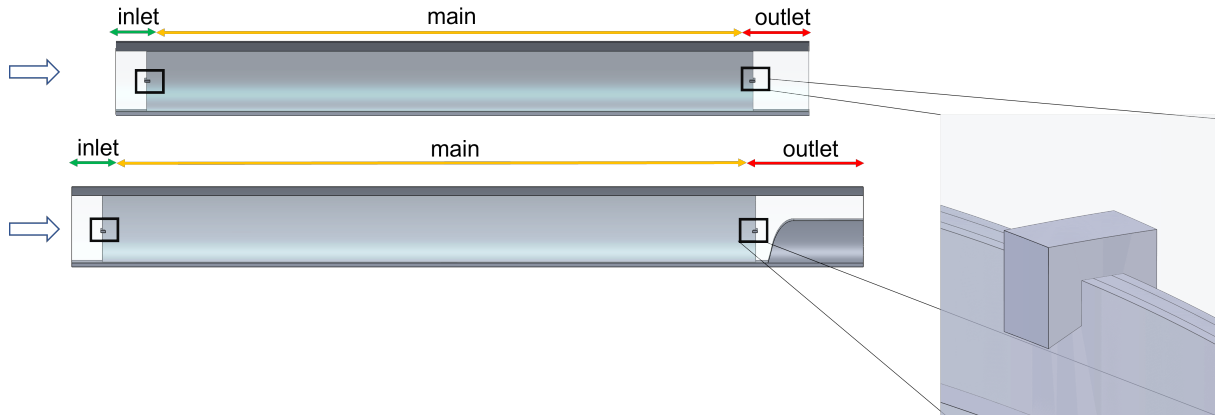
Figure 9.2: *The CAD model of both HEU and LEU plates created in SolidWorks and a zoom-in at the comb, is shown. The empty arrows refer to the water movement direction, while the red, yellow, and green arrows show the inlet, main and outlet sections used for the meshing process.*

9.1.2 Mesh

The mesh used for further calculations and couplings comes as a result of a mesh sensitivity analysis. Prior to mesh generation and evaluation, the height of the first cell at the wall was determined such that the y^+ value lies within the logarithmic region of 30-200 (see Chapter 4.2), and the usage of the automatic wall treatment is appropriate. Using Equation (4.1), the height of the first cell at the wall can be calculated to be around 0.06 mm to 0.09 mm depending on the mainstream velocity which ranges from $9.8\,\mathrm{m\,s^{-1}}$ at the inlet to roughly $21\,\mathrm{m\,s^{-1}}$ close to the lower comb.

Main section

The main section is meshed with hexahedra elements, which allow for a high degree of user control. Since this is the area where the heat is deposited and, therefore, where most of the heat transfer takes place, special care is taken to find a suitable mesh that captures the physics correctly. For this, the necessary number of elements along the plate's thickness, width, and length is explored. For the HEU plate, 34 elements are placed in the thickness of the water domain (17 on each side), 8 in each cladding domain, and 10 in the fuel. Additionally, in the radial direction, 25 cells are used to mesh each frame in the radial direction, 120 cells and 75 cells for the higher and lower density fuels, respectively. 200 cells are placed in the longitudinal direction.

For the LEU plate, the final main section mesh has 66 elements through the thickness, of which 40 are placed in the cooling channel (20 on each side), 8 in each cladding domain, and 10 in the fuel. Furthermore, 230 elements are placed along the width of the cooling channel, 25 in the frame, 180 in the fuel, and 15 in the tubing. The final mesh used for calculations of the HEU plate consists of approximately $3 \cdot 10^6$ nodes, while the mesh used for the LEU calculation has about $4.3 \cdot 10^6$ elements. Table 9.1 summarizes all the meshing parameters for both HEU and

Plates	Thickness				Width		Length
	Water	Cladding	Fuel	Frame	Fuel 3.0	Fuel 1.5	All
HEU plate	17	8	10	25	120	35	200
LEU plate	20	8	10	25	180		230

Table 9.1: *Meshing details for the main heated part in the HEU and LEU plate.*

LEU plates.

Inlet and Outlet sections

The inlet and outlet regions are discretized using tetrahedra cells, while the main part is meshed with hexahedra cells. This was done to avoid skewed hexahedra cells in the combs' vicinity. Due to the tilted bottom surface of the combs, the usage of skewed hexahedra cells presents numerical instability.

For the inlet and outlet section, a maximum element size of 1 mm is used, except for the cladding and frame where the element size is set to 0.5 mm. The mesh density at the water domain right below and above the comb is also increased to 0.5 mm in pursuance of the maximum and minimum pressure values using the sphere influence radius method. This implies that a sphere with a certain radius covering the chosen areas for mesh refinement is defined. The advantage of this sizing method is the ability to select specific zones and not the entire domain, edge, or surface.

In the areas where the inlet and outlet sections are connected to the main heated section, the mesh is further refined to 0.2 mm to ensure continuous development of the heat transfer processes and velocity and pressure contours. Moreover, in order to properly account for the heat transfer at the walls, 5 mesh element layers are created at the fluid-solid interface with a first cell height of 0.05 mm, and a growth factor of 1.2. At the inlet, an additional refinement takes place by setting a sphere influence radius with an element size of 0.5 mm with the aim to better capture the velocity development into the domain. The same meshing approach was followed for the inlet and outlet sections of the LEU plate.

The three meshes were then "glued" together using the General Grid Interface (GGI) feature in CFX. The GGI option ensures the connection between non-matching element types such as hexahedron to tetrahedron in this case or node location. Further details on GGI theory can be found in [35].

9.1.3 Turbulence Parameter Evaluation

The turbulence parameters at the inlet of the water domain are estimated using the formulas shown in [76]. The hydraulic diameter of a channel that consists of two concentric circles is

defined as:

$$d_h = d_0 - d_i \tag{9.1}$$

In a fully developed flow, the turbulence length scale l is estimated to be 3.8 % of the hydraulic diameter in a circular pipe and 7% of the hydraulic diameter in cases where the pipe diameter does not imply the hydraulic diameter [77]:

$$l = 0.07 \cdot d_h \tag{9.2}$$

In turbulence models such as K-ϵ, the turbulent kinetic energy is related to the turbulent length scale such that:

$$l = C_\mu^{3/4} \frac{K^{3/2}}{\epsilon} \tag{9.3}$$

where C_μ is a constant with value 0.09. Similarly, for k-ω based models:

$$l = C_\mu^{-1/4} \frac{K^{1/2}}{\omega} \tag{9.4}$$

The turbulent kinetic energy K can be calculated as:

$$K = \frac{3}{2} v'^2 \tag{9.5}$$

Where v'^2 is the mean square of the velocity fluctuations. To calculate it, Reynolds number (Re) and turbulence intensity are first taken into account:

$$Re = \frac{v d_h}{\nu} \tag{9.6}$$

And:

$$I = 0.16 \cdot Re^{-1/8} \tag{9.7}$$

The turbulence intensity can also be expressed as a ratio between the root-mean-square of the velocity fluctuations v' and Reynold's averaged velocity $\tilde{v}$:

$$I = \frac{v'}{\tilde{v}} \tag{9.8}$$

Using these relations, the turbulence parameters of the FRM II plate at the inlet are summarized in Table 9.2.

Parameter	Symbol	Value HEU	Value LEU
Hydraulic diameter (mm)	d_h	99	107.1
Reynolds number (-)	Re	$1.4 \cdot 10^6$	$1.54 \cdot 10^6$
Turbulent intensity (%)	I	2.7	3.6
Turbulent energy ($m^2\,s^{-2}$)	K	0.1	0.2
Turbulent length scale (mm)	l	6.9	7.5
Turbulent dissipation rate (s^{-1})	ω	87.8	108.3
Turbulent dissipation ($m^2\,s^{-3}$)	ϵ	0.8	1.9

Table 9.2: *The turbulence parameters at the inlet of the water domain for the current HEU plate and the potential LEU plate.*

The cooling channel thickness of the potential LEU core is larger compared to the HEU core, leading to a larger hydraulic diameter. Since Re number depends proportionally on the hydraulic diameter, it increases slightly in the LEU core. A higher Re number indicates larger turbulence in the channel. This is reflected by the higher turbulent intensity I and turbulent energy K. However, even though the turbulent intensity is larger in the LEU core, the turbulent intensity values between 1% and 5% are still in the medium turbulent intensity range. The turbulent length scale increases from 6.9 mm to 7.5 mm from HEU to LEU. This means that the largest eddies in the LEU core are slightly larger. Analogously, the rate at which the turbulent kinetic energy transforms into thermal energy is also increased for the LEU core compared to the HEU core. This implies larger turbulent heat transfer and therefore, slightly more efficient cooling in the LEU core.

9.1.4 Boundary Conditions

Inlet

HEU
The mass flow of water going through the FRM II core is $274.5\,\mathrm{kg\,s^{-1}}$. Given that there are in total 113 plates and the CFD setup consists of one of them, $2.4292\,\mathrm{kg\,s^{-1}}$ water is flowing through one plate. A preliminary calculation of the velocity profile from the sieve is performed to assure a fully developed flow at the inlet of the Computational Fluid Dynamics (CFD) domain. The details of these calculations are shown in Appendix VI. The velocity profile obtained from this calculation is used as a boundary condition for the inlet. Additionally, the inlet water temperature is set at $37\,°\mathrm{C}$, according to [5].

LEU
For the LEU core, the mass flow calculated by the flow network code in [3] results in $277.655\,\mathrm{kg\,s^{-1}}$. Since there are 109 plates in the LEU core, the mass flow crossing one coolant channel is $2.5473\,\mathrm{kg\,s^{-1}}$. Similarly to the HEU plate, a preliminary isothermal calculation of the sieve was

performed to deduct the velocity profile at the inlet.

Outlet

At the outlet, the system pressure of FRM II of 2.3 bar was set as the average static pressure for the HEU plate. For the LEU plate, the outlet pressure was obtained by a hand calculation considering that the reduction of the flow area compared to the case without flow restrictor leads to an increase in velocity and subsequently a decrease in pressure [3]. From this, an average static pressure of 0.26 bar was set at the outlet.

Fluid Solid Interface

At the fluid-solid interface, the heat transfer is activated. Additionally, an absolute roughness of 2.4 µm is applied. This roughness value was calculated in [12] from the values provided in the licensing documents [5, 78].

9.1.5   Heating Data

A script retrieves the heat source needed to perform the thermal hydraulics calculations from Serpent 2. The flowchart of the script is shown in Figure 9.3. This script essentially compresses the power density calculated for the entire plate and coolant channels into the power density that can be deposited only in the fuel domains (Step 1). The heating data is then rotated by 2pi (Step 2), and only the data covering the fuel domain is kept (Step 3). Dr. Christian Reiter wrote and prepared the script as part of the Serpent 2-CFX coupling framework. The heating data shown in Step 3 in Figure 9.3 is the heating profile that is imported into CFX via the "Initialize Profile Data" tool. An additional variable responsible for the heating data's power density (HeatDep) is created and assigned to each fuel domain. Furthermore, a subdomain containing the high- and low-density fuels is created and assigned the said variable[1].

---

[1]Ansys CFX offers the possibility to include thermal radiation into the setup. Nonetheless, this approach is not considered since thermal radiation makes up for less than 1% of the total heat. Applying the Stefan-Boltzmann's law for radiation for a maximum temperature difference of 80 K in the fuel:

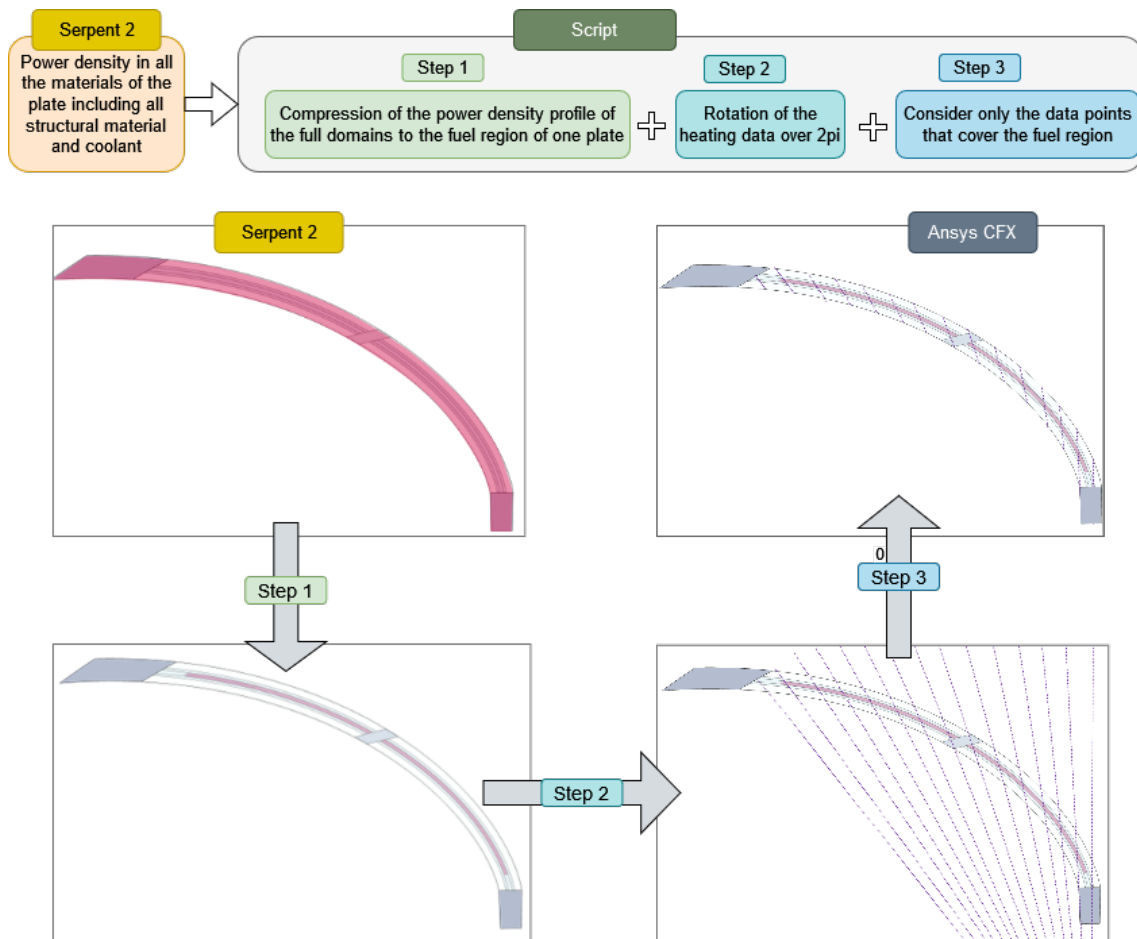$$\frac{P}{A} = \sigma \cdot \Delta T \approx 2 \, \text{W} \, \text{m}^{-2} \tag{9.9}$$

Figure 9.3: *The script workflow that transforms the heating data to be used by Ansys CFX. From Serpent 2, the power density obtained for all the domains is shown in red. In step 1, the red area is restricted only to the fuel region to show that the power density is compressed to the fuel. The power density data points (one line) are rotated over 2pi to cover the full radial range of the plate in step 2. In step 3, only the power density data points that cover the fuel area are taken into account.*

9.1.6 Material Properties

Water

The international steam tables IAPWS-97 [79], implemented in CFX, are used for the water material properties. This library expresses the water properties in a temperature- and pressure-dependent fashion. It also includes the properties for subcooled water, supercritical water/steam, superheated steam, saturation data, and high-temperature steam.

Cladding

The fuel plate cladding is made of AlFeNi. The literature regarding material properties of AlFeNi is rather sparse. However, the *Siemens* licensing report for FRM II [5] stated the thermal conductivity of AlFeNi to be around $216 \, \mathrm{W \, m^{-1} \, K^{-1}}$. Additionally, according to a document published by the International Atomic Energy Agency (IAEA) [80], the properties of AlFeNi are believed to be similar to the aluminum 8000 series, which exhibit a thermal conductivity ranging from $167 \, \mathrm{W \, m^{-1} \, K^{-1}}$ to $220 \, \mathrm{W \, m^{-1} \, K^{-1}}$ as stated in [81]. Based on this, the quoted value of $216 \, \mathrm{W \, m^{-1} \, K^{-1}}$ seems reasonable. No temperature variation of the thermal conductivity is taken into account.

For the specific heat capacity of AlFeNi, the c_p of pure aluminum is used, which is determined via [82]:

$$c_p^{\mathrm{Al}} \left[\mathrm{J \, kg^{-1} \, K^{-1}} \right] = 892 + 0.46 \cdot T[°\mathrm{C}] \tag{9.10}$$

Since the specific heat capacity of the cladding does not exhibit severe change over the temperature range of $40 \, °\mathrm{C}$ to $95 \, °\mathrm{C}^2$, a stable value of $903 \, \mathrm{J \, kg^{-1} \, K^{-1}}$ is used.

Aluminum Frame

The picture frame that surrounds the fuel meat is made of $\mathrm{AlMg_2}$, which has a noticeably lower thermal conductivity ($150 \, \mathrm{W \, m^{-1} \, K^{-1}}$) compared to AlFeNi. In the previous studies on the thermal-hydraulic behavior of FRM II, the frame was considered as AlFeNi based on the rationale that the low thermal conductivity is not expected to affect the overall results in a significant way. In this work, both cases were calculated, using the actual $\mathrm{AlMg_2}$ and AlFeNi for the picture frame to assess the influence and validity of the assumptions on the plate's thermal-hydraulic behavior. These calculations show that the previously made assumptions about the picture frame material are justified, as shown in Chapter 12.

---

²Roughly 3.8%

Quantity	Value inner fuel	Value outer fuel
ρ $(\mathrm{g\,m^{-3}})$	5.20	3.96
c_p $(\mathrm{J\,m^{-1}\,K^{-1}})$	475.0	630.4
k $(\mathrm{W\,m^{-1}\,K^{-1}})$	109	165

Table 9.3: *U_3Si_2 - Al material properties for the HEU core [5].*

Tubing

Even though the tubing of the core is made of AlMg$_3$, it was assumed to be AlFeNi. This assumption is justified by the fact that the tubing is not expected to have a high temperature; therefore, for the sake of simplification, all cladding and tubing material is set to AlFeNi. The results shown in Chapter 12 validate this assumption.

Dispersed U$_3$Si$_2$ - Al fuel

The current fuel of the FRM II is U$_3$Si$_2$ dispersed in an aluminum matrix, as mentioned in Chapter 1. The volume fraction of the porosity in the fuel can be calculated by [83]:

$$V_P = 0.072 \cdot V_F - 0.275 \cdot V_F^2 + 1.32 \cdot V_F^3 \qquad (9.11)$$

where V_F is the fuel's volume fraction, and the fuel accounts for the rest of the volume fraction. The specific heat capacity of U$_3$Si$_2$ is calculated as:

$$c_p^{\mathrm{U_3Si_2}} \left[\mathrm{J\,kg^{-1}\,K^{-1}} \right] = 199 + 0.104 \cdot T[^\circ\mathrm{C}] \qquad (9.12)$$

Then the heat capacity for the fuel is:

$$c_p^{\mathrm{U_3Si_2-Al}} \left[\mathrm{MJ\,m^{-3}\,K^{-1}} \right] = 0.0122 \cdot V_F \cdot c_p^{\mathrm{U_3Si_2}} + 0.0027 \cdot (1 - V_F - V_P)c_p^{\mathrm{Al}} \qquad (9.13)$$

The thermal conductivity of U$_3$Si$_2$ - Al fuel was measured at Argonne [82] in dependence on the uranium loading. Since the thermal conductivity of pure U$_3$Si$_2$ $\left(15\,\mathrm{W\,m^{-1}\,K^{-1}}\right)$ is about 14 times smaller than that of aluminum, reduction of the thermal conductivity of the fuel is expected when the uranium loading is increased. This is shown in Figure 9.4. From Figure 9.4, it can be deduced that the value for the thermal conductivity of U$_3$Si$_2$ - Al fuel is $180\,\mathrm{W\,m^{-1}\,K^{-1}}$ upon 13.7% U$_3$Si$_2$ volume fraction. This value agrees with the values reported on the licensing process of FRM II [5]. The temperature-independent values stated in Table 9.3 are used for this work.
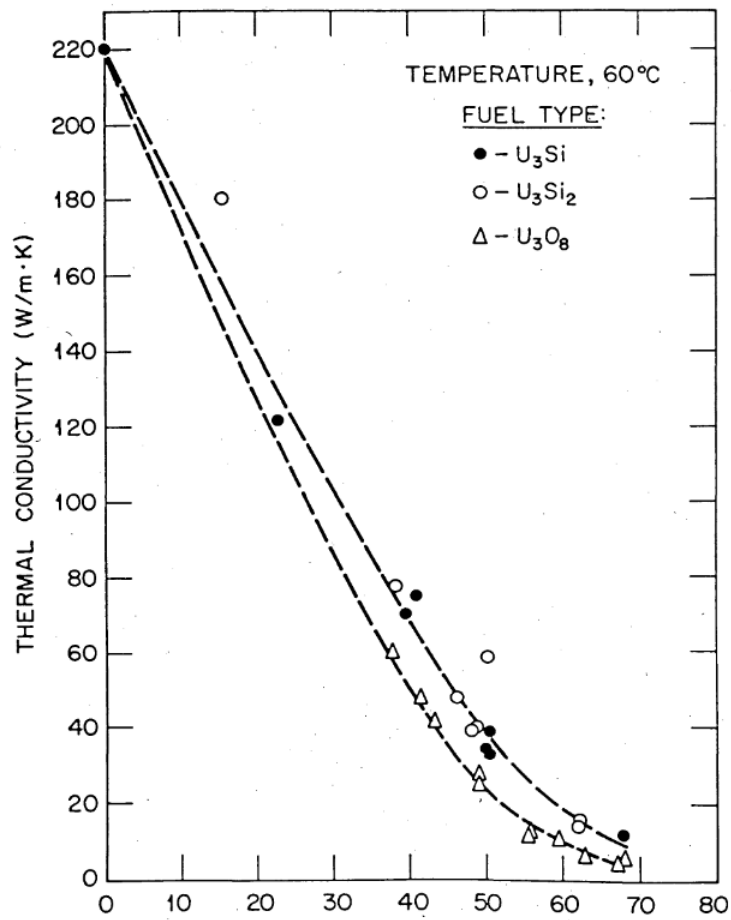
Figure 9.4: *Thermal conductivity of U_3Si_2 - Al in dependence to the volume uranium loading. Source: [82].*

Monolithic UMo fuel

Currently, a monolithic form of UMo is considered for the LEU core. In contrast to the uranium silicide dispersed fuel, the material data from the literature for the monolithic UMo is relatively bountiful since this fuel has also been the proposed option for the U.S. High-Performance Research Reactors (USHPRR) conversion.

One of the latest reports on the material properties of UMo alloys published at Argonne looks over the whole range of available studies on UMo [9]. The data shown here and used in the simulations constitute the best fit as presented in [9]. Furthermore, only the unirradiated material properties are used in this work.

Based on [9], the density can be expressed in a linear form in terms of temperature in the following relation:

$$\rho \left[\mathrm{g\,cm^{-3}} \right] = 17.15 - 8.766 \cdot 10^{-4} \cdot T \tag{9.14}$$

The specific heat capacity is given by:

$$c_p \left[\mathrm{J\,g^{-1}\,^{\circ}C^{-1}} \right] = 0.133 + 6.99 \cdot 10^{-5} \cdot T \tag{9.15}$$

The thermal conductivity can be given in terms of temperature:

$$k \left[\mathrm{W\,m^{-1}\,^{\circ}C^{-1}} \right] = 0.0355 \cdot T + 13.29 \tag{9.16}$$

Equation (9.16) is applicable in the temperature range from $50\,^{\circ}\mathrm{C}$ to $800\,^{\circ}\mathrm{C}$.

In the Serpent 2 – CFX LEU calculations, temperature-dependent material properties are defined by the above equations.

9.1.7   Initial Conditions

Simple conditions were assumed for initiating the analysis, such as $v_{in} = v_z = 9.83\,\mathrm{m\,s^{-1}}$, $T_w = T_{inlet} = 37\,^{\circ}\mathrm{C}$. The pressure was initialized with roughly $7.5\,\mathrm{bar}$. For the aluminum and fuel domains, slightly higher temperatures were used as initial conditions. In the transient calculations, the results obtained from the steady-state ones were used as starting conditions.

The thermal-hydraulic calculations' output parameters have an residual smaller than 10^{-5}. Additionally, all the quantities were monitored, and their convergence was confirmed.

9.2 Coupling

There are two approaches to couple Serpent 2 and CFX. The first approach consists on a so-called subsequent coupling, or one-way] coupling. This type of coupling relies on the subsequent data sharing between the codes. More specifically, first the Serpent 2 model is built and run. Then, the power density results are exported from Serpent 2 and imported to CFX by means of a profile initiation. The second approach is based on continuous data exchange between the codes. First, the Serpent model is solved and the power deposition is mapped onto the fuel domains in CFX. Then, CFX continues its routine with solving for temperature, pressure, velocity, density. Furthermore, the density and temperature profiles are transferred into Serpent 2. This loop progresses until a previously defined convergence criteria is reached in each code as well as globally. The full coupling is performed by means of a python wrapper.

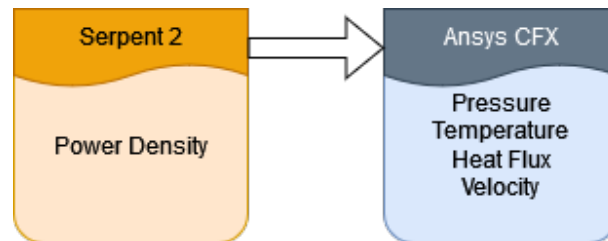The Serpent 2-CFX results shown in this thesis rely purely on the sequential coupling.

Figure 9.5: *A simple schematics of Serpent 2 - Ansys CFX subsequent coupling.*

CHAPTER 10

Thermal-Fluid-Structure Interaction (TFSI)

In this chapter, the approach of modeling the thermal-fluid-structure interaction is presented. The content is split in two parts: one-way and two-way Thermal-Fluid-Structure Interaction (TFSI). In each of these parts, the thermal mechanical, thermal hydraulics modeling and the coupling between the two are described.

10.1 One-way FSI

As mentioned in Chapter 7, the one-way TFSI refers to a sequential coupling between Ansys CFX (CFX) and Ansys Mechanical. The goal of this type of coupling is to assess the effects of the temperature and pressure fields on the deformation behavior of the plates. CFX is used to solve for the thermal-hydraulic behavior in a conjugate heat transfer approach. The CFX setup is equivalent to the model described in Chapter 9. The variables calculated by CFX such as pressure and/or temperature fields are inserted in Ansys Mechanical as boundary conditions. Moreover, the corresponding deformation and stress are calculated. The workflow for the one-way TFSI coupling is shown in Figure 10.1.

10.1.1 Thermal Hydraulics

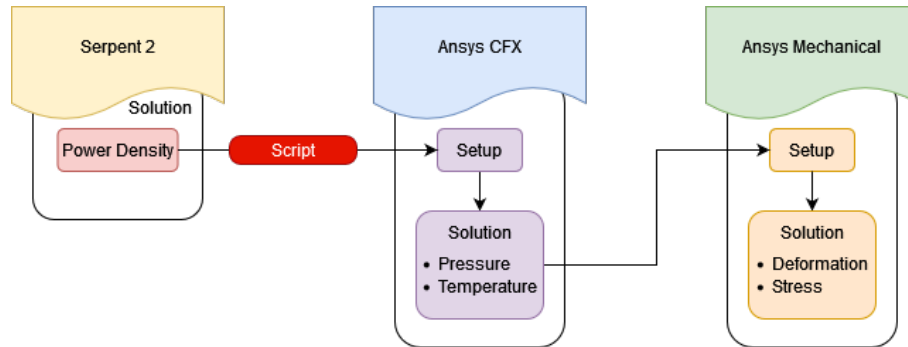The thermal hydraulics setup used for the one-way TFSI calculations is identical to the setup described in Chapter 9.

Figure 10.1: *Schematics of one-way TFSI used in this work. The power density calculated by Serpent 2 is post processed by means of a script which is described in Chapter 9. Furthermore, the pressure and temperature fields obtained by CFX are used as boundary conditions for Ansys Mechanical. The deformation and stress are calculated by Ansys Mechanical.*

10.1.2   Mechanics

The CAD model of the plate built in *SolidWorks*, was transferred to Spaceclaim[1] where the fluid domain was suppressed and the mesh of the solid parts, cladding, fuel and tubing was generated. The plate is meshed by hexahedra elements.

The bonded contact type is used to describe the contact between the fuel and cladding, plate and tubing, plate and combs. It implies that the surfaces where the contact is defined stay bonded and no separation can occur. A zero displacement boundary condition in all three directions is placed on the outer tubing surfaces and combs.

The load coming from the thermal hydraulics solver CFX, is imported and applied to the corresponding geometrical feature in Ansys Mechanical. For instance, the temperature of the fuel and aluminum domains from CFX is imported to the fuel and aluminum domains in Ansys Mechanical, while the pressure is imported and assigned to the fluid-solid interface. The zero-displacement surfaces are shown in Figure 10.2a and 10.2b for the Highly-Enriched Uranium (HEU) and Low Enriched Uranium (LEU) plates, respectively. CFX is able to import two types of results to mech, namely pressure and temperature. Therefore, for one-way TFSI, four cases were considered:

- Case 1: Only pressure load is used as a boundary condition in Ansys Mechanical.

- Case 2: Only temperature load is used as a boundary condition in Ansys Mechanical.

- Case 3: Both pressure and temperature loads are used as boundary conditions in Ansys Mechanical.

- Case 4: Both pressure and temperature loads are used as a boundary condition in Ansys Mechanical. Additionally, the combs are not fixed, but free to move.

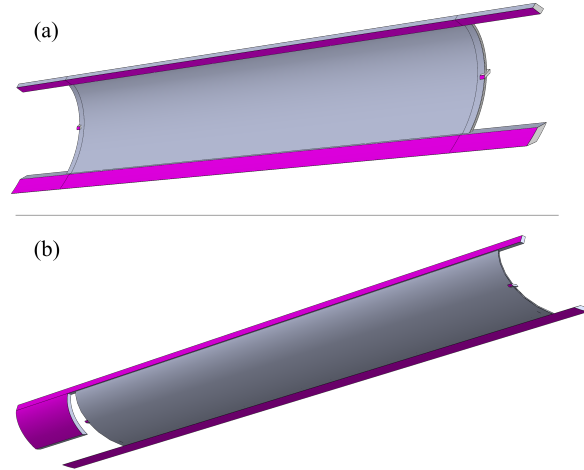[1]Spaceclaim is a meshing software, part of Ansys Products.

Figure 10.2: *The fixed boundary conditions in one-way FSI for the HEU plate (a) and LEU plate (b). Magenta expresses the fully fixed surfaces.*

10.2 Two-way FSI

In the two-way coupling, the power deposition from Serpent 2 is taken into account in the Ansys Mechanical solver. Therefore, the subsections here are referred to as Thermal Mechanics and Hydraulics. A simple schematics of the coupling is shown in Figure 10.3.

10.2.1 Thermal Mechanics

The structural setup in the two-way TFSI approach is similar to the one-way TFSI with a few exceptions. For instance, in the two-way TFSI, the fluid-structure interface is defined by
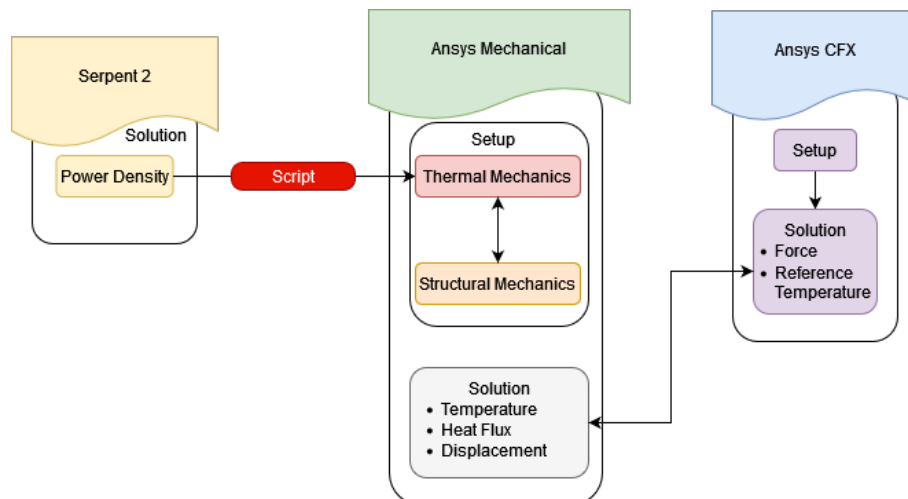

Figure 10.3: *Schematics of two-way FSI used in this work. The setup is built in Ansys Workbench.*

means of a boundary condition and it implies that system coupling transfers data between the structural solver and the hydraulic one. Furthermore, the two-way TFSI coupling includes a coupled structural-thermal setup. The thermal load which constitutes of the heat generation data exported from Serpent 2, is applied to the solid domain within Ansys Mechanical, in contrast to the one-way TFSI, where the power deposition is applied within CFX and the conjugate heat transfer solver is used. In order to create a structural-thermal coupling within the static structural application in Ansys Mechanical, commands assigning the power deposition to each mesh element are used. Additionally, the element type is switched to SOLID226. SOLID226 elements have displacement and temperature degrees of freedom, thus being able to represent the physics of a coupled thermal-structural solver.

10.2.2   Hydraulics

For the hydraulics setup, all the solid domains are omitted from the hydraulic solver. The water domain is split into three parts. The used mesh is exactly the same as the mesh described in Chapter 9, with the difference that here no solid domain is part of the meshing process.

For the inlet, the velocity profile calculated from the sieve (shown in Appendix VI) is used. The outcome of the preliminary sieve calculation is a developed velocity profile. The outlet boundary condition consists of a static pressure of 2.3 bars. A roughness of 2.4 µm is applied to the fluid-solid interface. The fluid-solid interface data exchange is set to "System Coupling", which implies that data such as force and temperature will be exchanged between CFX and Ansys Mechanical. Furthermore, the mesh deformation is activated.

10.3   Material Properties

Cladding

The Impulse Excitation Technique (IET) experiments described in Chapter 8 revealed the Young's modulus of the AlFeNi plate to be $74.24\,\text{GPa} \pm 0.05\,\text{GPa}$. This value is found to be conforming to the literature values that estimate the AlFeNi cladding to exhibit similar material properties as the aluminum 8000 series [80, 84], whose E-modulus ranges from $72\,\text{GPa}$ to $78\,\text{GPa}$ [81]. Therefore, in the mechanical calculations, the experimentally measured E-modulus of $74.24\,\text{GPa}$ was used for the cladding.

Picture Frame

$AlMg_2$ is the picture frame material with E-modulus of $68\,\text{GPa}$ and thermal conductivity of $150\,\text{W}\,\text{m}^{-1}\,\text{K}^{-1}$ [85].

Tubing

The material of the tubing is AlMg$_3$; however, since the tubing is a fixed boundary condition and it is not expected to reach high temperatures AlFeNi was used instead of AlMg$_3$, same as in [12].

U$_3$Si$_2$ - Al fuel

The Young's modulus of the fuel plate measured with IET is $75.83\,\text{GPa} \pm 1.69\,\text{GPa}$, a value which is comparable to the E-modulus of the AlFeNi plate. For both fuel densities, the mechanical calculations use the E-modulus of $75.83\,\text{GPa}$.

The influence of statistical uncertainty of the material properties measured by IET on the deformations is entirely negligible. The related-sensitivity analysis is shown in Appendix VI.

UMo

The best fit of the material properties summarized in [9] is used in this work. The material properties used in the thermal-hydraulic calculations, such as density, specific heat capacity, and thermal conductivity of UMo are shown in Chapter 9. Young's modulus, yield strength, and thermal expansion are shown here.

The Young's modulus in terms of temperature is given by:

$$E_{UMo}[\text{GPa}] = 90 - 0.13T \tag{10.1}$$

where T is in °C.

The yield strength as provided in [86] is:

$$\sigma_{UMo}[\text{MPa}] = 1027 - 1.48T \tag{10.2}$$

where T is in °C.

As for the Poisson ratio, the value of 0.35 is used, as stated in [9].

The thermal expansion can be calculated by:

$$\alpha = 7.91 + 0.0121T \tag{10.3}$$

α is given in $1 \cdot 10^{-6}\,1/\text{K}$ and the temperature in K.

In the mechanical simulations, the material properties at room temperature are used. The properties are summarized in Table 10.1.

Material	Thermal Expansion Coefficient (K^{-1})	Thermal Conductivity $(\text{W}\,\text{m}^{-1}\,\text{K}^{-1})$	Density $(\text{kg}\,\text{m}^{-3})$	Specific Heat Capacity $(\text{J}\,\text{kg}^{-1}\,\text{K}^{-1})$	Young's Modulus (GPa)	Poisson's Ratio (-)
AlMg_2	23	150	2700	900	68	0.33
AlFeNi	23	216	2770	903	74.2	0.33
Fuel 3.0 gU/cc	15.2	109	5200	475	75.8	0.30
Fuel 1.5 gU/cc	15.2	167	3960	630	75.8	0.30
Fuel UMo	11.5	15	17100	142	88	0.35

Table 10.1: *Material properties at room temperature used in the computational models. Sources: [5, 80, 81, 85].*

Part IV

Results

CHAPTER 11

Verification and Validation

In this chapter, the semantics of verification and validation and their meaning related to high-flux research reactors are laid out in the first and second section, respectively. The two experiments used for verification and validation are described and their simulation results are shown and discussed in detail.

11.1 Semantics of Verification and Validation

Verification and validation are synonyms in the English language. However, a distinction can be made between these two words in terms of quality assurance related to building confidence in Computational Fluid Dynamics (CFD) and Computational Structural Mechanics (CSM) calculations. This being said, the difference between verification and validation is established by Boehm [87], Blottner [88] and Roache [89]:

> *"Validation ≈ solving the right equations."*
> *"Verification ≈ solving the equations right."*

In CFD and CSM, the code user defines which partial differential equations and boundary conditions are being solved and shows that they are solved correctly and consistently within the chosen accuracy order. This is known as verification. Validation, on the other hand, is whether the equations represent the physics of the problem at hand which is observed and characterized in an experiment [90]. In the strict sense of the word, a "code" cannot be validated; only a range of calculations performed with a code can be validated. A code can be verified for various problems; however, using a verified code for a new problem is insufficient. Therefore, for simulating a new problem, the numerical errors or uncertainties must be tackled by performing mesh convergence tests.

11.2 Code Verification and Validation for High-Flux Research Reactors

Commercial CFD and CSM codes are widely used for various applications, including nuclear power plants [91, 92]. However, their usage for problems related to high-flux research reactors, such as Forschungs-Neutronenquelle Heinz Maier-Leibnitz (FRM II), High Flux Isotope Reactor (HFIR) and High Flux Reactor (RHF), is sporadic. Therefore, to rely on these codes for future projects, they must be verified and validated for high-performance research reactor conditions. Additionally, building confidence and credibility in using commercial codes is highly beneficial to the Low Enriched Uranium (LEU) conversion process. As mentioned in Section 11.1, experimental data that reflect the key features of high-flux research reactors is essential. However, the availability of these experiments is not abundant. Two experiments assessing the behavior of high-flux research reactors are Gambill & Bundy and Cheverton & Kelley experiments, performed as part of HFIR licensing. In the present work, the code verification relies on the code-to-code comparison of numerical solutions. The code validation is based on comparing the simulation results to an experimental outcome.

Ansys CFX (CFX) is validated using the Gambill–Bundy experiments and verified further within Involute Working Group (IWG) with Star-CCM+ and Comsol (see Chapter 11.3). Similarly, Ansys Mechanical is validated with Cheverton–Kelley experiments and verified against Star-CCM+ and Comsol (see Chapter 11.4). In the verification and validation (V&V) process, only the results obtained with CFX and Ansys Mechanical are shown, since these are the codes of choice for this work. For further details regarding the comparison between codes, the reader can refer to the corresponding publications [15, 16, 38, 93, 94].

11.3 Gambill-Bundy Experiments

In the early 60s, Gambill and Bundy performed a few thermal-hydraulic tests in the framework of HFIR program. As the reactor design was being finalized, a research paper regarding the forced convection of water in heated thin rectangular channels was published by Levy et al. [95]. In this paper, the authors suggested that the heat transfer coefficient for forced convection in a rectangular channel is 15% to 30% lower than in a round tube and 32% to 57% lower than the Sieder-Tate correlation predicts. Hence, Gambill and Bundy were tasked with performing tests of a HFIR representative model and conditions, studying the heat transfer coefficients, and determining the correlation best suited to HFIR thermal-hydraulic safety analysis. HFIR, RHF and FRM II are very similar to each other. Therefore, by extension, Gambill-Bundy experiments are also representative for RHF and FRM II.

The experimental setup consists of an electrically heated vertical rectangle aluminum channel. The water coolant from a tank containing 1150 liters of water was pumped into the heated
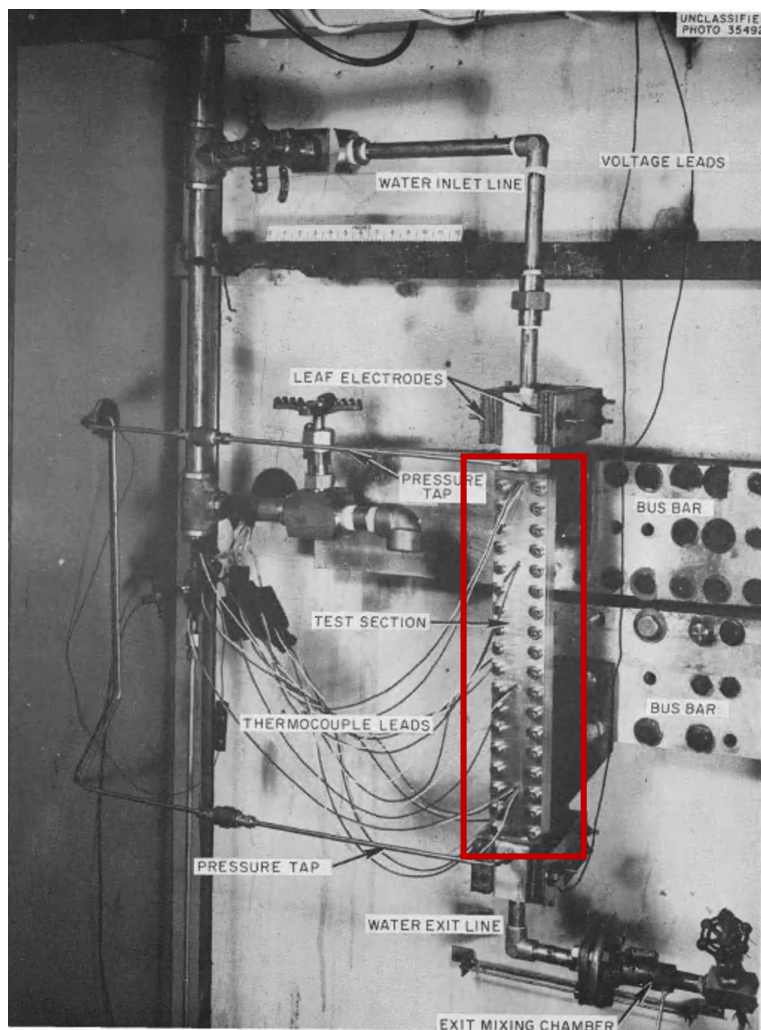
Figure 11.1: *Picture of the Gambill and Bundy experimental setup. The test section is shown in the red rectangle. Source:[13].*

section with a mass flow of roughly $0.277\,\mathrm{kg\,s^{-1}}$. Figure 11.1 shows a picture of the experimental setup. The test section consisted of the aluminum plate, Mycelex insulators, backup plates, and the end blocks. These parts are shown in Figure 11.2 and Figure 11.3.
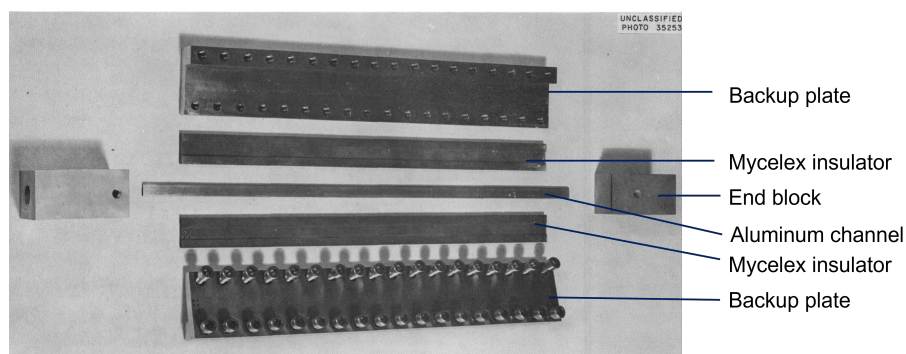

Figure 11.2: *The disassembled test section: the aluminum channel, including the insulator, backup plates, and end blocks, is shown. Source: [13].*
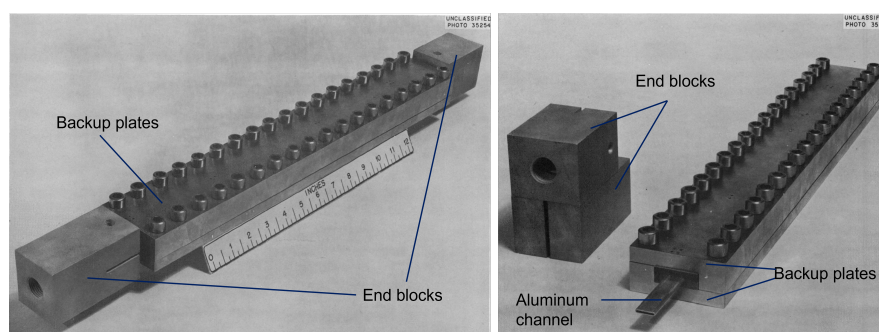
Figure 11.3: *The assembly of the test section. Source: [13].*

In order to measure the temperature of the wall and coolant, twelve thermocouples were placed every 5 cm on alternately opposing sides along the channel length. The pressure was measured by a gauge that was calibrated during steady-state operation. The inlet temperature was regulated by a steam beam coil and the test section was insulated. It was decided that the aluminum channel would not have a constant thickness due to possible heat flux peaking at the edges. The shape and dimensions of the channel are shown in Figure 11.5. In total, 11 experiments were performed; however, only run 8 of Test 7 is reported, also shown in Figure 11.4.

The bulk temperature was assumed to be increasing linearly with the channel length from $69\,^{\circ}\mathrm{C}$ at the inlet to $154\,^{\circ}\mathrm{C}$ at the outlet. According to [13], a calculation was done and this assumption was deemed acceptable. The thermocouples measured the temperature at the outer wall and evaluated the temperature drop through the wall as:

$$\Delta t_w = \frac{\phi\alpha}{2k} \tag{11.1}$$

where ϕ is the wall to water heat flux, α is the thickness of the channel and k is the thermal conductivity of aluminum. The wall temperature went from $111\,^{\circ}\mathrm{C}$ to $209\,^{\circ}\mathrm{C}$ from inlet to outlet. The wall roughness was $1.6\,\mathrm{\mu m}$ and the local heat transfer coefficient was calculated by:
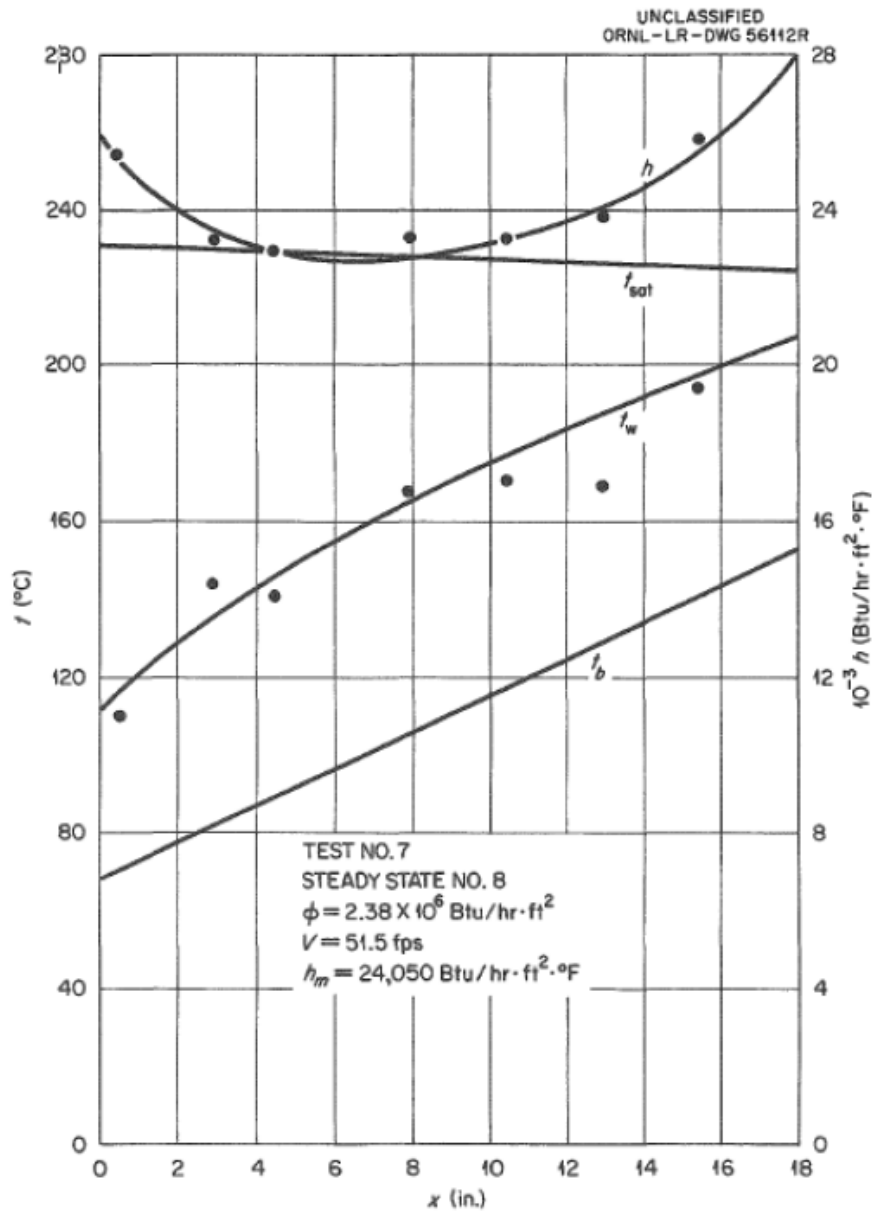
Figure 11.4: *Plot showing the variation of the wall temperature, bulk temperature, saturation temperature, and heat transfer coefficient from Test 7, run 8. Taken from Gambill–Bundy report [13].*

$$h = \frac{\phi_x}{(t_{wall} - t_{bulk})_x} \tag{11.2}$$

where the index x is the distance from the heated inlet.

In their report, Gambill and Bundy compared the experimentally determined heat transfer coefficients to Sieder-Tate and Hausen correlations. For Sieder-Tate, it was concluded that Equation (2.11) with a correction of 0.024 is representative of HFIR conditions, while for Hausen correlation a correction of 0.105 in Equation (2.12) was proposed.

11.3.1 Simulation of Gambill and Bundy experiments with Ansys CFX

Throughout the timeline of this thesis, there have been many developments in modeling the Gambill-Bundy experiments utilizing CFD codes within IWG. This multi-dimensional work has resulted in different publications [15, 38]. In mid 2023, a rather large analysis of an extended range of Reynolds numbers in a reduced geometry was performed. The CFD results of the Gambill-Bundy simulations that are presented here are based on an expanded version of already published material [15, 38]. Furthermore, in this thesis, only the results obtained with CFX are shown. The interested reader can refer to [96].

11.3.1.1 CAD Model and Mesh

The computer-aided design (CAD) model used in these simulations was built in *SolidWorks* and included the aluminum and water domains. An extra 10 cm long unheated extension was attached to the inlet, allowing the flow to develop before going into the heated section. The full CAD model is shown in Figure 11.5. The geometry was then meshed by using ICEM CFD[1]. Two different mesh densities with different y^+ values were explored, a fine one with $y^+ < 1$ and a coarse one with $y^+ \approx 30$. Both meshes are shown in Figure 11.6.

11.3.1.2 Material Properties

The water material properties were taken from the international steam tables IAPWS-97 [79]. The material properties of AA-6061 aluminum type were used for the aluminum channel. The fluctuation of the density, specific heat capacity and thermal conductivity in the expected temperature range (149 °C - 288 °C) was deemed negligible. Table 11.1 gives the used material property values.
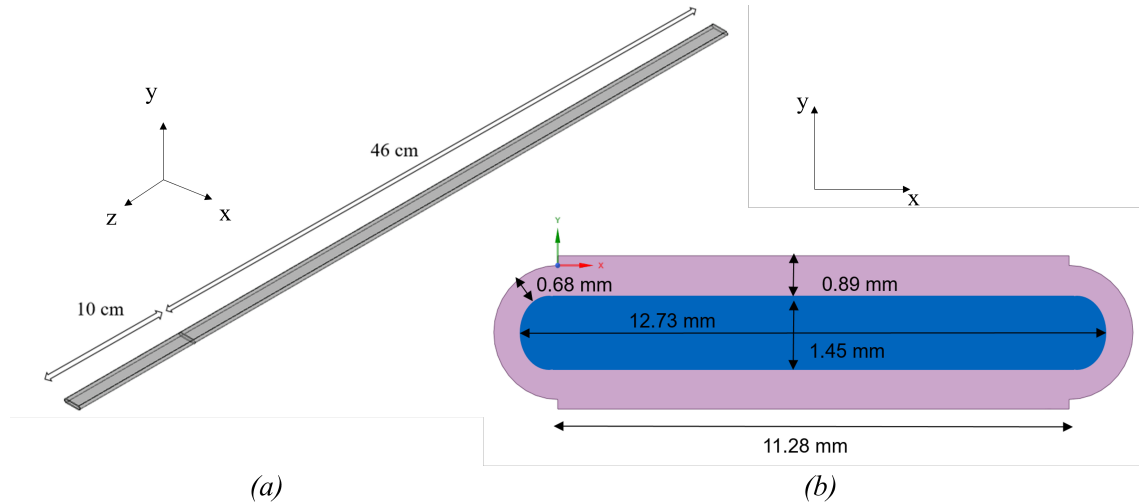
---

[1]Meshing software part of Ansys Product Suite

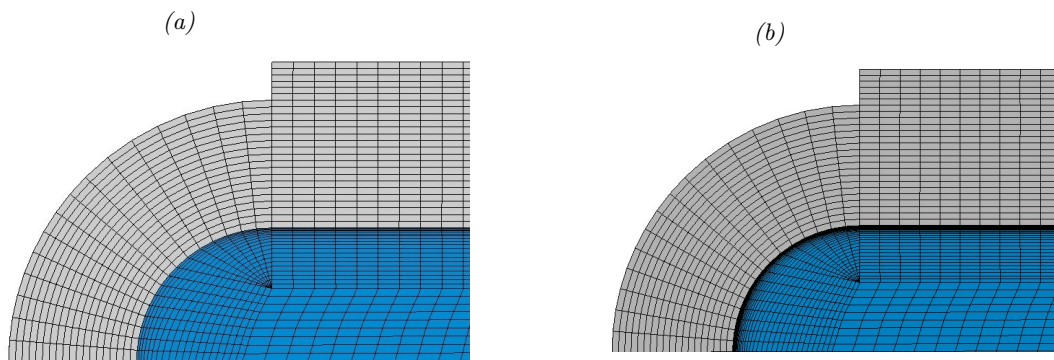**Figure 11.5:** *The isotopic (a) and top (b) view of the CAD representing the Gambill & Bundy test section.*

Figure 11.6: *The coarse mesh (a) and the fine mesh (b) used for calculations.*

Material Property	Value
Density ($\mathrm{kg\,m^{-3}}$)	2700
Specific heat capacity ($\mathrm{J\,kg^{-1}\,K^{-1}}$)	903
Thermal Conductivity ($\mathrm{W\,m^{-1}\,K^{-1}}$)	235

Table 11.1: *Material properties used for the aluminum domain.*

11.3.1.3   Boundary Conditions

The following boundary conditions were applied to the setup:

- Inlet velocity v_{in} = $15.7\,\mathrm{m\,s^{-1}}$

- Inlet temperature $T_{in} = 69\,°\mathrm{C}$

- Outlet pressure $p_{out} = 27.9\,\mathrm{bar}$

- Wall roughness $= 1.6\,\mathrm{\mu m}$

Since the Gambill and Bundy report does not contain specific information regarding the heat applied to the aluminum channel, a value for the heat source was estimated from the published data using:

$$Q = mc_p\Delta T \tag{11.3}$$

where ΔT is the difference between outlet and inlet temperature, about $82\,°\mathrm{C}$ in this case. c_p and m are the specific heat capacity at constant pressure and mass of water, respectively.

In order to properly simulate the Joule heating of the aluminum channel without adding unnecessary computational complexity to the setup, a volumetric heat depending on the electrical resistivity was applied. Furthermore, due to the dependence of the electrical resistivity on the temperature, the heat generated in aluminum increases with temperature. The total power generated by a current is calculated as:

$$P = I^2 R = I^2 \frac{\rho(T)}{A} l \tag{11.4}$$

The volumetric heat is then defined as:

$$\frac{P}{V} = \frac{I^2}{A^2}\rho(T) \tag{11.5}$$

where P is the power, V is the voltage, I is the current, R is the resistance, $\rho(T)$ is the temperature-dependent resistivity, A the cross-section and l the length of the heated channel.

The resistivity of the aluminum was defined as [97]:

$$\rho(T) = \rho_0(1 + \alpha \cdot (T - T_0)) \tag{11.6}$$

where $\rho_0 = 2.99 \cdot 10^{-8}\,\Omega\,\mathrm{m}$ at $293.15\,\mathrm{K}$.

The data extraction was done in the following way: all the bulk-related variables such as bulk velocity, density, specific heat capacity, thermal conductivity and bulk temperature are extracted as mass flow average at 6 xy-planes located at different heights from the outlet, exactly as in the experiments:

- Plane 1: z=0.42 m

- Plane 2: z=0.34 m

- Plane 3: z=0.26 m

- Plane 4: z=0.19 m

- Plane 5: z=0.114 m

- Plane 5: z=0.038 m

The wall properties, such as wall temperature and heat flux, were extracted at a point located at the wall in the middle of the channel in x-direction. Furthermore, the viscosity values at wall and bulk temperatures are calculated via temperature-dependent polynomials such that:

$$\mu = T^3 \cdot 1 \cdot 10^{-9} + 3 \cdot 10^{-7} \cdot T^2 - 3 \cdot 10^{-5} \cdot T + 0.0015 \tag{11.7}$$

For the plots presented in Section 11.3.2, the Nusselt number (Nu) number is plotted in terms of Reynolds number (Re) number. The Nu number normalized to Re number according to Hausen correlation, shown in Equation (2.12), is:

$$Nu_{H-Norm} = \frac{Nu_x}{Pr^{1/3}} \left[1 + \frac{1}{3} \left(\frac{D}{L_h} \right)^{2/3} \right]^{-1} \left(\frac{\mu_w}{\mu_b} \right)^{0.14} \tag{11.8}$$

Nu number normalized to Re number according to Sieder-Tate correlation is:

$$Nu_{ST-Norm} = \frac{Nu_x}{Pr^{1/3}} \cdot \left(\frac{\mu_w}{\mu_b} \right)^{0.14} \tag{11.9}$$

The Nu number evaluated at a position x is :

$$Nu = \frac{h_x \cdot d_h}{k_x} \tag{11.10}$$

where h_x and k_x are the heat transfer coefficient and coolant thermal conductivity at axial position x, respectively.

11.3.2   Results

The wall temperature profiles calculated using CFX are shown in Figure 11.7. For the coarse mesh (Figure 11.7a), all three turbulence models calculate similar wall temperature, with the largest relative difference of 3.5% between SST and RS (see Chapter 4.3). Nevertheless, the wall temperature values obtained by CFD compare well to the experimental data with a maximum statistical deviation of 10%. For the fine mesh, the wall temperatures calculated by K-ϵ and RS model are roughly $8\,^{\circ}\mathrm{C}$ (0.04%) higher than for SST. This can be related to the scalable wall functions used in K-ϵ and RS. The scalable wall function limit the turbulence implementation at $y^+ = 11.06$, while SST can resolve the turbulence in all y^+ ranges. The turbulence models show a change of the slope of wall temperature profiles at the beginning of the channel, while in the experimental data, such a phenomenon is not observable. It is important to note that in the experimental setup, aluminum parts surrounded the test section at the inlet, which could potentially enhance heat conduction from the test section. These aluminum end blocks were not simulated in CFX; thus, the slope may vary. Furthermore, the slope is more prominent in the simulations that use fine meshes. This is due to the fact that the fine mesh has a higher element count, and therefore, more data points are available. The modeling of the surrounding components in CFX was not achievable since insufficient information was provided in the experimental report. Going from the inlet to roughly $5\,\mathrm{cm}$ into the test channel, the discrepancy between the experiment and the simulations is substantially reduced. For $5\,\mathrm{cm}$ from the heated inlet until the end of the channel, the calculated wall temperatures are within the experimental data points in both coarse and fine meshes.
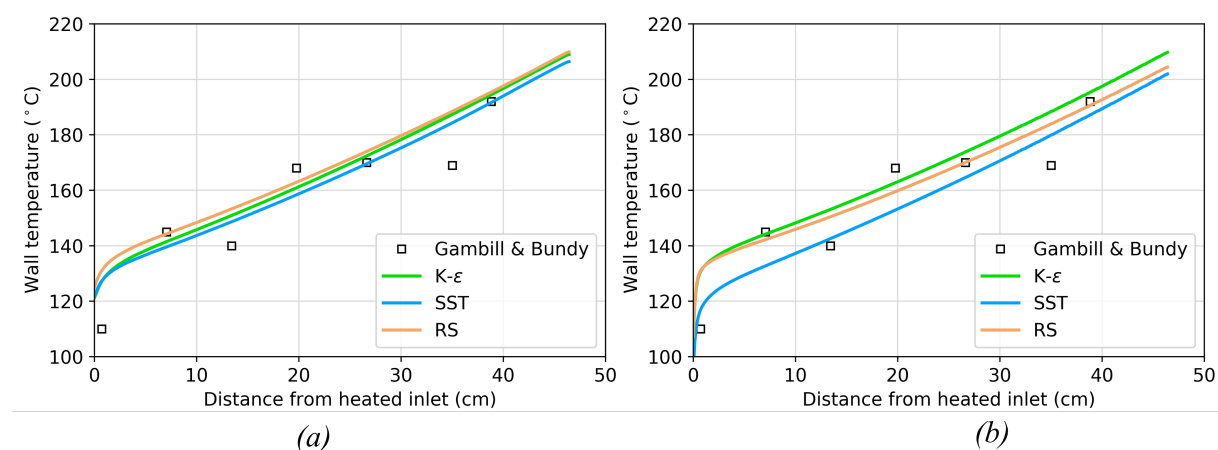

Figure 11.7: *The comparison between the wall temperature values measured by Gambill & Bundy and calculated by Ansys CFX for the coarse (a) and fine mesh (b).*

The results of CFX compared to the experimental data and the Hausen and Sieder-Tate correlations are depicted in Figure 11.8 and Figure 11.9, respectively. The comparison between coarse and fine mesh is also shown for each correlation. Depending on the correlation used in each plot (Hausen or Sieder–Tate), the ordinate and abscissa of the plot is modified accordingly.

For example, in Figure 11.8, the results obtained with Hausen correlation are shown by plotting the Nu normalized according to Hausen correlation shown in Equation (2.12). Therefore, the x-axis expresses the normalized Re as $Re^{2/3} - 125$. In Figure 11.9 where the results obtained with Sieder–Tate correlation are shown, simply Re number remains in the x-axis, since Sieder–Tate correlation depends on Re number as previously seen in Equation (2.11).

When using Hausen correlation on the coarse mesh (Figure 11.8a), all three turbulence models perform similarly, with a maximum Nu number deviation of 10% from the correlation. Nu numbers calculated for SST on the fine mesh are slightly higher than the Hausen correlation and the Nu number calculated for the same models with the coarse mesh. The SST turbulence model with fine mesh seems to estimate the Nu number values to be larger by roughly 7% compared to K-ϵ and Reynold Stress (RS) and approximately 12% from the Hausen correlation. However, Nu numbers calculated by all turbulence models have a good agreement with Nu numbers from the experiment.

A more significant similarity is observed for Nu number calculated by CFX and the Sieder-Tate correlation. For the coarse mesh, all three turbulence models perform alike. For the fine mesh, Nu number calculated by the SST turbulence model is larger by roughly 8% from RS and K-ϵ turbulence model and about 10% from the Sieder-Tate correlation.
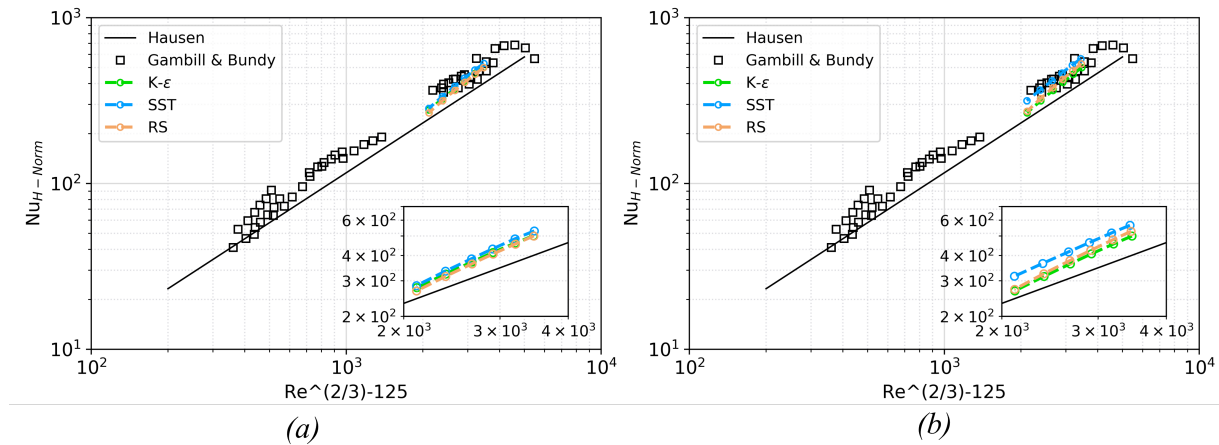

Figure 11.8: *The comparison between the Gambill & Bundy experiment, Hausen correlation and the Ansys CFX outcome for the coarse (a) and fine mesh (b). The term $Re^{2/3} - 125$ is x-axis expressed the normalized Re according to Hausen correlation.*

The heat transfer coefficients were calculated in each case for 200 axial positions using Equation (11.2). The results obtained by CFX are shown in Figure 11.10 in comparison to the experimental data from Gambill and Bundy. In principle, the CFX results reproduce the experimental trend that the heat transfer coefficient undergoes a sharp decrease at the inlet followed by an increase as the flow proceeds through the channel. Gambill and Bundy suggested that the steep decrease of the heat transfer coefficient at the inlet emerged from the thermal boundary layer development. This effect is less prominent in the CFD calculations as a result of the
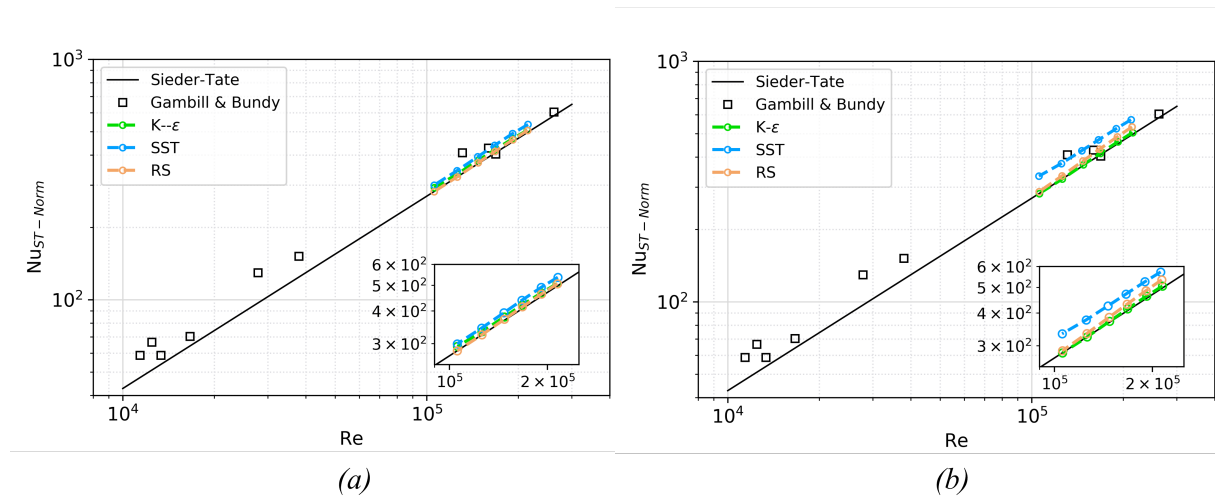
Figure 11.9: *The comparison between the Gambill & Bundy experiment, the Sieder-Tate correlation and the Ansys CFX outcome for the coarse (a) and fine mesh (b).*

simplifications made at the inlet section. The discrepancy between the experiments and the CFX simulation is expected to diminish if the heat conduction between the channel and end blocks at the inlet is modeled. Further along the channel, the heat transfer coefficient increase is similar for all three turbulence models for coarse and fine meshes. SST calculates higher heat transfer coefficients in both coarse and fine meshes than K-ϵ and RS. This is expected since SST turbulence model resolves the boundary layer better than the K-ϵ model, thus increasing the efficiency of the heat transfer process. A similar statement can be made for the RS model used here, since it uses the same scalable wall functions as K-ϵ (see Chapter 4.2.1).
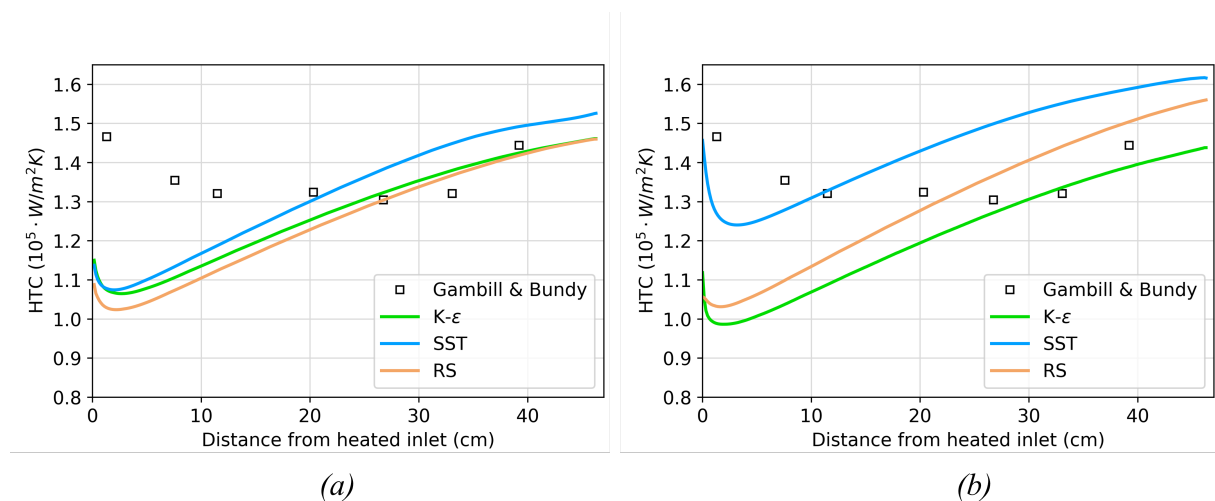

Figure 11.10: *The comparison between the heat transfer coefficients from Gambill & Bundy experiment and Ansys CFX outcome for the coarse (a) and fine mesh (b).*

11.3.3 Conclusions

Overall, all turbulence models provide results that match the well-known empirical correlations, such as Hausen and Sieder-Tate. The maximum difference between CFD and correlations is 10% for Hausen. Furthermore, it was shown that the heat transfer process can be captured well with all three turbulence models, especially at the end of the channel. The verification of CFX towards other CFD codes is shown in [15]. The differences between CFD codes can arise on account of different discretization methods.

Based on this analysis and previous work done by IWG, it is crucial to confirm that CFX is able to provide computational results comparable to corresponding experimental data. Furthermore, the comparison of CFX results to other CFD codes, such as Star-CCM+ and Comsol, gives additional assurance on the validity of the computational methods. Therefore, it is concluded that CFX is verified and validated and can be used as a prediction tool during further analysis.

11.4 Cheverton-Kelley Experiments

Cheverton and Kelley [14] performed a series of experiments in the late 60s intending to evaluate the plate stability under thermal and pressure differential conditions on the HFIR reactor during its licensing process. The experiments were performed on a mock-up of the HFIR outer involute fuel plate.

The HFIR core has two concentric fuel elements, where each plate is spot welded to the side plates in 24 locations along the length of the plate. The plates in the inner cylinder have a smaller involute radius; therefore, they are more curved than those in the outer cylinder. It was concluded that the outer plate has a higher buckling tendency and was the subject to investigation. Consequently, the Cheverton-Kelley experiments rely on testing the buckling tendency of HFIR's outer plate under temperature and pressure loads. In an involute plate-type reactor, the temperature distribution in one plate is not uniform due to the varying power profile dependent to where the absorber materials are located in the reactor core. Furthermore, the possible imperfections on the involute plates can induce different pressure differentials on each side of the plates that affect the buckling behavior. Exploring the replicability of the Cherverton-Kelley experiments using CSM is crucial since a successful simulation of these experiments is not only essential to the CSM code validation. Additionally, the influence of different pressure and temperature loads on the deformation behavior of involute plates deepens the general understanding of the mechanical behavior of involute plate-type reactors. The comprehension of involute plate deformation and buckling can be further used during the FRM II conversion process.

Cheverton and Kelley performed several tests with a uniform temperature load up to 316 °C, uniform pressure load of 207 kPa, as well as temperature and pressure load applied simultaneously. 24 tabs were attached to each side of the plate to imitate the welding spots. Two types of tabs with 6.35 mm and 3.175 mm width were tested. In addition to the solid base, a split base was used in a few tests to replicate the rotating side plates of HFIR that allow for radial expansion of the plate. A few tests were performed by substituting 2 inches on both ends of the plate with steel to represent the unfueled regions at the HFIR plate, also called "cold" ends.

The experimental setup is shown in Figure 11.11. It includes the plate attached to a base, on top of which a bridge with seven styluses measuring the deformation of the plate was installed. The positions of the styluses along the involute arc length were: (1) 3.175 mm, (2) 14.605 mm, (3) 26.035 mm, (4) 37.465 mm, (5) 48.895 mm, (6) 60.325 mm, (7) 71.755 mm. The styluses are shown in numbers in Figure 11.11b. Furthermore, the bridge was mounted on a track and could be moved axially for more measurements. The accuracy of styluses was reported to be 0.0254 mm [14]. In order to apply the temperature loads, the whole experimental setup was put in an oven and brought to the desired temperature. The two short sides of the involute plate were sealed for the pressure load, and air with the required pressure was applied to the concave side.

In a few tests, the measured deflections fluctuated considerably. This was noticed to be stronger in the cases where the degree of end fixation was a variable. Furthermore, imperfections on the initial shape of the plate as well as slight changes in the shape of the plate caused by the installation, were observed. The deviation of the subjected plate from the involute reached up to 0.3 mm in the measured data. Three tests were performed on the plates to estimate the uncertainty of the deflections, which resulted to a maximum difference of 11% from the mean value [14].

11.4.1 Simulation of Cheverton–Kelley Experiments in Ansys Mechanical

In this section, the details of the simulation of Cheverton–Kelley experiments in Ansys Mechanical are presented. First, the geometry of the model is shown in Section 11.4.1.1. Furthermore, the material properties and boundary conditions are discussed in Sections 11.4.1.2 and 11.4.1.3. In Section 11.4.1.4, the outcome of mesh sensitivity analysis is shown. Finally, in Section 11.4.2 the results obtained with Ansys Mechanical are shown.

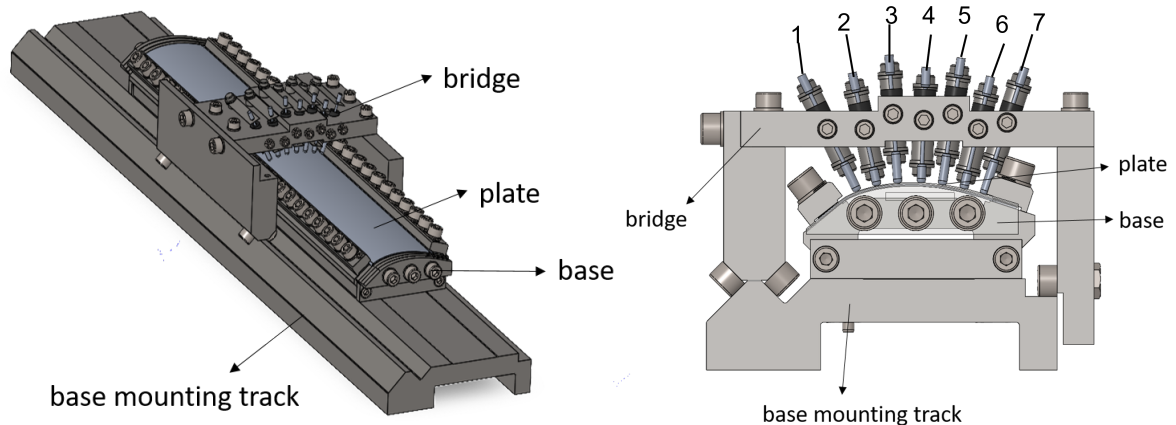#### 11.4.1.1 Geometry of the model

Figure 11.11: *The geometry of the model in a perspective view (left) and (right) a front view of the experimental setup. Source [16].*

Figure 11.12 shows the plate geometry with the tabs. The CAD model is built in *SolidWorks* with the support of a few pictures reported by Cheverton and Kelley. However, since the drawings are not sufficient in order to understand all the details necessary to build a CAD model, simple assumptions are made. For instance, the analysis does not include the bolts, screws, and other attachments. The pictures depicting the experimental assembly are shown in Figure 11.11.
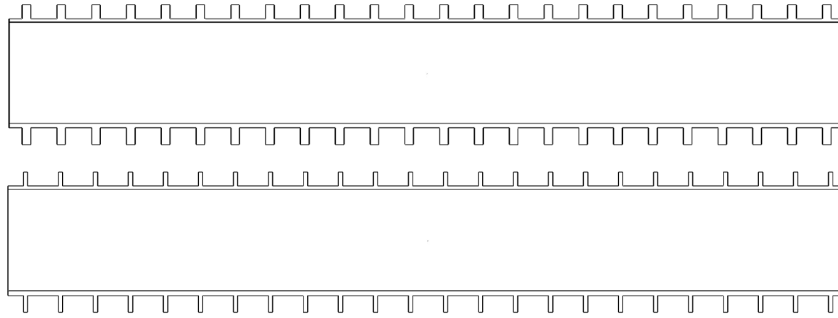
Figure 11.12: *Side view of the involute plate with 6.35 mm wide tabs (top) and 3.175 mm wide tabs (bottom). Source [16].*

11.4.1.2 Material Properties

Cheverton and Kelley experimented on two types of plates: a) aluminum plates with fuel and b) pure aluminum AA-6061-T0 plates. According to their report, the difference in deformation between the fueled and pure aluminum plates was small. Based on this statement, it was assumed that simulating the pure aluminum plate should give a reasonable estimate of the deformations for a "real" reactor plate [93]. For the cold ends, carbon steel was used. The base material was varied between Monel, Invar and carbon Steel, depending on the case. Cheverton and Kelley chose the base material based on their low thermal expansion coefficient ranging from $1.3\,\mu\text{m}\,\text{m}^{-1}\,\text{K}^{-1}$ for Invar to $12.9\,\mu\text{m}\,\text{m}^{-1}\,\text{K}^{-1}$ for carbon Steel. The specific values of the material properties were not mentioned in the original Cheverton-Kelley report. It was, however mentioned that the plate exhibited elastic behavior in most tests, with a few exceptions of plastic deformations in a few cases. The material properties used in this study were reported by Jain et al. [94] and Sitek et al. [93] in previous computational structural mechanics studies of the Cheverton-Kelley experiments. The material properties are shown in Table 11.2 and correspond to room temperature. Furthermore, an isotropic model was used for all the metals, representing the behavior in the elastic regime.

Material	Thermal Expansion Coefficient $(\mu\text{m}\,\text{m}^{-1}\,\text{K}^{-1})$	Thermal Conductivity $(\text{W}\,\text{m}^{-1}\,\text{K}^{-1})$	Density $(\text{kg}\,\text{m}^{-3})$	Specific Heat Capacity $(\text{J}\,\text{kg}^{-1}\,\text{K}^{-1})$	Young's Modulus (GPa)	Poisson's Ratio (-)
AA-6061-T0	23.26	167	2700	896	69	0.33
Carbon Steel	12.9	47.4	7850	477	203	0.29
Invar	1.3	10.15	8050	515	141	0.3
Monel	13.9	21.8	8800	427	169	0.295

Table 11.2: *Material properties used in the computational models at room temperature. Provided by [94].*

11.4.1.3   Loads and Constraints

Cheverton and Kelley experimented on a broad range of parameters. For the validation of Ansys Mechanical, 11 cases were taken into account, starting from simple setups containing only the plate under a pressure load and continuing to more complicated cases such as the plate mounted on a solid/split base under thermal load. These cases are chosen to simulate a variety of loads, materials and boundary conditions that summarize the experimental work done by Cheverton and Kelley. Cases 0-4 were performed with a pressure load, Cases 5-9 with a thermal load and Case 10 with both loads combined. Two models are proposed to simulate the experiments; one containing only the plate (Case 0-5), and the other one also containing the base and the plate (Case 6-10).

Single-plate Model (Case 0-5)

It has been shown in [93] and [94] that the model with a single plate can produce accurate deformations in the cases where no thermal load is present or the cases where the thermal load does not induce a significant deformation of the base in addition to the plate. Furthermore, the computational effort in the single plate model is substantially lower than in plate plus base models, enabling the simulation of a broad range of loads quickly.

Plate and Base Model (Case 6-10)

The base material in the CK experiments varied between Invar and Monel. Both these materials have lower thermal expansion coefficients than aluminum, allowing for a different level of constraint on the plate under thermal load. Furthermore, the steel ends that were attached to the plate in a few tests to simulate the unfueled regions in the HFIR plate introduce an additional constraint to the system. The bottom surfaces of the base have been constrained in the normal direction but are allowed to move in-plane. One edge at the middle of one end plate is fully constrained to eliminate rigid body motion. The location of the edge was chosen to have the least possible influence on the total deformation of the model. The base was used as a whole for two setups, Case 6 and Case 10. For Cases 7, 8 and 9, the base was split in two parts. Under a thermal load, the two parts of the base can move relative to each other, causing a displacement of the tabs and deformation of the plate. The CAD models for the solid and split base are shown in Figure 11.13a and Figure 11.13b, respectively.

The base model consists of the base (split or solid), the two top bars used for fixing the tabs, and two end plates. The contact implementation is the following: bonded contact between the base and the end plates, as well as the plate and the base, and no-separation contact between the thin strips and the base. The summary of the cases and the corresponding boundary conditions are summarized in Table 11.3.

In general, the deformations normal to the convex surface of the involute are obtained in different lengths of the plate. For instance, the extraction line for deformations at the mid-length plate, at the end plate and along the plate length is shown in Figure 11.14.
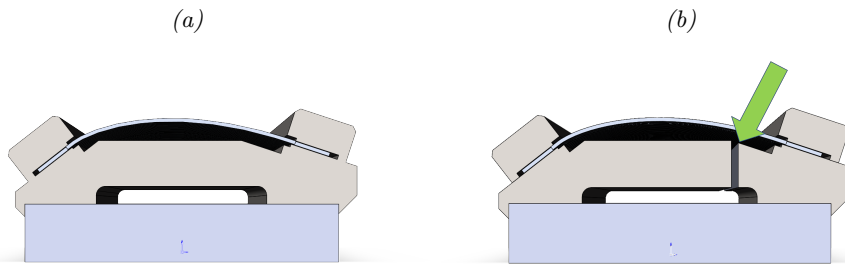
Figure 11.13: *The geometry of the solid (a) and split (b) base. In (b) the arrow points to the slit in the base. Source: [16]*
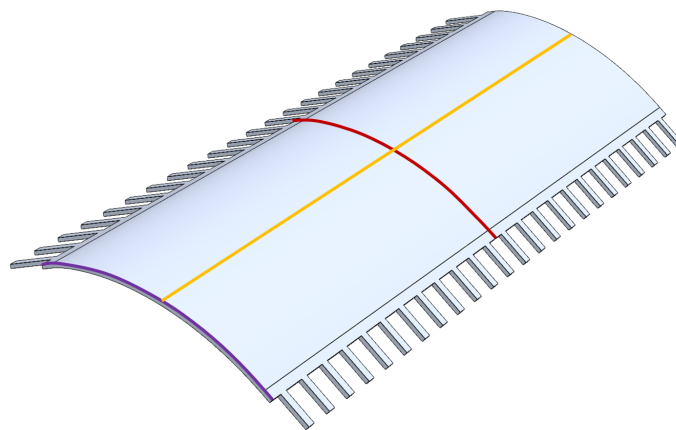

Figure 11.14: *The locations where the normal deformations are deducted. The red line refers to the mid-length plate, the purple to the end of the plate, and the orange to the data along the length of the plate.*
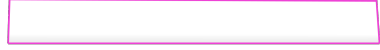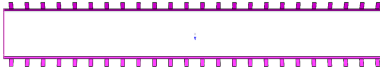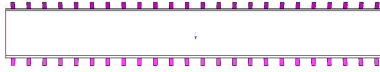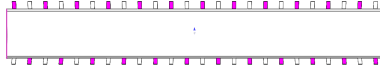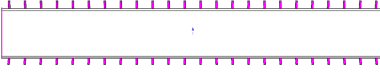
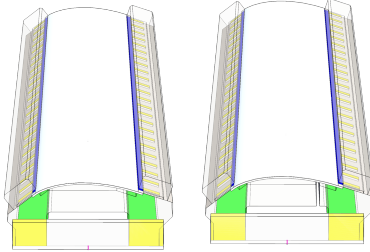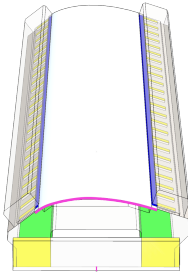| Case	Load	*Material*	*Constraint*
Ref C0	Uniform Pressure load 207 kPa applied to the concave surface of the involute.	Aluminum plate	
C1	Uniform Pressure load 207 kPa applied to the concave surface of the involute and the side strips of each plate. For each type of constraint, the load varies from 69 kPa to 207 kPa.		
C2			
C3			
C4			
C5	Uniform temperature load of 477 K. Initial temperature 300 K.	Aluminum plate	
C6		Aluminum plate, solid Invar base	
C7		Aluminum plate, split Invar base	
C8		Aluminum plate, split Steel base	
C9		Aluminum and steel plate, split Invar base	
C10	Uniform temperature load of 477 K. Initial temperature 300 K. Uniform pressure load equal to 207 kPa applied to the concave surface of the involute and the straight side strips of the plate.	Aluminum plate, solid Monel base	

Table 11.3: *Summary of each case simulated by Ansys Mechanical and the corresponding boundary conditions. The constraint of each model are shown in the last column. Magenta is referred to as zero displacements, the green as the zero normal displacements, while yellow and blue represent the bonded and compression-only contacts. Source: [16].*

11.4.1.4 Mesh Sensitivity Analysis

A mesh sensitivity analysis was conducted to find a suitable mesh in terms of accuracy-computational effort ratio for the plate under investigation. For this, the CAD model of the involute plate is meshed in SpaceClaim[2] with three different cell densities, shown in Table 11.4. The plate is then uploaded into Ansys Mechanical, where a pressure load of 69 kPa is applied to the concave side of the plate. Additionally, the tabs, as well as the short edges of the plate are fully constrained. Three mesh densities were calculated: a coarse mesh with 2 x 50 x 400 elements, a medium mesh with 4 x 100 x 400 elements and a fine mesh with 8 x 200 x 400 elements in thickness, span and length, respectively. The deformations normal to the convex surface were obtained and compared between the different mesh densities.

Mesh	# Nodes	Max Deformation (mm)	Min Deformation (mm)	Relative Change Max (%)	Relative Change Min (%)
Coarse	$1.89 \cdot 10^5$	0.057	-0.019	5%	6%
Medium	$6.27 \cdot 10^5$	0.059	-0.020	1%	1%
Fine	$21.7 \cdot 10^5$	0.060	-0.021	ref	ref

Table 11.4: *Mesh sensitivity analysis with three different mesh densities.*

The maximum normal deformation calculated by the fine, medium and coarse mesh is 0.06 mm, 0.057 mm and 0.057 mm. Since the relative difference in deformations between the medium and fine mesh is small and the computational effort for the medium mesh is substantially lower than the fine one, the medium mesh was selected for the study. Furthermore, the maximum normal deformations calculated by all three meshes do not exceed 0.06 mm, which is an acceptable value for a reactor. The normal deformations calculated with three different mesh densities are shown in Figure 11.15.
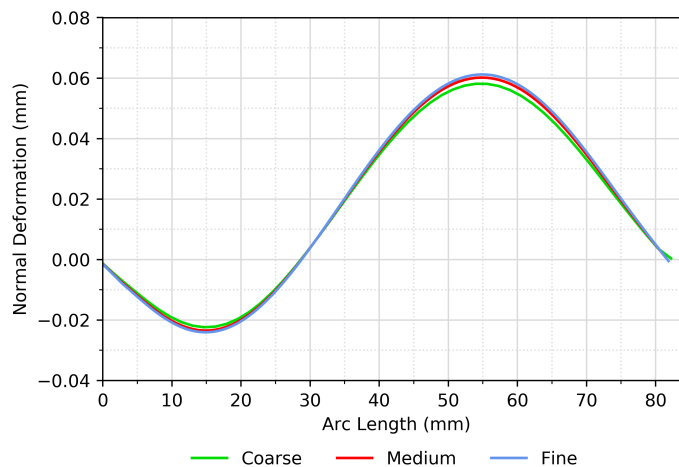

Figure 11.15: *Normal deformation at the plate mid-length as calculated with three different mesh densities in Ansys Mechanical. Refurbished from source [16] to focus on the Ansys results.*

---

[2]SpaceClaim is a meshing software part of Ansys product suite.

11.4.2 Results: Pressure Load

Reference Case C0

In order to get a better understanding of the replicability of Cheverton & Kelley experiments using Ansys Mechanical, a straightforward setup such as the involute plate without grooves nor tabs is first simulated under pressure loads using linear and nonlinear solvers. The pressure load of 207 kPa is applied to the concave surface of the involute plate, where the short and long edges of the plate are constrained. The primary goal of this calculation is to assess the dependence of the solution on the stress-displacement relationship. All the calculations were also performed with Star-CCM+ and Comsol as part of the IWG work frame to perform a thorough verification and validation of the used codes. This is, however, not part of the thesis; therefore no details related to the modeling in Star-CCM+ and Comsol are provided here. The interested reader can refer to the publication on this topic [16].

The normal deformations as shown in Figure 11.16, are extracted at an edge located at the mid length of the plate. The coordinate system is set so that negative displacements imply that the involute deforms towards the concave side, while positive displacement implies deformation towards the convex side. As mentioned in Chapter 5.3.1, the nonlinear solver is usually used in scenarios where the displacement is large compared to the smallest dimension of the body, which in this case is the thickness. As Figure 11.16 shows, the displacement calculated by the nonlinear solver is roughly 7 % of the plate thickness. Therefore, the upcoming calculations are only performed with the linear solver. The difference between the linear and nonlinear solutions is about 12.4% in Ansys Mechanical.
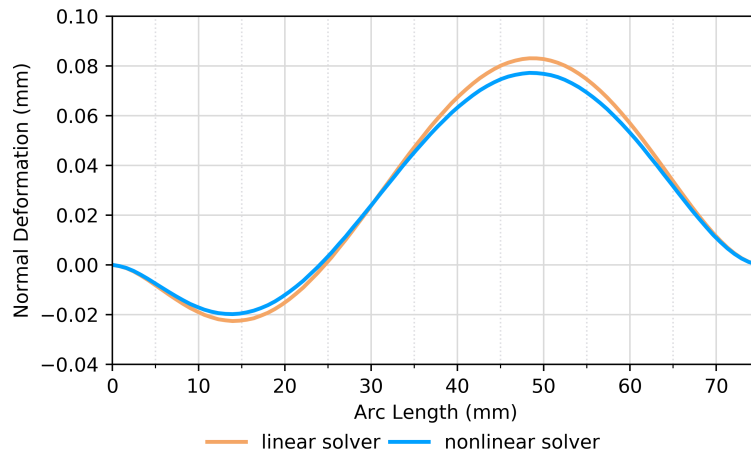

Figure 11.16: *The normal deformation calculated by using a linear and nonlinear solver in the reference Case 0. Refurbished from source [16] to focus on the Ansys results.*

Case 1 to Case 4

The normal deformations calculated in cases 1 through 4 are shown in Figure 11.17. In Case 1, 2 and 3, the tabs have 6.35 mm-wide tabs and the boundary conditions consist of all tabs and side strips being fixed in Case 1, all tabs fixed in Case 2, and every other tab is fixed in Case 3. Case 4 explores the 3.175 mm-wide tabs, where all the tabs are fixed. In all these scenarios, the short ends of the plate are fixed and the pressure load is applied to the concave surface of the involute in three-step loads: 69 kPa, 138 kPa and 207 kPa. The experimental deformations were taken from sensors #2 and #5 located at 14.6 mm and 48.9 mm arc length from the generating circle, respectively.

The normal deformations calculated by Ansys Mechanical agree very well with the experimental results in Case 1 with an absolute deviation of 0.0016 mm at 69 kPa, 0.001 mm at 138 kPa and 0.003 mm at 207 kPa, as seen in Figure 11.17a. Once the restriction on the side strips is lifted in Case 2, higher deformations are observed. This is conveyed well by Ansys Mechanical with a maximum difference between the calculated values and the experiment of 0.01 mm at 69 kPa, 0.009 mm at 138 kPa and 0.04 mm at 207 kPa. These results are shown in Figure 11.17b.

When the weld between the involute plate and the side plates in the reactor core is missing or has failed, the plate experiences an increase in deformation due to the lost constraint. This scenario is simulated in Case 3, where only every other tab is a constraint, while the rest are free to move. The normal deformations for Case 3 are shown in Figure 11.17c. The calculated deformation at 138 kPa is 0.038 mm smaller than the experimental result. At 207 kPa on the other hand, the code underestimates the deformations by approximately 0.14 mm. This comes as a result of the plate undergoing plastic deformation in the experiment. The calculations are unable to capture this behavior since the used solvers are linear and describe the plate behavior exclusively in the elastic regime (see Chapter 5.3).

The tabs width was reduced to 3.175 mm in Case 4 and the resulting deformations are shown in Figure 11.17d. The involute plate experiences slightly larger normal deformations compared to Case 2 due to the reduced tab width. The calculated deformations are in very good agreement with the experimental data at 138 kPa, with a maximum difference of 0.01 mm.
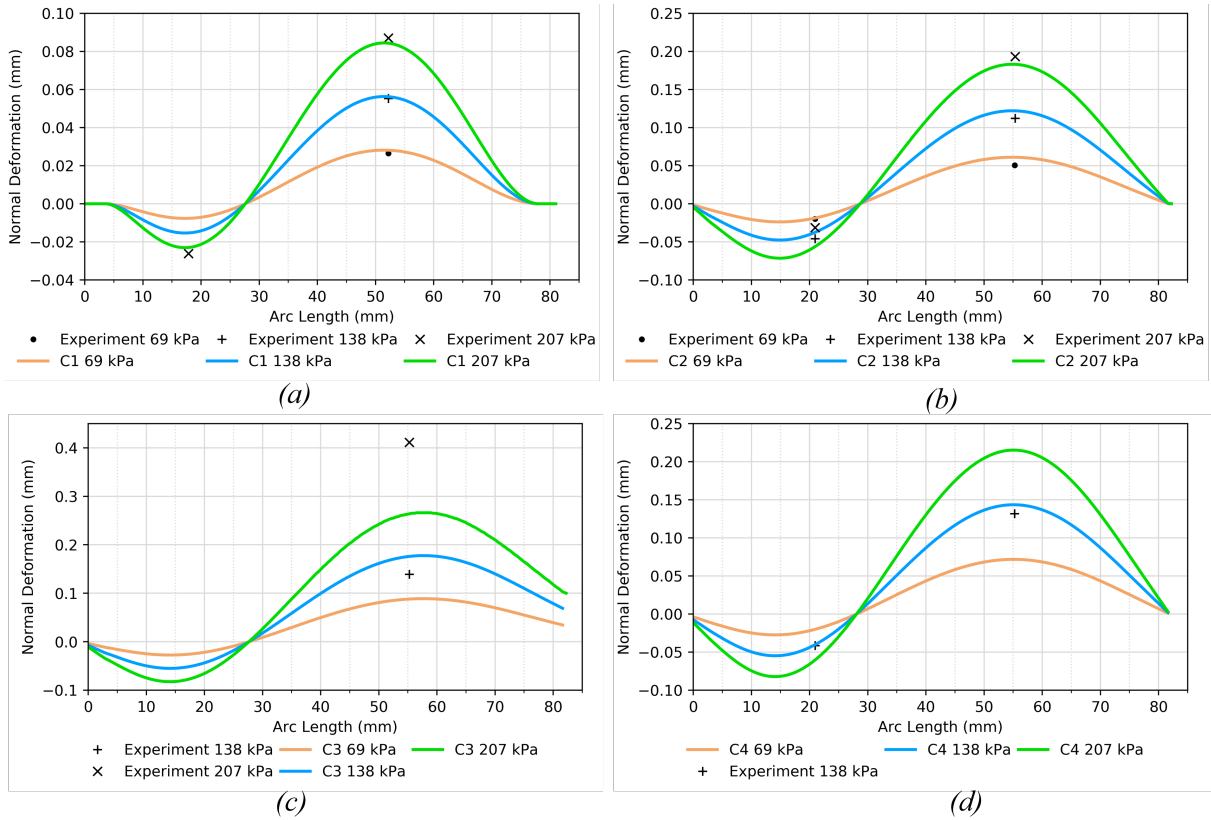
Figure 11.17: *The normal deformation calculated at the plate's mid-length in Case 1 (a), Case 2 (b), Case 3 (c) and Case 4 (d). Refurbished from source [16] to focus on the Ansys results.*

11.4.3   Results: Temperature Load

Case 5

The involute plate is tested under a uniform temperature of $204\,°C$ where the initial temperature was $27\,°C$ in Case 5. In the Cheverton–Kelley experiments, this test is done with the plate mounted on an Invar base. Since the thermal coefficient expansion of Invar is much lower than aluminum's, the base is removed from the setup. The results for Case 5 are shown in Figure 11.18. Ansys Mechanical predicts normal deformations very close to the experimental values, with a maximum absolute difference of $0.02\,mm$.
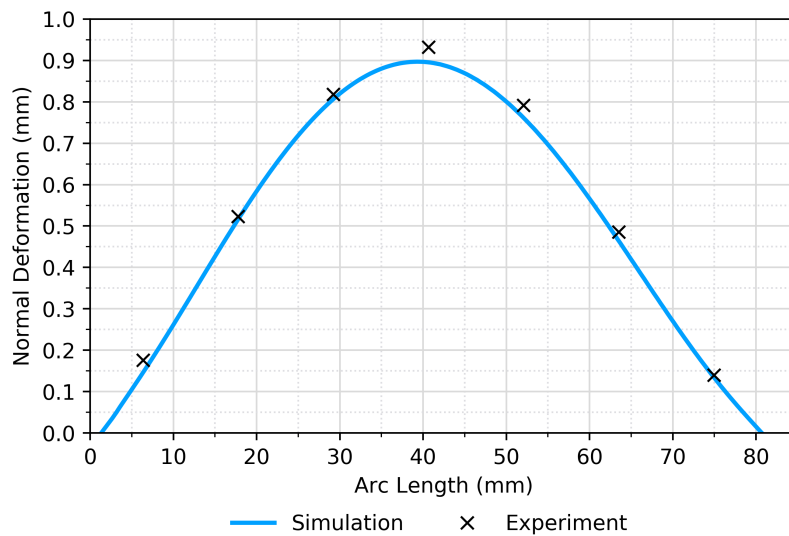
Figure 11.18: *The normal deformation at the plate mid-length calculated by Ansys Mechanical and measured in the experiment for Case 5. Refurbished from source [16] to focus on the Ansys results.*

Case 6

The plate, including the base, was used for the rest of the simulations. Cases 6 and 7 are essentially similar to Case 5, but more complex situations in terms of the presence of the solid base (Case 6) and split base (Case 7) in the setups. A bonded contact is applied between the tabs and the base in both cases. A no-separation contact is applied to the side strips and the base, ultimately limiting the movement in normal direction but allowing small in-plane sliding. The bottom surfaces of the base are constrained in normal direction, and the middle edge of one of the end plates is completely fixed in order to block rigid body motion. The results for Case 6 and Case 7 are shown in Figure 11.19a and Figure 11.19b, respectively. The calculated normal deformations at the plate's mid-length have a maximum deviation of 0.02 mm from the experimental data. The deformations are similar at the end of the plate with a maximum difference of 0.09 mm. Essentially, the deformation shape is well captured by Ansys Mechanical at both the middle and end of the plate.

Case 7

The base was split in Case 7 in order to accommodate for radial expansion of the plate, which leads to smaller deformations of the plate compared to the solid base. This can be seen in Figure 11.19b. The shape of deflections calculated by Ansys Mechanical is similar to the experiment. The maximum calculated normal deformations are about 0.22 mm smaller than the experimental data at the plate mid-length and 0.09 mm smaller at the plate end.
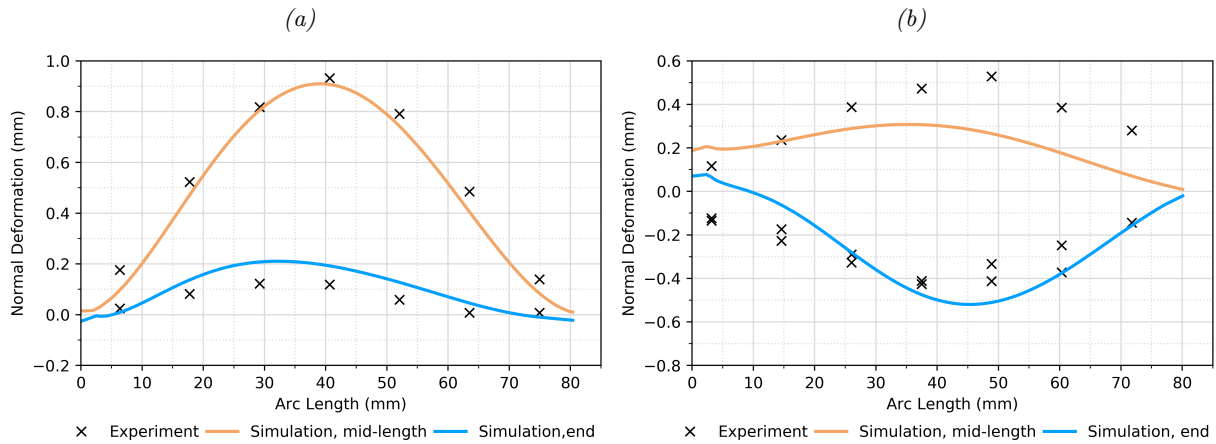
Figure 11.19: *The normal deformation calculated at the plate mid-length for Case 6 (a) and Case 7 (b). Refurbished from source [16] to focus on the Ansys results.*

Case 8

Case 8 comprises the aluminum plate installed in a split carbon steel base. Since carbon steel has a higher thermal expansion coefficient than Invar used in Case 7, the base is expected to deform more than in Case 7, leading to smaller deflections of the aluminum plate. These results are depicted in Figure 11.20 for the mid-length of the plate. Ansys Mechanical is able to reproduce well the maximum deformation behavior at the mid-length of the plate with a maximum difference of 0.03 mm from the experimental data. The situation is slightly different at the end of the plate, where the deflections are underestimated at the smaller arc lengths (left), but accurately captured at higher arc lengths. The deformation shapes differ from the experimental data. Nevertheless, Ansys Mechanical predicts results in good agreement with the experiment, with a maximum difference in maximum deformations of 0.09 mm.
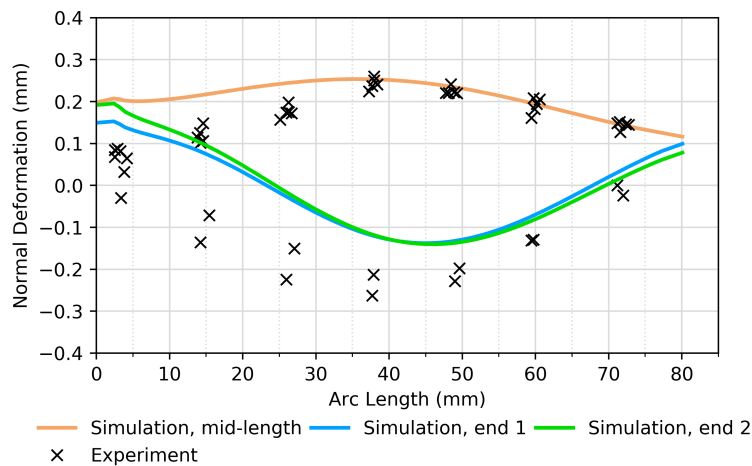

Figure 11.20: *The normal deformation at the plate mid-length calculated by Ansys Mechanical and measured in the experiment for Case 8. Refurbished from source [16] to focus on the Ansys results.*

Case 9

HFIR plates have a 5 cm long unfueled section at each end, which leads to a localized abrupt temperature change. In their experiments, Cheverton and Kelley modeled this feature by replacing 5 cm at each end of the aluminum plate with carbon steel. Since carbon steel has a lower thermal expansion coefficient than aluminum, it would serve to approximate the response of HFIR plate to thermal load. The model uses Invar for the base, and the same boundary conditions described in Case 6 apply. Only the reading from sensor #5 was provided in the CK report [14]. The effect of the carbon steel ends is depicted in Figure 11.21, where the deformation shape has changed compared to a case without carbon steel ends, such as Case 7. The deflections have higher values, especially at the short ends of the plate, due to the presence of cold ends. Figure 11.21 shows the normal deformations at the mid-length. Ansys Mechanical calculates deflections 0.26 mm smaller than the experiment at the mid-length of the plate and roughly 0.38 mm larger deflections at the ends of the plate. This difference in deflections between the simulation and experiment could be attributed to plastic flow. In the report published by Cheverton and Kelley [14], it is mentioned that plastic flow may occur in the plate's aluminum section due to aluminum's higher thermal conductivity.
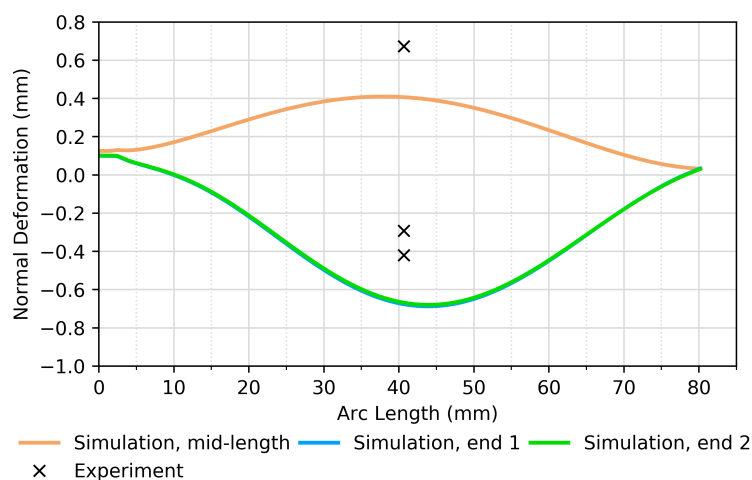
Figure 11.21: *The normal deformation at the plate mid-length calculated by Ansys Mechanical and measured in the experiment for Case 9. Refurbished from source [16] to focus on the Ansys results.*

11.4.4   Results: Pressure and Temperature Loads

An aluminum plate was installed in a solid Monel base in Case 10 and was subjected to temperature and pressure loads. First, the temperature was increased from 27 °C to 204 °C, then the pressure load of 207 kPa was applied. In this case, an additional boundary condition was used; namely, the short ends of the plate were fixed. Figures 11.22a and 11.22b show the normal deformations for the plate under thermal load and pressure plus thermal load, respectively.

Upon thermal load only, the plate mid-length deformation measured in the experiment is roughly 0.46 mm. Upon pressure application, the maximum deflections measured in the experiment

Figure 11.22: *The normal deformation at the plate mid-length for Case 10 without pressure (a) and with pressure (b). Both plots depict results at a temperature of* $204\,°C$*. Refurbished from source [16] to focus on the Ansys results.*

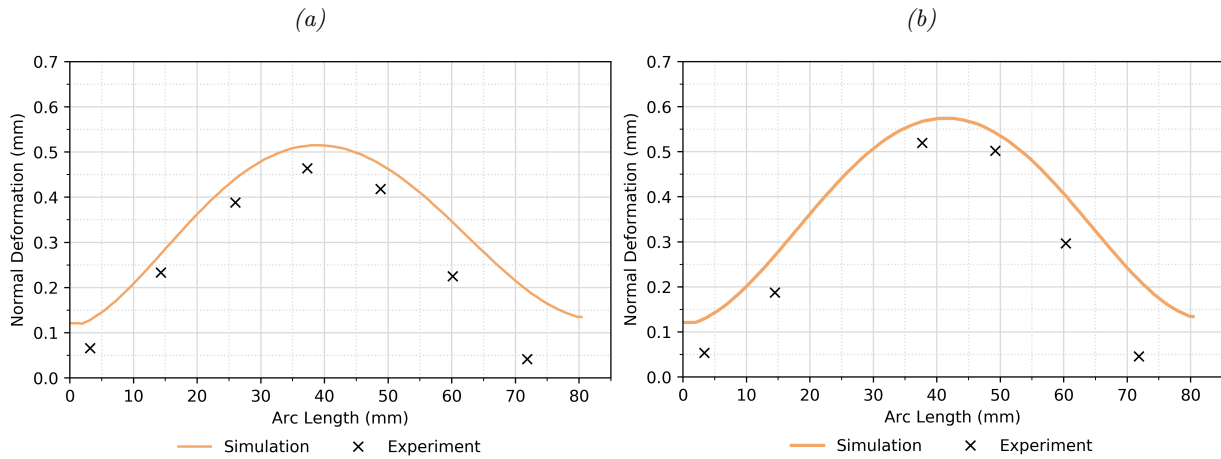increase to $0.52\,\text{mm}$. The deformations calculated by Ansys Mechanical are roughly $0.05\,\text{mm}$ larger than the experimental results for both steps (with and without pressure).

11.4.5 Conclusions

As for the single plate model, it has been found that the plate deflections are reasonably accurate in the cases where only elastic deformation is observed in the experiments, such as Cases 1, 2, 4 and 5. The deflections calculated in these cases are much smaller compared to the coolant channel at HFIR reactor, which has a thickness of $1.27\,\text{mm}$. In order to provide a further understanding of what these values mean to an involute plate shape reactor like HFIR, the deformation of $0.025\,\text{mm}$ (observed in Case 2, load 69 kPa) is very comparable to the oxide layer thickness under Advanced Neutron Source (ANS) thermal-hydraulic conditions [98]. The deformation of $0.025\,\text{mm}$ is about twice as high compared to the oxide layer thickness observed for the current FRM II plate, as reported in [99]. Furthermore, the deflections calculated in the single plate models are smaller overall than $1.27\,\text{mm}$, which corresponds the thickness of the plate. In Case 3, where plastic deformation occurs, the magnitude of the deformation could not be replicated with the linear elastic material models.

The plate and base models, such as Case 6 to Case 9, give a good deflection accuracy at the middle of the plate, where the maximum deflection calculated differs by up to $0.38\,\text{mm}$ between the simulation and experiment. The deflection curves at the mid-length of the plate have similar shapes and magnitudes. The end deformations are more susceptible to differences in modeling the interaction between the plate and the base, leading to larger differences in deflections. The average offset between the experiment and computational results considering all the cases is below 30%, which is completely justified and expected considering that a crucial part of the modeling, such as the CAD model was done based on a few drawings and assumptions. Furthermore, the experimental imperfections such as the reported non-ideal initial shape of the plate in the tests or the possible oversimplification in the modeling approach, may have an influence.

Additionally, an important point to mention is that even though Cheverton and Kelley's experiments measured rather large deformations compared to the channel thickness of an involute reactor (almost 50 % in the case of FRM II), these experiments aimed to evaluate the plate's buckling trend under non-standard operating conditions. Thus, it can be concluded that Ansys Mechanical is able to express the plate behavior in different scenarios, the non-conventional ones included. The code-to-code comparison also shows a good agreement. The interested reader can refer to [16] for more details.

The first goal of calculating the Cheverton-Kelley experiments by using CSM codes such as Ansys Mechanical, Comsol and Star-CCM+ is to validate and verify these codes against experimental data and each other. Secondly, and more importantly, the objective of these calculations is to be able to use these codes for prediction purposes for other rector-related scenarios in the near future such as the LEU conversion scenarios. This successful V&V leads the way to use these codes as prediction tools. Therefore, the overall modeling results of the Cheverton-Kelley experiments have substantial predictive capabilities.

CHAPTER 12

Neutronic – Hydraulics Coupling Results

Based on the verification and validation of Ansys CFX (CFX) using the Gambill–Bundy experiments in Chapter 11.3, CFX is used further for the calculation of the thermal-hydraulic parameters of the current Highly-Enriched Uranium (HEU) core and the potential Low Enriched Uranium (LEU) core. All calculations are performed under nominal conditions at beginning of life (BOL). Serpent 2-CFX coupling for the HEU core is verified by using the previously performed coupling between MCNP and CFX as a verification source. The small differences observed between the two different coupling frameworks are related to the fact that these studies are performed at different times, roughly 10 years apart. The capabilities of modeling approaches have expanded significantly in the past years. Therefore, the differences between the MCNP-CFX and Serpent 2-CFX coupling can be attributed to newer code versions being available at present.

The thermal-hydraulic behavior of a potential LEU core is assessed and based on these calculations, the LEU core is deemed scientifically feasible. The results for the current HEU core, a scientifically possible LEU core, as well as the comparison of fundamental thermal-hydraulic quantities between the two cores are not included in the public version of this thesis. The rationale for this is based on the sensitive nature of the results and their role for the FRM II conversion and licensing process.

CHAPTER 13

Thermal-Fluid-Structure Interaction (TFSI) Coupling Results

In this chapter, the results obtained with the sequential and direct Thermal-Fluid-Structure Interaction (TFSI) coupling for the current Highly-Enriched Uranium (HEU) core and the potential Low Enriched Uranium (LEU) core are discussed. First, the sequential coupling results is performed. Then, the direct coupling and a comparison between the two different couplings is carried out.

All calculations are performed under nominal conditions at beginning of life (BOL). Similarity is observed for the deformation magnitudes calculated for the HEU and LEU plates, which means that the potential LEU core will not present larger deformations than the current one. Additionally, the plate deformations obtained by the sequential and direct couplings are comparable to each other. This indicates the deformations undergone by the plate under nominal conditions do not affect the coolant flow and vice-versa. Therefore, under such conditions, the sequential coupling is sufficient in capturing the physics at play. Additionally, the influence of the combs on the plate's deformation is assessed. It is concluded that the combs do not play a significant role in the deformations; however, this is not a complete conclusion, since further calculations including vibration studies are needed to fully evaluate the combs' importance on the plate's mechanical stability.

The detailed TFSI results are not included in the public version of this dissertation, as they contain sensitive information to the reactor safety and thus cannot be publicly available.

CHAPTER 14

Station Blackout Scenario

In this chapter, the previously settled couplings in Chapter 12 and Chapter 13, are used to assess the plate's behavior under an incident scenario, which is a station blackout leading to failure of primary pumps and reactor SCRAM[1].

The station blackout, followed by the reactor SCRAM is assessed in a time-dependent simulation for the current Highly-Enriched Uranium (HEU) plate. The mass flow and the power were simultaneously decreased for 200 s after the pump failure detection. The resulting pressure, temperature, heat flux and plate deformations are shown. Based on these results, it is concluded that, no pulsating boiling will occur at the plate vicinity, since the calculated heat fluxes are below the measured critical heat flux shown in the licensing reports of Forschungs-Neutronenquelle Heinz Maier-Leibnitz (FRM II) [101–103]. However, to fully assess the failure of primary pumps scenario, the simulation would have to include both fluid and vapor phases, which was not possible at the present time frame of this work. Assuming that pulsating pressures do occur at the plate surface, their influence on the plate mechanical stability is assessed in a separate calculation. Based on the obtained deformations and stress values, the pulsating pressure of 0.8 bar does not impair the plates mechanical integrity.

The detailed results concerning this chapter are not included in the public version of this dissertation, as they contain sensitive information to the reactor safety and thus cannot be publicly available.

---

[1]SCRAM is a term used internationally for reactor emergency shutdown. The term SCRAM is believed to originate from Enrico Fermi who built the first nuclear reactor (also known as Chicago Pile 1). This reactor had a control rod tied to a rope , and a human standing next to it ready to cut the rope upon command. SCRAM was defined as "Safety Control Rods Activation Mechanism" [100].

Part V

Summary

CHAPTER 15

Summary and Conclusion

The primary objective of this thesis was to develop a coupled system of codes that accounts for the thermal-hydraulic and thermal-mechanic behaviors of the current Forschungs-Neutronenquelle Heinz Maier-Leibnitz (FRM II) Highly-Enriched Uranium (HEU) plate. Furthermore, the application of the coupled system as a prediction tool for a potential Low Enriched Uranium (LEU) core constitutes a complimentary objective, but important nonetheless.

The first step was the verification and validation of Computational Fluid Dynamics (CFD) and Computational Structural Mechanics (CSM) codes by using experimental data collected by researchers in the early 60s during the High-Flux Research Reactor (HFIR) licensing program, Gambill–Bundy and Cheverton–Kelley experiments [13, 14]. Gambill-Bundy experiments aimed at assessing the heat transfer parameters of a heated thin rectangular channel that is representative of HFIR conditions [13]. Cheverton-Kelley experiments were performed to estimate the pressure- and -temperature induced buckling tendencies of the HFIR outer plate [14]. Considering that the concept and design of FRM II originates from High Flux Isotope Reactor (HFIR), these experiments can be used, by extension, to represent the thermal hydraulic and mechanical conditions of FRM II. Consequently, the Gambill–Bundy and Cheverton–Kelley experiments were simulated using Ansys CFX for the thermal-hydraulics (see Chapter 11.3) and Ansys Mechanical for thermal-mechanics (see Chapter 11.4). Furthermore, the obtained results were validated against the experimental data and verified with two other similar codes within the frame work of Involute Working Group (IWG) [15, 16][38][96]. The successful verification and validation (V&V) of the CFD and CSM codes builds credibility in the methods and leads the way to using these codes for prediction purposes in the LEU conversion scenarios.

Further analysis of the current FRM II HEU plate was performed by using a coupling between the neutronic Monte Carlo code Serpent 2 and the previously validated and verified code, Ansys CFX (see Chapter 12). The Serpent 2-Ansys CFX (CFX) coupling was verified by using the FRM II licensing documents and the previously done coupling between MCNP and CFX as verification bases. The results obtained with the Serpent 2-CFX coupling agree well with the

calculated and measured values shown in the licensing reports [5], and the previous work on the HEU plate done with different codes [12]. In the few cases where the results show larger deviations from the verification sources, the differences can be explained based on the different boundary conditions of the system. The boundary conditions used here are justified by data provided by the licensing documents.

The next step consisted of using the newly coupled system between hydraulic and mechanics to calculate deformations and stresses for the current HEU plate. This assessment was performed two-fold: in a sequential thermal-fluid-structure interaction (TFSI) coupling and a direct TFSI coupling (see Chapter 13). The sequential Thermal-Fluid-Structure Interaction (TFSI) coupling implies that the thermal-hydraulic loads calculated by the Serpent 2–CFX coupling are used as boundary conditions for the simulation performed in Ansys Mechanical, the goal of which is determining the influence of temperature and pressure on the plate deformation. In contrast, the direct TFSI coupling relies on continuous exchange of information between CFX and Ansys Mechanical, i.e. the deformation caused by thermal expansion in the plate in Ansys Mechanical is transferred to CFX where the deformation's effect on the velocity is calculated. Consecutively, the modified flow field variables such as pressure are sent back to Ansys Mechanical. This loop continues based on the convergence criteria. Both coupling approaches are applied to the HEU plate. The deformations obtained with the sequential and direct couplings agree well with each other with a maximum deviation of $10\,\mu m$, which is an indication that the deformations undergone by the plate are small, and therefore, do not have an impact on the flow field.

An additional point of interest was the assessment of the combs' influence on the thermal-hydraulic and mechanical parameters. It is seen that the bottom comb plays a modest role in the heat transfer parameters of the HEU plate in the sense that it creates turbulence that aids the convective heat transfer. From a mechanical deformation point of view, it appears that the role of the comb is minor. However, these calculations are not conclusive in this regard as additional calculations assessing the combs influence on the plate vibrations are necessary (see Section 15.1.)

The above-mentioned Serpent 2-CFX coupling and thermal-fluid-structure interaction (TFSI) couplings are used to assess and predict the thermal-hydraulic and thermal-mechanic behavior of a potential LEU core design for the conversion of FRM II. A potential LEU core design is briefly described in Chapter 1.3. It is crucial to point out that the potential LEU core discussed in this work originates from an extensive down-selection process, the details of which are described in [3]. A comparison is made between the two cores in terms of velocities, pressure, heat fluxes and temperatures. Some of the geometrical and material differences between the current HEU and potential LEU plate are responsible for the differences in velocities, pressure and temperatures. However, these differences are understood and justified. Therefore, the potential LEU core appears scientifically feasible.

Finally, in Chapter 14, the successfully developed coupled system was used to assess the station blackout scenario for the current FRM II HEU core in which all the primary pumps fail and the

core is scrammed. The results indicate that no pulsating boiling will occur as the calculated heat flux is smaller than the experimentally determined critical heat flux which sets the limit for the onset of pulsating boiling. Furthermore, assuming that pulsated boiling does occur, the influence of the pulsating pressure on the plate's mechanical integrity is determined to be minor.

15.1 Outlook

The road to the conversion of FRM II to LEU has many aspects to be considered. Further work is expected to include an optimized LEU core and a detailed assessment of the mechanical aspects such as stresses and vibrations undergone by the LEU plate. Furthermore, special attention will be paid to the multiphase flow analysis of the coolant. Such calculations are expected to include thermal phase change of the water into vapor by using boiling models in CFX.

15.2 Conclusion

The developed coupling between Serpent 2, Ansys CFX and Ansys Mechanical is a state-of-the-art solution that can be used for the FRM II conversion program for the years to come. This coupling includes commercial codes that are widely used not only in the nuclear community, but also in broader research topics including turbulence and multiphase modeling. It is thereupon believed that these couplings will facilitate the conversion program of FRM II by shedding light into the many aspects that the LEU conversion encompasses.

Part VI

Appendix

Velocity Profile Calculations Using the Sieve

A top view of the sieve that is located upstream of the fuel element in the central channel is shown in Figure A.1. To obtain a developed velocity profile for the inlet boundary condition of the fuel plate, a calculation of the sieve is required. Since the sieve has a repetitive structure, a quarter of it together with the surrounding water domain was modeled in *SolidWorks* and then meshed. A picture of the computer-aided design (CAD) model from *SolidWorks* and the corresponding mesh are shown in Figure A.2. A more detailed view of the mesh is shown in Figure A.3
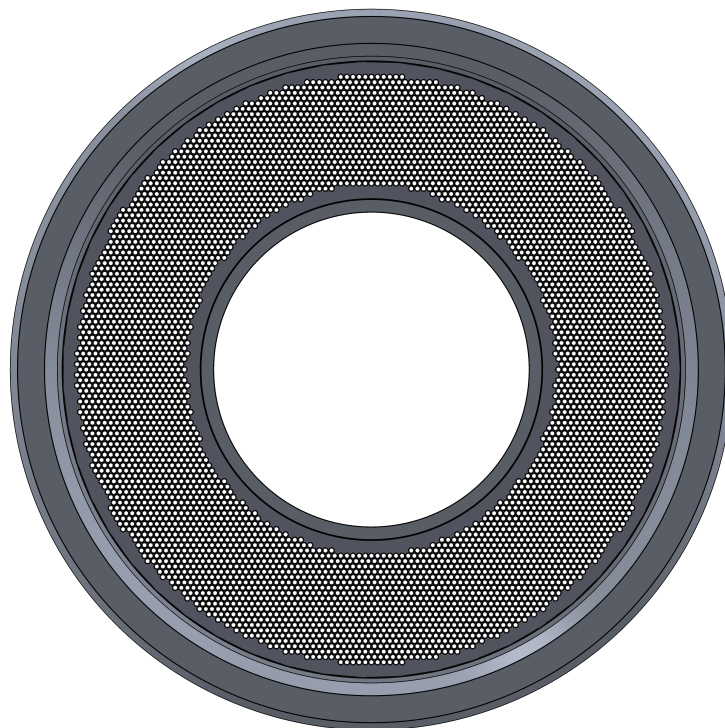
Figure A.1: *Top view of the sieve that is located upstream of the fuel element.*

Since no heat is present upstream of the central channel, the calculation is isothermal with a stable temperature of $37\,^\circ\text{C}$. The boundary conditions include an inlet mass flow of $68.625\,\text{kg}\,\text{s}^{-1}$, which correspond to a fourth of the total mass flow. The static pressure of $7.5\,\text{bar}$ which is the calculated pressure for the inlet of the fuel plate was set as the outlet boundary condition.
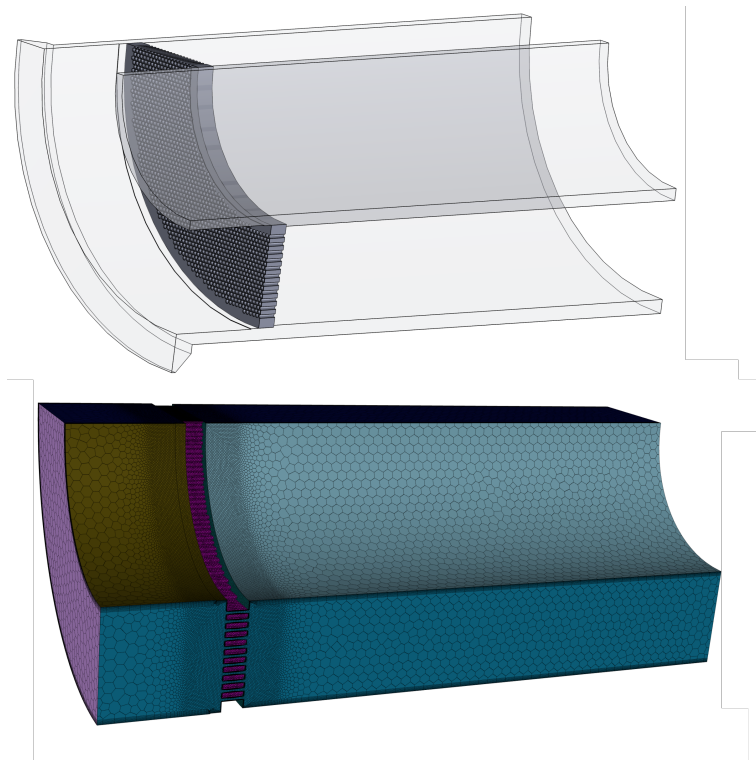
Figure A.2: *CAD model and mesh of a quarter of the sieve are shown at the top and bottom of the figure, respectively.*
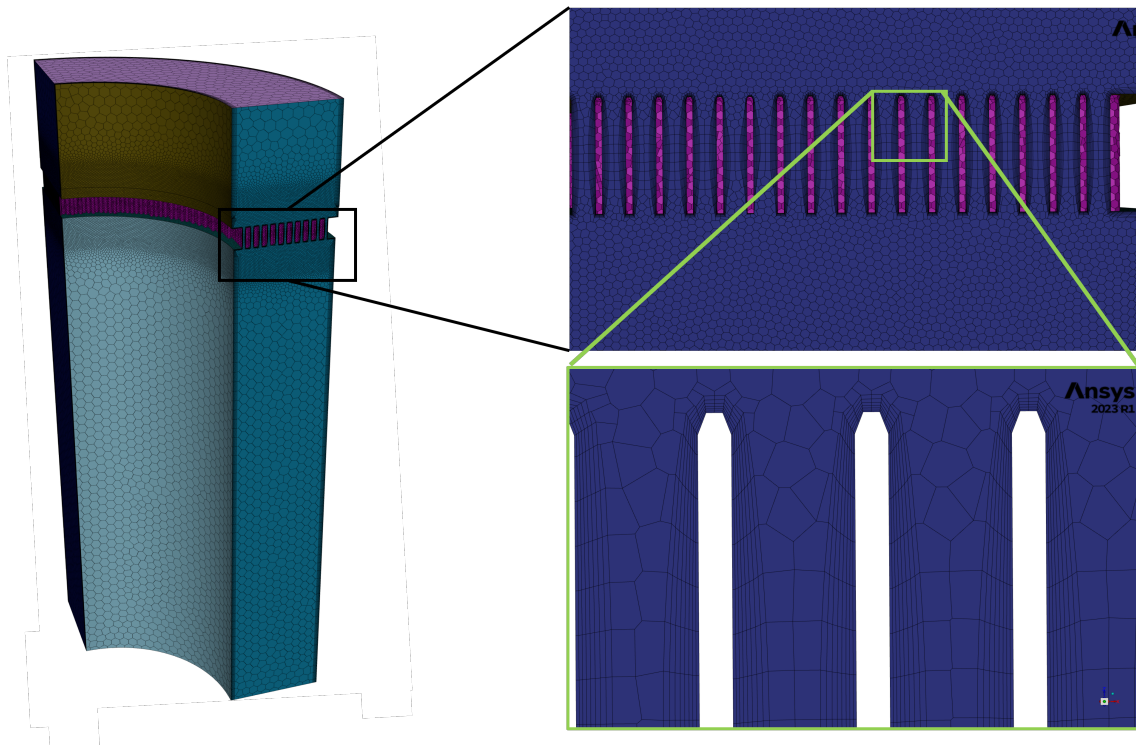
Figure A.3: *A more detailed mesh of the sieve and the surrounding water domain is shown.*

Temperature Dependent Material Properties

The specific heat capacity of U_3Si_2, aluminum and fuel is shown in Figure A.4 according to the formulas stated in [82].

Figure A.4: *Temperature dependent specific heat capacity for U_3Si_2, aluminum and fuel.*

Material Properties Sensitivity

To analyze more closely the influence of the material properties on the deformations in the Highly-Enriched Uranium (HEU) plate, the statistical uncertainty on the material properties measured by the Impulse Excitation Technique in Chapter 9.1.6 is used. You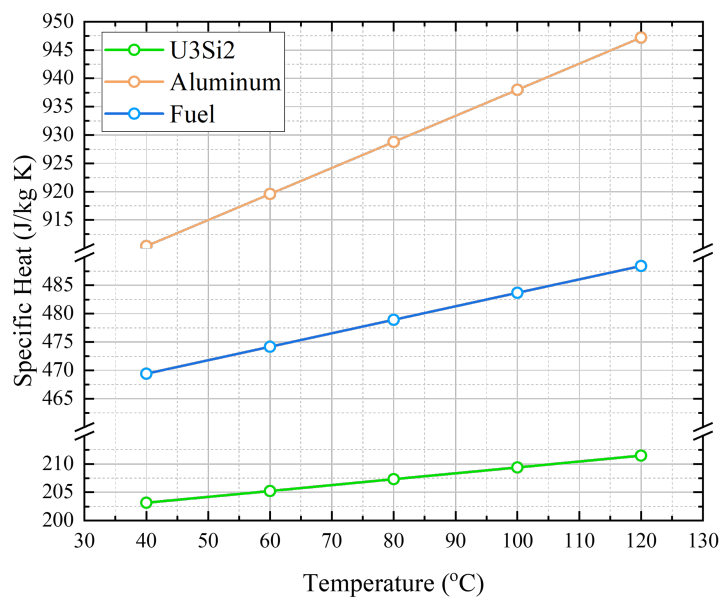ng's modulus is varied within the statistical uncertainty while keeping a constant Poisson ratio of 0.3. Then, different values of the Poisson ratio are used to determine its influence on the maximum total deformation. The results are shown in Figure A.5.

As expected, an increase in Poisson's ratio leads to an increase in the deformation, while a decrease in the elasticity modulus decreases the deformation.
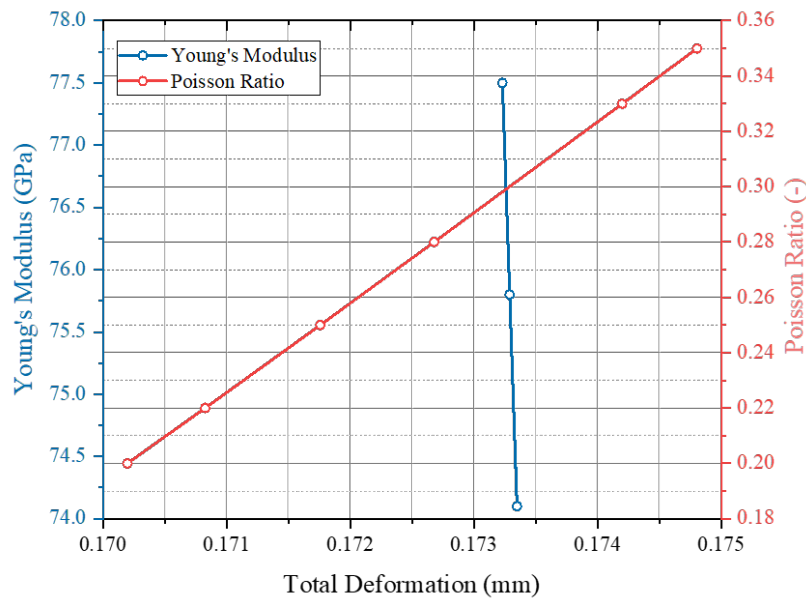
Figure A.5: *Dependence of the maximum total deformation upon Young's modulus and Poisson's ratio.*

The deformation results differ by 0.034 % from Young's modulus value used in the calculations. Applying Poisson's ratio range of 0.2-0.35 spreads the deformation values by a maximum of 1.78 %. Therefore, it is concluded that the statistical uncertainty of the material properties is entirely negligible. Furthermore, the independence of the deformation on Poisson's ratio assures that keeping a constant value for Poisson's ratio in the Impulse Excitation Technique (IET) formulas is Chapter 8 is a well-founded assumption.

List of Abbreviations

FRM II Forschungs-Neutronenquelle Heinz Maier-Leibnitz

TUM Technische Universität München

ORNL Oak Ridge National Laboratory

Argonne Argonne National Laboratory

ILL Institute Laue Langevin

HFIR High Flux Isotope Reactor

RHF High Flux Reactor

CAD computer-aided design

CFD Computational Fluid Dynamics

CSM Computational Structural Mechanics

CFX Ansys CFX

RANS Reynolds-Averaged Navier-Stokes

HEU Highly-Enriched Uranium

LEU Low Enriched Uranium

ONB Onset of Nucleate Boiling

DNB Departure from Nucleate Boiling

CHF Critical Heat Flux

SST Shear Stress Transport

RS Reynold Stress

IWG Involute Working Group

1D one-dimensional

FSI Fluid-Structure Interaction

GUI Graphical User Interface

PDE Partial Differential Equation

Re Reynolds number

Nu Nusselt number

Pr Prandtl number

3D three-dimensional

FEM Finite Element Method

FVM Finite Volume Method

FDM Finite Difference Method

IET Impulse Excitation Technique

TFSI Thermal-Fluid-Structure Interaction

IAEA International Atomic Energy Agency

List of Symbols

Symbol	Unit	Meaning
a	$\mathrm{m\,s^{-2}}$	thermal diffusivity
A	$\mathrm{cm^2}$	area
ΔB	-	modification of wall functions for rough walls
C	varying	used for constants
c_p	$\mathrm{J\,kg^{-1}\,K^{-1}}$	specific heat capacity at constant pressure
d_h	m	hydraulic diameter
d_M	m	momentum boundary layer
d_T	m	thermal boundary layer
D	Pa	elasticity matrix
D	$\mathrm{W\,m\,K^{-1}}$	thermal conductivity matrix
e	$\mathrm{m^2\,s^{-2}}$	internal energy per unit mass
E	J	energy
E	Pa	Young's modulus
F	N	force
G	Pa	bulk modulus
h	$\mathrm{W\,m^{-2}\,K^{-1}}$	heat transfer coefficient
h	mm	sand grain roughness
I	%	turbulence intensity
k	$\mathrm{W\,m\,K^{-1}}$	thermal conductivity
K	$\mathrm{m^2\,s^{-2}}$	turbulence kinetic energy per unit mass
K	$\mathrm{N\,m^{-1}}$	stiffness matrix
$\boldsymbol{n}$	-	normal vector
Nu	-	Nusselt number
p	Pa or bar	pressure
Pr	-	Prandtl number
Q	$\mathrm{J\,m^{-1}\,s^{-3}}$	energy per unit volume and unit time
q	$\mathrm{W\,cm^{-2}}$	heat flux
$\ddot{q}$	$\mathrm{W\,cm^{-1}}$	heat generation rate per unit volume
Re	-	Reynolds number
T	°C	temperature
T^+	-	dimensionless temperature
t	s	time
u^+	-	dimensionless velocity
u_τ	$\mathrm{m\,s^{-1}}$	shear or friction velocity

u^*	-	dimensionless velocity (updated scale for scalable wall functions)
u	m	displacement
v	$\mathrm{m\,s^{-1}}$	velocity
V	cm	volume
W	J	work
y^+	-	dimensionless wall distance
y^*	-	dimensionless wall distance (updated scale for scalable wall functions)
α	$\mathrm{K^{-1}}$	Secant coefficient of thermal expansion
ϵ	$\mathrm{mm\,mm^{-1}}$	strain
ϵ	$\mathrm{m^2\,s^{-1}}$	turbulence dissipation rate
κ	-	von Karman constant
λ	$\mathrm{Pa\,s}$	bulk viscosity
μ	$\mathrm{Pa\,s}$	dynamic viscosity
μ_t	$\mathrm{Pa\,s}$	turbulence viscosity
ν	$\mathrm{m\,s^{-2}}$	kinematic viscosity
ν	$\mathrm{m\,s^{-2}}$	momentum diffusivity
ν	-	Poisson's ratio
ω	$\mathrm{s^{-1}}$	turbulence frequency
ρ	$\mathrm{kg\,m^{-1}}$	density
$\boldsymbol{\sigma}$	Pa	stress tensor
$\boldsymbol{\tau}$	Pa	viscous stress tensor
τ_w	$\mathrm{Pa\,s}$	wall shear stress

Bibliography

[1] Forschungs-Neutronenquelle Heinz Maier-Leibnitz. *Neutron Source*. URL: https://www.frm2.tum.de/en/frm2/the-neutron-source/reactor/.

[2] C. Reiter. "Model system for transient calculations for research reactors with a compact core". Dissertation. Technical University of Munich, April 2019. URL: http://mediatum.ub.tum.de/node?id=1506848.

[3] C. Reiter, A. Bergeron, D. Bonete-Wiese, M. Kirst, J. Mercz, R. Schönecker, K. Shehu, B. Ozar, F. Puig, J. Licht, W. Petry, and P. Müller-Buschbaum. "A Low-Enriched Uranium (LEU) option for the conversion of FRM II". In: *Annals of Nuclear Energy* 183 (2023), p. 109599. ISSN: 03064549. DOI: 10.1016/j.anucene.2022.109599. URL: 10.1016/j.anucene.2022.109599.

[4] Forschungs-Neutronenquelle Heinz Maier-Leibnitz. *FRM II Conversion*. URL: https://www.frm2.tum.de/en/frm2/the-neutron-source/conversion/.

[5] Gysler, Sperber, and Ehrich. *Thermahydraulische Kernauslegung FRM II: A1C-1301735-1*.

[6] A. Bergeron, C. Bojanowski, J. Licht, K. Shehu, C. Reiter, F. Thomas, Y. Calzavara, P. K. Jain, and D. Chandler. "Involute Working Group (IWG) Progress Towards Validation of CFD for Involute-Plate Reactors Safety Analysis". In: *International Meeting on Reduced Enrichment for Research Test Reactors (RERTR)*.

[7] C. Steyer. "Plasma- und festkoerperphysikalische Optimierung eines Beschichtungsverfahrens fuer monolithische UMo-Kernbrennstoffe". Dissertation. Technical University of Munich, 2019. URL: https://mediatum.ub.tum.de/doc/1506848/document.pdf.

[8] C. Miller, B. Durtschi, J. I. Cole, and K. Daum. *U-10Mo Monolithic Fuel Qualification Plan*. 2021. URL: https://www.osti.gov/biblio/1781336.

[9] L. Jamison, J. Stillman, D. Jaluvka, W. Mohamed, Y. Kim, and E. Wilson. *Review of the Technical Basis for Properties and Fuel Performance Data Used in HEU to LEU Conversion Analysis for U-10Mo Monolithic Alloy Fuel*. DOI: 10.2172/1663207. URL: https://www.osti.gov/biblio/1663207.

[10] C. Reiter, M. Kirst, K. Shehu, D. Bonete-Wiese, R. Schoenecker, A. Bergeron, F. Puig, and B. Ozar. *Modelling of the FRM II - Validation and Verification of the Models and Methods*. Unpublished confidential TUM document, 2022.

[11] K. Faust. "Serpent 2 and OpenFOAM Models for Coupled Calculations of Research Reactors with a Compact Core". Master Thesis. FRM II: Technical University of Munich, June 2019.

[12] H. Breitkreutz. "Coupled Neutronics and Thermal Hydraulics of High Density Cores for FRM II". Dissertation. Technical University of Munich, February 2011. URL: http://mediatum.ub.tum.de/node?id=1070613.

[13] W. R. Gambill and R. D. Bundy. "HFIR heat transfer studies of turbulent water flow in thin rectangular channels". In: *OSTI* (). DOI: 10.2172/4033513. URL: https://www.osti.gov/biblio/4033513-hfir-heat-transfer-studies-turbulent-water-flow-thin-rectangular-channels.

[14] R. D. Cheverton and W. H. Kelley. *Experimental Investigation of HFIR Fuel Plate Deflections Induced by Temperature and Pressure Differentials*. DOI: 10.2172/4817701.

[15] K. Shehu, C. Bojanowski, A. Bergeron, W. Petry, and C. Reiter. "First Steps to Coupled Hydraulic and Mechanical Calculations within a Parameter Study to Define Possible Core Designs for the Conversion of FRM II". In: *EPJ Web of Conferences* 247 (2021), p. 08011. ISSN: 2100-014X. DOI: 10.1051/epjconf/202124708011.

[16] M. Sitek, K. Shehu, P. K. Jain, A. Bergeron, J. Licht, C. Reiter, M. Sitek, A. Bergeron, and J. Licht. "Thermomechanical Analysis and Modeling of Involute-Shaped Fuel Plates Using the Cheverton–Kelley Experiments for the High Flux Isotope Reactor". In: *Nuclear Engineering and Design* 409 (2023), p. 112334. DOI: 10.1016/j.nucengdes.2023.112334.

[17] A. Bejan and A. D. Kraus. *Heat transfer handbook*. Hoboken, N.J. and Chichester: Wiley, 2003. ISBN: 0-471-39015-1.

[18] F. P. Incropera. *Fundamentals of heat and mass transfer*. 6th ed. Hoboken, N.J.: Wiley and Chichester, 2007. ISBN: 978-0-471-45728-2.

[19] H. Schlichting. *Boundary-Layer Theory*. Springer Berlin Heidelberg, 2000. ISBN: 978-3-642-85831-4.

[20] M. David, A. Toutant, and F. Bataille. "Numerical development of heat transfer correlation in asymmetrically heated turbulent channel flow". In: *International Journal of Heat and Mass Transfer* 164 (2021), p. 120599. ISSN: 0017-9310. DOI: 10.1016/j.ijheatmasstransfer.2020.120599.

[21] E. N. Sieder and G. E. Tate. "Heat Transfer and Pressure Drop of Liquids in Tubes". In: *Industrial & Engineering Chemistry* 28.12 (1936), pp. 1429–1435. ISSN: 0019-7866. DOI: 10.1021/ie50324a027.

[22] H. Hausen. "Wärmeübertragung im Gegenstrom, Gleichstrom und Kreuzstrom". In: *ZAMM - Journal of Applied Mathematics and Mechanics / Zeitschrift für Angewandte Mathematik und Mechanik* 59.4 (1979), p. 213. ISSN: 1521-4001. DOI: 10.1002/zamm.19790590411.

[23] Y. S. Kim, H. T. Chae, S. van den Berghe, A. Leenaers, V. Kuzminov, and A. M. Yacout. "Aluminum cladding oxide growth prediction for high flux research reactors". In: *Journal of Nuclear Materials* 529 (2020), p. 151926. ISSN: 00223115. DOI: `10.1016/j.jnucmat.2019.151926`.

[24] G. H. Yeoh, J. Y. Tu, and Y. Li. "Numerical investigation of static flow instability in a low-pressure subcooled boiling channel". In: *Heat and Mass Transfer* 40.5 (2004), pp. 355–364. ISSN: 0947-7411. URL: `https://www.academia.edu/14277079/Numerical_investigation_of_static_flow_instability_in_a_low_pressure_subcooled_boiling_channel`.

[25] A. Faghri and Y. Zhang. *Fundamentals of multiphase heat transfer and flow*. Cham, Switzerland: Springer, 2020. ISBN: 978-3-030-22136-2.

[26] T. Schlitt. "Proof of concept for a thermohydraulic loop: Validation of simulation tools". Master Thesis. Technical University of Munich, October 2021.

[27] J. Blazek. *Computational fluid dynamics: Principles and applications*. Third edition. Amsterdam: Butterworth-Heinemann, 2015. ISBN: 9780080999951.

[28] L. G. Leal. *Advanced transport phenomena: Fluid mechanics and convective transport processes*. Cambridge series in chemical engineering. Cambridge and New York: Cambridge University Press, 2007. ISBN: 0511296479.

[29] H. Oertel. *Prandtl's essentials of fluid mechanics*. 2nd. Vol. 158. Applied mathematical sciences. New York: Springer, 2004. ISBN: 0387404376. URL: `http://www.springer.com/gb/`.

[30] *Navier–Stokes Equation | Clay Mathematics Institute*. URL: `https://www.claymath.org/millennium-problems/navier%E2%80%93stokes-equation`.

[31] "IV. On the dynamical theory of incompressible viscous fluids and the determination of the criterion". In: *Philosophical Transactions of the Royal Society of London. (A.)* 186 (1895), pp. 123–164. ISSN: 0264-3820. DOI: `10.1098/rsta.1895.0004`.

[32] J. Boussinesq. *Essai Sur La Théorie Des Eaux Courantes*. Paris, 1877.

[33] Online Document. *All there is to know about different mesh types in CFD!* 2016. URL: `https://www.manchestercfd.co.uk/post/all-there-is-to-know-about-different-mesh-types-in-cfd`.

[34] T. von Kármán. *Aerodynamics: Selected topics in the light of their historical development*. Mineola N.Y.: Dover Publications, 2004. ISBN: 978-0-486-43485-8.

[35] Ansys. *Ansys CFX Solver Theory Guide. Release 2022.R2*. Ed. by Ansys User Guide.

[36] W. M. Kays. "Turbulent Prandtl Number—Where Are We?" In: *Journal of Heat Transfer* 116.2 (1994), pp. 284–295. ISSN: 0022-1481. DOI: `10.1115/1.2911398`.

[37] B. E. Launder and D. B. Spalding. "The numerical computation of turbulent flows". In: *Computer Methods in Applied Mechanics and Engineering* 3.2 (1974), pp. 269–289. ISSN: 00457825. DOI: `10.1016/0045-7825(74)90029-2`.

[38] C. Bojanowski, A. Bergeron, and J. Licht. "Involute Working Group – Validation of CFD Turbulence Models for Steady-State Safety Analysis". In: *OSTI* ANL/RTR/TM-19/5 (). DOI: `10.2172/1615151`. URL: `https://www.osti.gov/biblio/1615151-involute-working-group-validation-cfd-turbulence-models-steady-state-safety-analysis`.

[39] M. F. Lechner R. *Development of a rough wall boundary condition for omega-based turbulence models.*

[40] L. D. Landau. *Course of theoretical physics. Vol 6, Fluid mechanics.* 2nd. Oxford: Pergamon, 1987. ISBN: 0080339336.

[41] L. Prandtl. *Abriss der Lehre von der Flüssigkeits- und Gasbewegung.* Fischer, G., 1913. URL: `https://www.deutsche-digitale-bibliothek.de/%20item/ITH27KERU2XUIHJH ZAFTGZCBBAWBYIKQ`.

[42] A. N. Kolmogorov. "Die Lokale Struktur der Turbulenz in einer inkompressiblen zähen Flüssigkeit bei sehr großen Reynolds Zahlen". In: *Dokl. Akad. Wiss. USSR* 30 (1941), pp. 301–305.

[43] S. B. Pope. *Turbulent flows.* Cambridge: Cambridge University Press, 2000. ISBN: 0521591252.

[44] L. F. Richardson. "The supply of energy from and to atmospheric eddies". In: *Proceedings of the Royal Society of London. Series A, Containing Papers of a Mathematical and Physical Character* 97.686 (1920), pp. 354–373. ISSN: 0950-1207. DOI: `10.1098/rspa.1920.0039`.

[45] *Simulation and modeling of turbulent flows.* ICASE/LaRC series in computational science and engineering. New York: Oxford University Press, 2020. ISBN: 9780197561003.

[46] J. SMAGORINSKY. "General Circulation Experiments with the Primitive Equations". In: *Monthly Weather Review* 91.3 (1963), pp. 99–164. ISSN: 0027-0644. DOI: `10.1175/1520-0493(1963)091{\textless}0099:GCEWTP{\textgreater}2.3.CO;2`. URL: `https://journals.ametsoc.org/downloadpdf/journals/mwre/91/3/1520-0493_1963_091_0099_gcewtp_2_3_co_2.pdf`.

[47] L. S. Hedges, A. K. Travin, and P. R. Spalart. "Detached-Eddy Simulations Over a Simplified Landing Gear". In: *Journal of Fluids Engineering* 124.2 (2002), pp. 413–423. ISSN: 0098-2202. DOI: `10.1115/1.1471532`.

[48] H. K. Versteeg and W. Malalasekera. *An introduction to computational fluid dynamics: The finite volume method / H.K. Versteeg and W. Malalasekera.* 2nd ed. Harlow, Essex: Pearson Education, 2007. ISBN: 9780131274983.

[49] D. C. Wilcox. "Multiscale model for turbulent flows". In: *AIAA Journal* 26.11 (1988), pp. 1311–1320. ISSN: 0001-1452. DOI: `10.2514/3.10042`.

[50] T. Esch and F. R. Menter. "Heat Transfer Predictions Based on Two-Equation Turbulence Models with Advanced Wall Treatment". In: *Turbulence, heat and mass transfer*. Ed. by K. Hanjalić, Y. Nagano, and M. J. Tummers. Turbulence heat and mass transfer. New York and Wallingford: Begell House, 2003, pp. 633–640. ISBN: 1567001963.

[51] B. Launder. "Second-moment closure: present and future". In: *International Journal of Heat and Fluid Flow* (1989), pp. 282–300. ISSN: 0142727X. URL: https://www.semanti cscholar.org/paper/Second-moment-closure%3A-present%E2%80%A6-and-future-Launder/e0fd9836c3f206e05ed87003769418111175bafd.

[52] W.J. Raw. "Robustness of Coupled Algebraic Multigrid for the Navier-Stokes Equations". In: *AIAA 96-0297, 34th Aerospace and Sciences Meeting & Exhibit* (1996).

[53] I. H. Shames and C. L. Dym. *Energy and finite element methods in structural mechanics: SI units edition*. New York, NY: Taylor & Francis, 2003. ISBN: 9780203757567. DOI: 10.1201/9780203757567.

[54] K.-J. Bathe. *Finite element procedures in engineering analysis*. Englewood Cliffs: Prentice Hall and London : Prentice-Hall International, 1996. ISBN: 0133014584.

[55] G. Dhatt, G. Touzot, and E. Lefrançois. *Finite element method*. Numerical methods series. London: ISTE, 2012. ISBN: 978-1-84821-368-5.

[56] Ansys. *Ansys Mechanical APDL Theory Reference 2022.R2*.

[57] R. v. Mises. "Mechanik der festen Körper im plastisch- deformablen Zustand". In: *Nachrichten von der Gesellschaft der Wissenschaften zu Göttingen, Mathematisch-Physikalische Klasse* 1913 (1913), pp. 582–592. URL: https://eudml.org/doc/58894.

[58] T. H. Courtney. *Mechanical behavior of materials*. 2nd ed. Long Grove, Illinois: Waveland, 2000. ISBN: 9781577664253.

[59] A. Gil, J. Segura, and N. M. Temme. *Numerical methods for special functions*. Philadelphia, Pa.: Society for Industrial & Applied Mathematics and Cambridge, 2007. ISBN: 978-0-89871-634-4.

[60] M. J. Turner, R. W. Clough, H. C. Martin, and L. J. Topp. "Stiffness and Deflection Analysis of Complex Structures". In: *Journal of the Aeronautical Sciences* 23.9 (1956), pp. 805–823. DOI: 10.2514/8.3664.

[61] A. Ern and J.-L. Guermond. *Theory and practice of finite elements*. New York: Springer, 2004. ISBN: 0-387-20574-8.

[62] Internet Document. *Basic FEA Theory – Part 1 – Principle of Virtual Work*. 8/2/2022. URL: https://polymerfem.com/basic-fea-theory-part-1-principle-of-virtual-work/.

[63] F. B. Hildebrand. *Introduction to numerical analysis*. 2d ed. International series in pure and applied mathematics. New York: McGraw-Hill, 1973, 1974. ISBN: 0070287619.

[64] J. C. Simo and M. S. Rifai. "A class of mixed assumed strain methods and the method of incompatible modes". In: *International Journal for Numerical Methods in Engineering* 29.8 (1990), pp. 1595–1638. ISSN: 0029-5981. DOI: 10.1002/nme.1620290802. URL: https://onlinelibrary-wiley-com.eaccess.ub.tum.de/doi/10.1002/nme.1620290802.

[65] J. C. Simo and F. Armero. "Geometrically non-linear enhanced strain mixed methods and the method of incompatible modes". In: *International Journal for Numerical Methods in Engineering* 33.7 (1992), pp. 1413–1449. ISSN: 0029-5981. DOI: 10.1002/nme.1620330705. URL: https://onlinelibrary-wiley-com.eaccess.ub.tum.de/doi/10.1002/nme.1620330705.

[66] A. Georqe, J. W.-H. Liu: "Computer Solution of Large Sparse Positive Definite Systems". In: *Biometrical Journal* 26.2 (1984), p. 218. ISSN: 03233847. DOI: 10.1002/bimj.4710260217.

[67] *Ansys CFX Fluid Structure Interaction (FSI) with Ansys Mechanical.*

[68] R. Silva. *Direct Coupled Thermal-Structural Analysis in Ansys Workbench.* Brasil, 2013. URL: https://docplayer.net/34689383-Direct-coupled-thermal-structural-analysis-in-ansys-workbench-roberto-silva-esss.html.

[69] W. Voigt. "Ueber die Beziehung zwischen den beiden Elasticitätsconstanten isotroper Körper". In: *Annalen der Physik* 274.12 (1889), pp. 573–587. ISSN: 1521-3889. DOI: 10.1002/andp.18892741206. URL: https://onlinelibrary.wiley.com/doi/pdf/10.1002/andp.18892741206.

[70] U. Carvajal-Nunez, T. A. Saleh, J. T. White, B. Maiorov, and A. T. Nelson. "Determination of elastic properties of polycrystalline U3Si2 using resonant ultrasound spectroscopy". In: *Journal of Nuclear Materials* 498 (2018), pp. 438–444. ISSN: 00223115. DOI: 10.1016/j.jnucmat.2017.11.008.

[71] *ASM Material Data Sheet.* 1.8.2022. URL: https://asm.matweb.com/search/SpecificMaterial.asp?bassnum=ma6061o.

[72] B. Weiler and C. U. Grosse. "Elastic Constants - Their Dynamic Measurement and Calculation". In: *Otto-Graf-Journal* 6 (1995), pp. 116–131.

[73] *TUM Center for Nuclear Safety and Innovation (CNSI).* URL: https://www.mep.tum.de/cnsi/startseite/.

[74] R. Schönecker. "Development, Verification and Discussion of a PLTEMP Model for Research Reactors with a Compact Core". Master's Thesis. 2020.

[75] Dassault Systèmes. *SOLIDWORKS.* URL: https://www.solidworks.com/de.

[76] CFD Online. *Turbulence Free Stream Boundary Conditions.* URL: https://www.cfd-online.com/Wiki/Turbulence_free-stream_boundary_conditions.

[77] *Turbulence length scale – CFD-Wiki, the free CFD reference.* 6/15/2012. URL: https://www.cfd-online.com/Wiki/Turbulence_length_scale.

[78] Siemens / TUM. *Sicherheitsbericht der Neutronenquelle Muenchen FRM II.* 1993.

[79] W. Wagner, J. R. Cooper, A. Dittmann, J. Kijima, H.-J. Kretzschmar, A. Kruse, R. Mares, K. Oguchi, H. Sato, I. Stöcker, O. Sˇifner, Y. Takaishi, I. Tanishita, J. Trübenbach, and T. Willkommen. "The IAPWS Industrial Formulation 1997 for the Thermodynamic Properties of Water and Steam". In: *Journal of Engineering for Gas Turbines and Power* 122.1 (2000), pp. 150–184. ISSN: 0742-4795. DOI: 10.1115/1.483186.

[80] International Atomic Energy Agency. *Material properties of unirradiated uranium-molybdenum (U-Mo) fuel for research reactors.* Vienna, Austria.

[81] W. R. Martin and J. R. Weir. *Mechanical properties of X8001 and 6061 aluminum alloys and aluminum-base fuel dispersion at elevated temperatures.* DOI: 10.2172/4114215. URL: https://www.osti.gov/biblio/4114215-mechanical-properties-x8001-aluminum-alloys-aluminum-base-fuel-dispersion-elevated-temperatures.

[82] U.S Nuclear Regulatory Commission. "Safety Evaluation Report: related to the Evaluation of Low-Enriched Uranium Silicide-Aluminum Dispersion Fuel for Use in Non-Power Reactors". In: *OSTI* (). DOI: 10.2172/6830338. URL: https://www.osti.gov/biblio/6830338.

[83] G. L. Copeland, R. W. Hobbs, G. L. Hofman, J. L. Snelgrove. *Performance of low-enriched U3Si2-aluminum dispersion fuel elements in the Oak Ridge Research Reactor: ANL/RERTR/TM-10.*

[84] K. Farrell. "5.07 - Performance of Aluminum in Research Reactors". In: *Comprehensive nuclear materials.* Ed. by R. J. M. Konings. Place of publication not identified: Elsevier Science, 2011, pp. 143–175. ISBN: 978-0-08-056033-5. DOI: 10.1016/B978-0-08-056033-5.00113-0. URL: https://www.sciencedirect.com/science/article/pii/B9780080560335001130.

[85] *5051A (AlMg2(B), 3.3326) Aluminum.* 30.05.2020. URL: https://www.makeitfrom.com/material-properties/5051A-AlMg2B-3.3326-Aluminum.

[86] E. Popov. *Preliminary Report on U-Mo Monolithic Fuel for Research Reactors.* March 2020.

[87] B. W. Boehm. "Software Engineering Economics". In: *Pioneers and Their Contributions to Software Engineering.* Springer, Berlin, Heidelberg, 2001, pp. 99–150. DOI: 10.1007/978-3-642-48354-7{\textunderscore}5. URL: https://link.springer.com/chapter/10.1007/978-3-642-48354-7_5.

[88] F. Blotnner. "Accurate Navier-Stokes results for the hypersonic flow over a spherical nosetip". In: *Journal of Spacecraft and Rockets* 27.2 (1990), pp. 113–122. DOI: 10.2514/6.1989-1671.

[89] P. J. Roache. *Verification and validation in computational science and engineering.* Albuquerque, N.M.: hermosapublishers, 1998. ISBN: 0-913478-08-3.

[90] U. Mehta. "Guide to credible computer simulations of fluid flows". In: *Journal of Propulsion and Power* 12.5 (1996), pp. 940–948. DOI: `10.2514/3.24126`. URL: `https://www.semanticscholar.org/paper/Guide-to-credible-computer-simulations-of-fluid-Mehta/9e99273407d57c311205400a37f73398ce8d2da8`.

[91] *Guide for the verification and validation of computational fluid dynamics simulations*. Washington, D.C.: American Institute of Aeronautics and Astronautics, 1998. ISBN: 978-1-56347-285-5. DOI: `10.2514/4.472855`.

[92] Nuclear Energy Agency. *Best Practice Guidelines for the Use of CFD in Nuclear Reactor Safety Applications – Revision: NEA/CSNI/R(2014)11*. Paris.

[93] M. Sitek, A. Bergeron, C. Bojanowski, Y. Yu, and J. Licht. "Involute Working Group – Development and Validation of the Finite Element Models of the Cheverton-Kelley Experiments". In: *OSTI* ANL/RTR/TM-20/15 (). DOI: `10.2172/1777474`. URL: `https://www.osti.gov/biblio/1777474`.

[94] P. K. Jain, J. D. Freels, and D. H. Cook. "3D COMSOL Simulations for Thermal Deflection of HFIR Fuel Plate in the "Cheverton-Kelley" Experiments: ORNL/TM-2012/138 NN9002000; MDGA518". In: *OSTI* (). DOI: `10.2172/1047622`. URL: `https://www.osti.gov/biblio/1047622`.

[95] S. Levy, R. A. Fuller, and R. O. Niemi. "Heat Transfer to Water in Thin Rectangular Channels". In: *Journal of Heat Transfer* 81.2 (1959), pp. 129–140. ISSN: 0022-1481. DOI: `10.1115/1.4008156`.

[96] C. Bojanowski, R. Schönecker, K. Borowiec, K. Shehu, J. Mercz, F. Thomas, A. Bergeron, P. Jain, C. Reiter, and J. Licht. *Verification and Validation of CFD Codes with Application to Heat Transfer in Involute Reactors*.

[97] W. Y. Du. *Resistive, capacitive, inductive, and magnetic sensor technologies*. Series in sensors. Boca Raton, London, and New York: CRC Press, 2015. ISBN: 9780429093180. DOI: `10.1201/b17685`. URL: `https://www.taylorfrancis.com/books/mono/10.1201/b17685/resistive-capacitive-inductive-magnetic-sensor-technologies-winncy-du`.

[98] R. E. Pawel, G. L. Yoder, C. D. West, and B. H. Montgomery. "The development of a preliminary correlation of data on oxide growth on 6061 aluminum under ANS thermal-hydraulic conditions". In: ORNL/TM-11517 (1990). DOI: `10.2172/5780409`. URL: `https://www.osti.gov/biblio/5780409`.

[99] Feltes. *Nukleare Kernauslegung FRM II - A1C-1300070-2: Arbeitsbericht*. 1996.

[100] NRC Web. *Scram: https://www.nrc.gov/reading-rm/basic-ref/glossary/scram.html*. 3/7/2023. URL: `https://www.nrc.gov/reading-rm/basic-ref/glossary/scram.html`.

[101] S. Skreba, J. Adamek, and H. Unger. *Experimentelle Untersuchungen und Ergebnise zur Abfuhr der Nachzerfallswaerme im FRM II: Abschlußbericht zum Forschungsvorhaben: Untersuchung des Übergangs von Zwangsauf Naturumlauf*.

[102] Heinecke and Sperber. *Ausfall aller Primärpumpen (Notstromfall) - FRM II - 23 0520.0004: Arbeitsbericht.* 1997.

[103] Gysler. *Betrachtungen zu den Folgen eines postulierten Ausfalls des Notkühlsystems bei freiem Auslaufen der Primärpumpen - FRM II - 28 0320.0002.* 1994.

[104] K. Shehu, J. Mercz, W. Petry, and C. Reiter. "Mechanical Evaluations to Define Possible Fuel Element Designs for the Conversion of FRM II". In: *Advances in Thermal Hydraulics ATH' 2020*, pp. 1194–1206.

[105] K. Shehu, B. Stepnik, W. Petry, and C. Reiter. "Determination of Young's Modulus of FRM II Fuel Plate Using the Impulse Excitation Technique (IET)". In: *to be published* (2023).

[106] K. Shehu and C. Reiter. "Coupling of Serpent 2 with Ansys CFX for FRM II Conversion Studies". In: *To be published.*

List of Publications

Publications related to the dissertation

- K. Shehu, C. Bojanowski, A. Bergeron, W. Petry, C. Reiter, "First Steps to Coupled Hydraulic and Mechanical Calculations Within a Parameter Study to Define Possible Core Designs for the Conversion of FRM II", *EPJ Web of Conferences* **247**, 8011 (2021). [15]

- K. Shehu, J. Mercz, W. Petry, C. Reiter, "Mechanical Evaluations to Define Possible Fuel Element Designs for the Conversion of FRM II", *Proceedings of Advances in Thermal Hydraulics ATH 2020*, 1194, (2020). [104]

- K. Shehu, B. Stepnik, Y. Calzavara, W. Petry, C. Reiter, "Determination of Young's Modulus of FRM II Fuel Plate Using the Impulse Excitation Technique (IET)", *In internal review process* (2023). [105]

- M. Sitek, K. Shehu, P. Jain, A. Bergeron, J. Licht, C. Reiter, "Thermomechanical Analysis and Modeling of Involute-Shaped Fuel Plates Using the Cheverton–Kelley Experiments for the High Flux Isotope Reactor", *Nuclear Engineering and Design* **409**, 112334 (2023). [16]

- K. Shehu, C. Reiter, "Coupling of Serpent 2 with Ansys CFX for FRM II Conversion Studies", *to be published*, 2023. [106]

- C. Reiter, A. Bergeron, D. Bonete-Wiese, M. Kirst, J. Mercz, R. Schönecker, K. Shehu, B. Ozar, F. Puig, J. Licht, W. Petry, P. Müller-Buschbaum, "A Low-Enriched Uranium (LEU) option for the conversion of FRM II", *Annals of Nuclear Energy* **183**, 109599 (2023). [3]

- C. Reiter, M. Kirst, K. Shehu, D. Bonete-Wiese, R. Schönecker, A. Bergeron, F. Puig, B. Ozar, "Modelling of the FRM II - Validation and Verification of the Models and Methods", *Unpublished confidential TUM document*, (2022). [10]

Acknowledgements

This thesis is the testimonial of the blood, sweat and tears of four and a half years. These past years have been nothing short of life-changing, exciting, and fundamentally unique, from starting my PhD literally the day before my master's defense to a global pandemic that altered everybody's routines forever to this moment full of relief writing this sentence. It is not easy to write the acknowledgments and express my gratitude to so many people that have been with me, around me or 1500 km away, but I will give it a go.

First and foremost, I would like to thank Professor Winfried Petry for giving me the opportunity to work on my PhD thesis in his group, for his guidance and the freedom he gave me to develop my own ideas. The discussions in his office and in side meetings during conferences have been extremely helpful from a scientific point of view and a social one.

Words cannot express my gratitude to Dr. Reiter (aka Christian) for being a supervisor, mentor and friend. Talks starting from reactor physics in O'hare airport to teaching me Bavarian words have certainly been some highlights of these years. Lastly, thank you Christian for deciding to come back to FRM II. I know this thesis would not have been what it is without your support. Habe d'ere!

A part of the happiness these years has been working with great people. On that note, I would like to thank my colleagues: Miriam, Ronja, Joy, Julius, Til, Daniel, Paul, JP, Gabriele, Chris, Andi, Lorenzo, Lukas, Cecilia, Tobi, Schwarzi, Anna, Bruno, Kevin. Working with these guys has been a ton of fun, and I am happy to say I made a few friends along the way. I am also very grateful to the fellow researchers at Institute Laue-Langevin: Fred and Yoann for the very nice Zoom calls and Fred for always providing a few jokes that break the ice of every situation. Thanks go as well as to the colleagues across the Atlantic at Argonne National Laboratory and Oak Ridge National Laboratory: Marta, Cezary, Basar, Francesc, Aurelien, Jeremy and Prashant. The scientific discussions and burger dinners in the suburbs of Chicago are deeply appreciated. Additionally, I would like to thank the LRZ and Ansys gurus Dr. Thomas Frank and Dr. Georg Scheurer, for all the help during these years. I am also thankful to Dr. Breitkreuz for the PhD interview about 5 years ago that changed the course of my life. Being confronted with the statement "We work like vampires" when entering a completely dark office was the enticement I needed to want to be in this group.

A huge thank you goes also to my friends Nisli, Ola, Laura, Michal, for always being a delight